Magnetoresistance and magnetization dynamics in hybrid structures

Dissertation
zur Erlangung des Doktorgrades
des Department Physik
der Universität Hamburg

vorgelegt von
Andreas Wittmann
aus Tettnang

Hamburg
2008

Gutachter der Dissertation	Prof. Dr. Detlef Heitmann Prof. Dr. Dirk Grundler
Gutachter der Disputation	Professor Dr. Wolfgang Hansen Professor Dr. Dirk Grundler
Datum der Disputation	25. Juli 2008
Vorsitzender des Prüfungsausschusses	PD. Dr. Alexander Chudnovskiy
Vorsitzender des Promotionsausschusses	Prof. Dr. Jochen Bartels
Dekan der Fakultät für Mathematik, Informatik und Naturwissenschaften	Prof. Dr. Arno Frühwald

Abstract

In this work experimental and theoretical studies on dc and ac magnetotransport phenomena in ferromagnet (FM)/semiconductor (SC) hybrid structures are presented: first, spin transport effects in FM/SC/FM hybrid structures, second the dc voltage drop across a nonmagnetic metal (NM)/FM/SC hybrid structure under microwave irradiation.

We present simulations of the spin–orbit coupling in SC and of spin polarized transport in hybrid structures. These simulations are important to understand our experimental results. Then we report on magnetotransport experiments on a Co/InAs (2DES)/Co hybrid structure, where the InAs–based heterostructure incorporates a two–dimensional electron system (2DES). The device is based on a successively optimized sample design with the goal to prepare clean and flat FM/SC interfaces. The concept started from the prediction of a spin filter effect at FM/InAs interfaces by D. Grundler and the challenge to realize a ballistic transport regime. The sample preparation includes novel techniques to create FM/SC interfaces fully in situ by a cleaved–edge overgrowth process. Further we present the procedures we developed to pattern a metallic film on the cleaved edge of a SC on the micrometer and nanometer scale. In our device we find a gate voltage dependent spin–valve effect. However the signal strength is far smaller than predicted. Reasons for this are discussed.

In the second part we present experiments on a NM/FM/2DES hybrid structure under microwave irradiation. We characterize the ferromagnetic resonance (FMR) frequencies of the 20 nm thick polycrystalline Co film as a function of an applied magnetic field. For this we excite a precession of the magnetization using a microwave and detect the absorption inductively. The FMR signature indicates a magnetic anisotropy. We provide evidence that the magnetic easy axis points perpendicular to the film plane. Then, data of the measured voltage across the Al/Co/InAs (2DES) device are presented. For a resonantly precessing magnetization of the Co film we observe a characteristic voltage signal. It changes sign if the applied magnetic field strength equals the anisotropy field. The data are discussed using three independent models. Most promising to explain our findings is the model of a rf induced photovoltage, which we recalculated in order to adapt it to our device geometry.

Inhaltsangabe

In dieser Arbeit werden experimentelle und theoretische Studien über DC und AC Magnetotransportphänomene an Ferromagnet (FM)/Halbleiter (HL)–Hybridstrukturen behandelt: zuerst Spintransport–Effekte in FM/HL/FM Hybridstrukturen, dann der Spannungsabfall über eine nichtmagnetische Metall (NM)/FM/HL–Hybridstruktur unter Einstrahlung von Mikrowellen.

Simulationen der Spin–Bahn Wechselwirkung im HL und von spinpolarisiertem Transport durch Hybridstrukturen werden vorgestellt. Die Simulationen tragen zum Verständnis der Messdaten bei. Dann wird über Magnetotransportexperimente an einer Co/InAs (2DES)/Co–Hybridstruktur berichtet, wobei die InAs–Heterostruktur ein zweidimensionales Elektronensystem (2DES) enthält. Die Probe basiert auf fortlaufender Optimierung der Reinheit und Glattheit der Grenzflächen. Das Konzept beinhaltet die Vorhersage von D. Grundler, nach der an FM/InAs Grenzflächen ein Spinfilter–Effekt auftritt und die Realisierung von ballistischem Transport. Für die Präparation der Proben wurden neuartige Methoden entwickelt um FM/HL Grenzflächen unter Hochvakuumbedingungen herzustellen. Darüber hinaus werden Prozesse zur Mikro- und Nanostrukturierung von Metallfilmen auf Spaltkanten beschrieben. In unserer Probe wird ein gatespannungsabhängiger Spinventil–Effekt beobachtet. Die Signalstärke ist jedoch weit geringer als erwartet. Gründe hierfür werden angeführt.

Im zweiten Teil werden Experimente an NM/FM/2DES–Strukturen unter Mikrowellenbestrahlung vorgestellt. Die ferromagnetische Resonanz (FMR) des 20 nm dicken, polykristallinen Co–Films wird als Funktion eines angelegten Magnetfelds gemessen. Dazu wird die Magnetisierung mithilfe von Mikrowellen zur Präzession angeregt und deren Absorption induktiv bestimmt. Die FMR–Signatur deutet auf eine magnetische Anisotropie hin. Es gibt Anzeichen für eine magnetisch leichte Achse senkrecht zum Film. Dann werden Spannungsmessungen an einem Al/Co/InAs (2DES) Bauteil vorgestellt. Bei resonanter Präzession der Magnetisierung im Co–Film wird ein charakteristisches Spannungssignal beobachtet. Dieses ändert sein Vorzeichen, wenn das angelegte Magnetfeld die Anisotropiefeldstärke erreicht. Drei Modelle werden diskutiert. Als vielversprechend wird das Modell einer mikrowelleninduzierten Photospannung erachtet. Das Modell wurde erweitert und an unsere Probengeometrie angepasst.

Contents

Abstract i

Inhaltsangabe iii

Contents v

1 Introduction 1

2 Physical concepts 3
2.1 Magnetic properties of ferromagnetic metals 3
2.1.1 Magnetic domains: Magnetization and switching 3
2.1.2 Spin polarization of conduction electrons 6
2.2 Spin effects 7
2.2.1 Inversion–asymmetry–induced spin splitting 8
2.2.2 Tunability of the spin–orbit coupling 12
2.2.3 Spin relaxation mechanisms in semiconductors 15
2.2.4 The spin pumping effect and the spin battery 17
2.2.5 Spin filtering at FM/SC interfaces 20
2.3 Magnetoresistance effects 22
2.3.1 The anisotropic magnetoresistance effect 22
2.3.2 The IPHE and the AHE 23
2.3.3 Magnetoresistance effects in a 2DES 24
2.3.4 Magnetoresistance effects in hybrid structures 28
2.4 Microwave induced photovoltage 31
2.5 The spin field–effect transistor 32

3 Preparation 35
3.1 Spin FET devices 35
3.1.1 Properties of the InAs heterostructure 35
3.1.2 Cleaved–edge overgrowth 36
3.1.3 Photolithography on the cleaved edge 38
3.1.4 Shaping source and drain contacts with a focused ion beam . . . 39
3.1.5 Separation of source and drain contacts with nanoindenting . . . 40
3.1.6 Preparation of the gate electrode 40
3.1.7 Contacting the sample 42
3.1.8 Cryogenic magnetotransport setup 42
3.2 Spin battery devices 45
3.2.1 Measurement setup for spin battery devices 47

4 Spin–orbit interaction in InAs 2DES **49**

5 Calculated impact of a gate voltage **53**

6 Calculations on spin dependent transport **57**
6.1 Calculating the transmission function 58
6.2 Gate voltage dependent transmission 59
6.3 Spin–orbit coupling dependent transmission 63
6.4 Calculated giant magnetoresistance effect 64

7 Magnetotransport on spin FET devices **67**
7.1 Magnetoresistance at fixed electron density 67
7.1.1 Signatures of the GMR effect 67
7.1.2 Signatures of the EMR effect 70
7.2 Magnetotransport with modulated gate voltage 72
7.2.1 Impact of the gate voltage 72
7.2.2 Angular dependence of oscillating device resistance 73
7.2.3 Temperature dependence 75
7.2.4 Interpretation 76

8 Hybrid structures under rf irradiation **81**
8.1 Resonance of the ferromagnetic film 81
8.2 dc voltage detection of magnetic resonances 83
8.2.1 Microwave induced dc voltage: Dependence on modulation frequency, bias current, illumination and rf power 86
8.2.2 Interpretation 89

9 Conclusions **101**

A. List of abbreviations **105**

Bibliography **107**

Chapter 1

Introduction

In this thesis two aspects of hybrid systems are investigated: First, spin polarized transport through ferromagnetic metal (FM)/semiconductor (SC)/FM devices, where the SC is a heterostructure that incorporates an InAs two–dimensional electron system (2DES), and second, the dynamic photo–Hall voltage of non–magnetic metal (NM)/FM/InAs (2DES) devices under microwave irradiation. The investigation of these aspects requires two different experimental setups, i.e. a cryogenic magnetotransport setup and a room temperature high frequency probe station. In the following we motivate both experiments separately.

In 1990 S. Datta and B. Das [Dat90] proposed to control the resistance of a FM/2DES/FM hybrid structure by means of the electron's spin rather than it's charge. Such devices are discussed controversially as the conductivity mismatch of the materials is a fundamental obstacle for effective spin–injection into the SC [Sch00]. On the other hand, high purity interfaces are predicted to exhibit a spin filter effect and, implemented in ballistic transport devices, are promising means for the realization of a spin field–effect transistor (FET) [Gru01a][Mat02]. Realizing such a spin FET is one of the longest standing hopes of spin–based electronics [Pri95]. This statement was made in 1995 by G. Prinz in a review article about spin polarized transport. Many technological advantages are attributed to a spin FET compared with conventional field–effect transistors by K. C. Hall and M. E. Flatté [Hal06]. The efforts during almost two decades to realize this device led to a high research activity in the field of SC spintronics and to the emergence of related research fields. Spin effects like the giant magnetoresistance (GMR), the tunability of spin–orbit interaction and the spin battery effect were investigated and explained. Currently a great challenge for researchers in the field of spintronics is to develop a coherent model that describes the transport of spin polarized electrons in SC and the spin injection across interfaces.

In this work we address these aspects theoretically and experimentally on the basis of a Co/InAs (2DES)/Co spin FET device. The lack of fundamental investigations of the spin–orbit interaction in InAs quantum wells (QW) motivated a detailed calculation of the band structure and electron states using the so–called tight–binding model. Further we performed extended computer simulations of transmission properties of nanoscaled spin FET devices. These are important to understand the influence of quantization phenomena in spin transport experiments. In our experiments we observe an oscillating device resistance as a function of an applied gate voltage. Models that could explain these oscillations are discussed.

A fast–growing field of spin physics is the magnetization dynamics. In particular this field covers collective spin excitations and spin waves. The ambition to exploit these all–magnetic signals for information processing is often summarized by the term *magnonics* [Kru06]. Further, microwave induced switching or spin accumulation through spin pumping might be relevant for future applications. Recently the groups of B. van Wees and C.–M. Hu published intriguing experiments on non–magnetic metal (NM)/FM/NM hybrid structures [Cos06a] and on single FM microstructures [Mec07], respectively. Both groups find dc components in the measured voltage across the devices and they suggest different applications for their findings: the all–electrical detection of spin accumulation and the rectification of an induced rf current. Although very similar results are found, the groups provide substantially different explanations of the observed phenomena.

In this thesis we investigate the voltage generation across an Al/Co/InAs (2DES) hybrid structure under microwave (rf) irradiation. By implementing a two–dimensional electron system (2DES) imbedded in an InAs based SC heterostructure we obtain additional tuning parameters for future experiments. We will show that our hybrid device not only exhibits a voltage signal similar to the results found in literature but additionally, we present a striking sign change in our measured signal. We discuss the models mentioned above and perform detailed calculations to adapt these models to our experiment.

Chapter 2

Physical concepts

This thesis deals with magnetotransport experiments on hybrid structures consisting of a SC heterostructure and a FM. In this chapter an overview of the physical concepts that are involved in this work is presented. It starts with the explanation of relevant properties of FM which are implemented in the samples we present here. Then we discuss spin effects with a focus on III–V SC heterostructures incorporating a 2DES. Within such systems a spin splitting occurs for zero magnetic field. We discuss the spin–orbit coupling and its tunability. Further an overview of spin scattering processes is given. We also mention the spin pumping and the spin battery effect. The latter effects do not depend on the presence of a SC but are important for the discussion of our data in chapter 8. This is followed by the discussion of spin filtering at FM/SC interfaces. The last section deals with transport phenomena occurring in FM/NM or FM/SC hybrid structures, such as the anisotropic magnetoresistance (AMR), the extraordinary magnetoresistance (EMR) effect and the GMR effect. On the basis of the AMR effect we discuss the microwave induced photovoltage. Finally, to understand the working principle of a spin field–effect transistor, we discuss the concept of the electronic analog of the electro–optic modulator presented by S. Datta and B. Das in 1990.

2.1 Magnetic properties of ferromagnetic metals

In our experiments FM are used for spin injection. FM have a finite magnetization in the absence of an external magnetic field for temperatures below the Curie temperature. We use FM films that are deposited by thermal evaporation. So we focus on polycrystalline thin films. In this section we discuss the properties of magnetic domains and the spin polarization mechanism.

2.1.1 Magnetic domains: Magnetization and switching

The existence of a spontaneous magnetization of the FM Ni, Fe and Co can be explained with the Stoner criterion [Iba99]. It is based on a system of free electrons which is extended to a band model that includes the exchange interaction between the electrons.

First we summarize the origin of the exchange interaction, which is described in detail in textbooks like [Iba99] or [Ash76]. The probability for two electrons with the same spin orientation to be located at the same place is zero, according to Pauli's exclusion principle. As a consequence, these electrons are distributed over a larger space and thus are less capable to shield the Coulomb attraction of a positive core from a

third electron. The third electron "feels" a reduced electron density in its vicinity what is called an exchange hole. This results in a reduction of energy for the third electron in vicinity of a core potential. The more electrons with the same spin are present, the more effective is the energy reduction. The consequence, which is only valid for FM, is that this exchange mechanism results in a parallel alignment of electron spins because the total energy of the system is reduced in this case.

In FM the electrons of the $4s$ and the $3d$ shells contribute to the electron density at E_F. Due to the latter exchange interaction the energy band of the $3d$ shell is split into two parts with parallel but opposite spin orientations [Kit93] as shown schematically in figure 2.1. These parts will further be referenced as the spin–up band and the

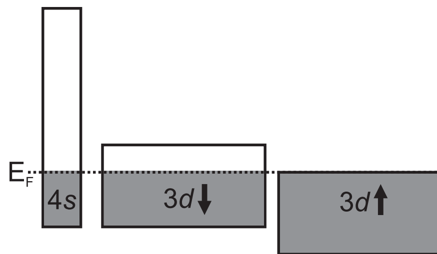

Figure 2.1: The $4s$ and the $3d$ energy bands of Ni are displayed schematically for $T = 0$ K. The $3d$ band is spin split due to the exchange interaction of the electrons and the energy of the $3d$ spin-up band is lowered. Thus this band is fully occupied. No splitting occurs for the high mobility $4s$ band.

spin–down band. For $T = 0$ K the energy of the spin–up band is reduced and the entire band resides below the Fermi level. Thus this band is completely filled with spin–up electrons. On the other hand, the energy level of the spin–down band is such that E_F intersects the band. Thus the spin–down band is only partly filled. So there are less spin–down electrons in the $3d$ shell compared with spin–up electrons. As each electron carries a magnetic moment this imbalance produces a net magnetization of a FM. One can determine the number of effective Bohr magnetons n_B per atom. For Ni at $T = 0$ K the effective Bohr magneton number is $n_B = 0.54$ per atom [Kit93]. The contribution of the orbital motions is included.

Macroscopic FM can be seen as an ensemble of domains. Each domain exhibits a uniform magnetization $\boldsymbol{m}$ in the absence of an external magnetic field. The formation of a multi–domain state results from the dipole interaction between electron spins [Ash76].

In the following it is shown that the domain structure depends strongly on geometrical properties. In thin FM films the total magnetization $\boldsymbol{M} = \sum_i \boldsymbol{m}_i$ is oriented preferably in the plane of the film. In [Bar04] the authors report on a systematic variation of the lateral geometry and thickness of microstructured permalloy ($Ni_{83}Fe_{17}$) thin films. They mapped the magnetization with a magnetic force microscope and resolved domain walls of multi–domain structures. The smaller the structures, the less domains are observed. It is possible to design single domain structures.

In [Gil05] the authors report that an extended polycrystalline Co film of 20 nm thickness exhibits magnetic domains with an area of some 100 μm^2 in its demagnetized state. The magnetization of these domains points in the plane of the film. Different results are reported for a patterned 20 nm thick polycrystalline Co film [New96]. Here, elliptic structures below 150×200 nm^2 provide single–domain islands with random

directions of $\boldsymbol{m}$, whereas above this limit domain walls exist within the structures. The resulting domain structure is such that the total energy of the FM reaches an absolute or relative minimum [Hub98]. The arrangement of the magnetic domains, in particular of the edge domains is determined by so–called stray field energy. An equilibrium domain configuration is reached if the stray field energy reaches a minimum. This minimum, in turn, depends on the shape of the FM.

With an externally applied magnetic field H the domain walls shift in order to maximize domains with a magnetization parallel to H at the expense of domains with m in other directions. The more domains are aligned, the higher the total magnetization M of the structure. For an increasing magnetic field, the saturation magnetization M_{sat} is reached at H_{sat}. Depending on the FM material and the shape of the structure different hysteresis curves can be measured. In figure 2.2 typical hysteresis curves for Co and Fe are shown. The results were published recently by J. Islam et al. in [Isl07].

The curves are measured with a SQUID[1] setup on extended films of two different

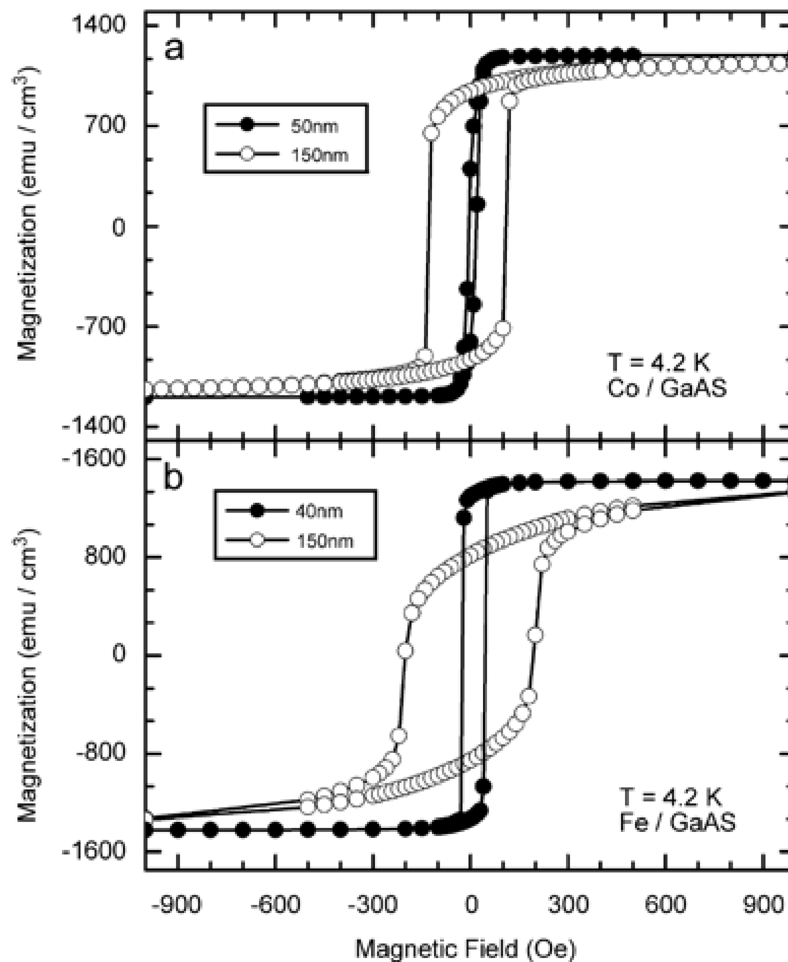

Figure 2.2: (a) Hysteresis curves of 50 and 150 nm thick Co and (b) 40 and 150 nm thick Fe films on a GaAs (001) substrate at 4.2 K. The magnetic field was parallel to the film plane. The graphs were taken from [Isl07]. They demonstrate how the design of a FM layer can influence the magnetization behavior.

thicknesses for each material. One can observe that the coercive field H_{coe}, the field at which the magnetization starts to change its sign, can be varied by choosing different thicknesses of the FM film. Single domain structures show an abrupt switching of M if H_{coe} is reached. They exhibit a square–shaped hysteresis curve.

A comprehensive overview of the behavior of magnetic domains can be found in the book of A. Hubert and R. Schäfer [Hub98].

2.1.2 Spin polarization of conduction electrons

In FM like Ni the $3d$ shell contributes to the electron density at E_F. As explained in section 2.1.1 the energy band of the $3d$ shell is split into two parts: one for spin–up electrons, one for spin–down electrons [Kit93].
The energy level of the spin–up $3d$ band is lowered by the splitting, such that, at $T = 0$, it lays below the Fermi level. Then, this band is completely filled with spin–up electrons. The spin–down band remains partly filled. The electron density at the Fermi energy is visualized in figure 2.3 taken from [Cal73]. In this reference the DOS for

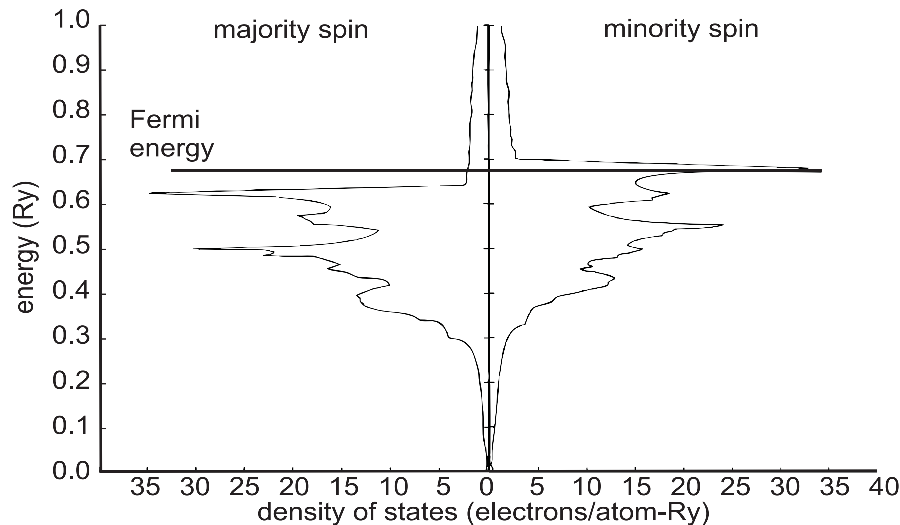

Figure 2.3: Energy distribution of the density of states for Ni. At the Fermi energy an imbalance occurs, leading to a spin polarized electron transport. The graph was taken from J. Callaway and C. S. Wang [Cal73].

the spin–up and spin–down electrons is calculated self consistently for Ni using the tight–binding approach. One can see that the DOS is unbalanced at the Fermi energy. Charge transport in $3d$ metals is governed by electrons in s like states. Thereby two scattering processes dominate: the scattering of the s electrons into unoccupied d states and into other s states. At $T = 0$, the $3d$ spin–up states are occupied, so the spin–up $4s$ electrons can scatter only into other high mobility $4s$ states. Hence the resistance of the spin–up oriented electrons is much smaller (N. F. Mott estimates by a factor 5) than for the spin–down $4s$ electrons, which have a finite probability to scatter into $3d$ states with a lower mobility. Therefore, at low temperatures, we may assume that

[1] **S**uperconducting **Q**uantum **I**nterference **D**evice

the resistance is determined mainly by the s–s transitions of the spin–up electrons. This theory was presented in 1936 by N. F. Mott [Mot36] based on separate conductive channels for the two spin orientations parallel and antiparallel to the magnetization of the FM. For transition metals this two–current approach is a straightforward picture to discuss transport phenomena and to explain spin polarization of electrons.

A high spin polarization is essential for the devices presented in this thesis. So we compare the spin polarizations of different transition metals and compounds as well as non–transition metals in table 2.1.

material	**spin polarization**
Co	35 % – 42 %
Ni	23 % – 46.5 %
Fe	40 % – 45 %
$Ni_{80}Fe_{20}$	25 % – 37 %
CrO_2	96 %
NiMnSb	58 %, 100 % (theor.)
Ni_2MnIn	34 %

(2.1)

These values are experimentally determined and reported in [Sou98] and [Ji01]. First principle calculations of spin polarizations were recently published in [Bah07]. For the diffusive transport regime, they obtain 54 % for Fe and −80 % for Ni and in the ballistic transport regime 42 % and −47 %.

We decided to use Co as FM contacts for the devices presented in this work. The decision is founded on its high spin polarization and its good conductivity. We found that these properties are stable with time even if the samples are exposed to air. As a reference we measured the ferromagnetic resonance (FMR) of unstructured Co films and found a long term stability of its magnetic properties, e.g. the saturation magnetization over months. We also performed transport experiments with Fe contacts. The results were not reproducible and unstable with time. We attribute this behavior to oxidation and corrosion of the contacts if exposed to ambient air. These aging effects were not observed with Co contacts. Co is deposited by thermal evaporation and thus suits our prerequisites for cleaved–edge overgrowth (CEO) preparation that will be introduced in chapter 3. The coercive field can be tailored by exploiting the magnetic shape anisotropy of Co microstructures as shown in [Cos06c]. It is a reliable magnetic material as its magnetic properties do not depend severely on a compound composition. This is in contrast to so–called half–Heussler alloys [Heu03]. For this material class a spin polarization of 100 % is predicted theoretically [dG83] but was not reached experimentally so far [Boc07].
Table 2.1 shows a high degree of spin polarization for CrO_2. In [Ji01] and in [Par02] we find that CrO_2 is a metastable material. Its surface degrades almost immediately after growth into Cr_2O_3 and possibly other Cr oxides. Oxidic Cr compounds exhibit a small conductivity and consequently are not suitable for transport experiments.

2.2 Spin effects

In this part we discuss spin effects that will be important for the interpretation of the experimental data presented in this thesis. Most topics are thoroughly reviewed by J. Fabian et al. in [Fab07], further references will be provided in the subsections. This section starts with the spin splitting of energy bands in a quantum well (QW) in absence

of an external magnetic field H. We introduce the so–called Rashba parameter as a measure for the spin splitting and show how it depends on the material, on electric fields and on the electron density in the QW. Then important mechanisms are presented that contribute to relax a given spin polarization in SC. In the following we briefly review recently discovered spin effects like spin pumping and the spin battery effect. At the end of the section we discuss spin filtering at FM/SC interfaces.

2.2.1 Inversion–asymmetry–induced spin splitting in III–V semiconductors at $H = 0$

We explain the existence of the inversion–asymmetry–induced spin splitting of the energy dispersion in SC materials. In particular we consider quasi–2D quantum wells (2DES) in heterostructures based on common III–V SC, e.g. GaAs or InAs, with a zinc blende lattice structure. These structures generally exhibit two types of asymmetries: bulk inversion asymmetry (BIA) of the underlying crystal and structure inversion asymmetry (SIA) of the confinement potential.

In the presence of such asymmetries the energy dispersion splits into $E^{(+)}(\boldsymbol{k})$ and $E^{(-)}(\boldsymbol{k})$ for electrons with opposing spin orientation $(+)$ and $(-)$ even if no external magnetic field is present. In a publication of Riechert et al. [Rie84] the first measurement of the splitting of the energy dispersion is reported. In their experiment they exploited the precession of the spin polarization of photoexcited conduction electrons of GaAs. This spin splitting is based on spin–orbit coupling. In simple terms, the coupling can be understood as follows: An electron has an intrinsic magnetic dipole moment and behaves like a miniature bar magnet that is aligned along its axis of angular momentum. As it orbits around the nucleus, the electron produces a magnetic field that modifies its own magnetic moment. This interaction is know as *spin–orbit coupling*.

Currently there are two substantially different approaches to quantify the spin splitting phenomenon. First there are calculations based on $\boldsymbol{k} \cdot \boldsymbol{p}$ theory. A very detailed description of spin–orbit effects using this theory is given by R. Winkler [Win03]. This method allows to study spin splitting of the conduction band in consideration of a limited number of energy bands. For 8 bands, an 8×8 or, for 14 bands an extended 14×14 Kane Hamiltonian must be properly defined.
A different approach was initiated by J. A. Majewski and P. Vogl [Maj02]. They define a universal Hamiltonian that is not limited to a finite number of energy bands. The calculations of the band structure and the spin splittings are based on the tight–binding model. In the following we discuss the two approaches separately.

The $\boldsymbol{k} \cdot \boldsymbol{p}$ theory approach

The first calculations of spin–orbit coupling effects that revealed a spin splitting are based on $\boldsymbol{k} \cdot \boldsymbol{p}$ theory. They were performed by G. Dresselhaus for a 3D zinc blende crystal [Dre55]. He included the bulk inversion asymmetry in the model and found that the spin degeneracy of the conduction band is lifted for symmetry reasons. This is why the BIA contribution to the Hamiltonian is also referenced as the Dresselhaus term. R. Winkler shows that the BIA spin splitting results from the coupling between the valence bands and the conduction band [Win03].

In SC heterostructures with 2DES an additional spin–orbit coupling effect occurs. It is usually referred to as the Bychkov–Rashba spin–orbit interaction [Byc84a][Byc84b].

It is caused by the structure inversion asymmetry (SIA) of the confining potential. R. Lassnig describes the influence of band mixing in QW on the electronic structure [Las85]. The calculations are also based on $\boldsymbol{k} \cdot \boldsymbol{p}$ theory. He points out that a spin splitting caused by SIA in the conduction band results from the electric field ε_z^V in the valence band. The mechanism can be explained as follows: The QW is formed by a sequence of SC with different energy gaps. A schematic band structure is shown in the central graph of figure 2.4. As a result of the discontinuity of the potential V and due

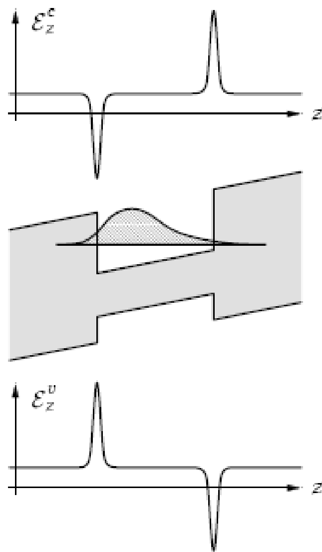

Figure 2.4: Qualitative sketch of an electron wave function in presence of a quantum well and an external electric field (middle part). The upper (lower) graph shows the effective electric field in the conduction (valence) band. The figure is taken from [Win03].

to $\varepsilon_z = dV/dz$, peaks of the electric field distribution occur at the positions of the SC interfaces. These are shown in figure 2.4 for the conduction band (ε_z^C, upper picture) and the valence band (ε_z^V, lower picture). In addition to that, an electric field ε_z^{SIA}, perpendicular to the 2DES originates from SIA. The latter field tilts the band structure and thus shifts the probability density of the conduction electrons in z direction. The middle part of figure 2.4 shows a sketch of the resulting probability density function. An equilibrium electron distribution is reached, if its maximum is located at the position, where ε_z^C and ε_z^{SIA} cancel each other and no net Coulomb force acts on the electrons (Ehrenfest's theorem). On the other hand the corresponding electric field from the valence bands ε_z^V does not cancel. So the electrons in the conduction band still "feel" the influence of ε_z^V. This intrinsic field can be tuned by an external electric field ε_z^{ext} achieving a tunability of the spin–orbit coupling. ε_z^V and ε_z^{ext} add to the total electric field

$$\varepsilon_z = \varepsilon_z^{ext} + \varepsilon_z^V \ . \tag{2.2}$$

In presence of spin–orbit coupling the so–called Rashba term H_{SO} [Byc84a] adds to the Hamiltonian

$$H = H_0 + H_{SO} = \frac{\hbar^2 k^2}{2m^*} + \alpha\, [\boldsymbol{\sigma} \times \boldsymbol{k}] \cdot \mathbf{e}_z. \tag{2.3}$$

m^* is the effective mass of the conduction electrons in the SC, σ represents the Pauli

spin matrices and $\mathbf{e}_z$ is the unit vector in z direction. The parameter α is a measure for the strength of the spin–orbit coupling. It is a material specific value but also depends on ε_z as indicated above. Further details will be discussed in section 2.2.2.
The addition of H_{SO} to the Hamiltonian results in a k–linear energy splitting of the conduction band,

$$E^{(\pm)}(\boldsymbol{k}) = \frac{\hbar^2 k^2}{2m^*} \pm \alpha \cdot \boldsymbol{k} \; . \tag{2.4}$$

Thus a $\mathbf{k}$ dependent energy splitting of $\Delta E(\boldsymbol{k}) = E^{(+)}(\boldsymbol{k}) - E^{(-)}(\boldsymbol{k})$ can be defined.

The presence of an external magnetic field H changes $\Delta E(\boldsymbol{k})$. The SIA splitting is reduced with increasing H and approaches asymptotically the Zeeman splitting [Zaw04].

As already mentioned, the two intrinsic contributions to the spin splitting of the conduction band at zero magnetic field are BIA and SIA. Thus, in the following we distinguish between the BIA and the SIA based energy splitting represented by the two constants α_{BIA} and α_{SIA}. In many publications α_{BIA} is called the Dresselhaus parameter β. The second constant represents the spin–orbit coupling that results from SIA and is often called the Rashba parameter α_R. In most experiments the two constants are not separately measurable and the data represent a superposition of both spin–orbit coupling mechanisms. In this case we use the coupling parameter α without an index as it was the case in equation 2.3 for example. For each contribution two eigenstates exist with opposite spin orientation Ψ^+ and Ψ^- These states are often called spin up (+) and spin down (−) state. In [Win04] detailed calculations show that the spin orientation of these eigenstates rotates in the plane of the QW as a function of k_x and k_y. The graphs in figure 2.5 are taken from [Win04] and display the spin orientations on a contour of constant energy for the SIA (a) and the BIA (b) mechanism, respectively. In

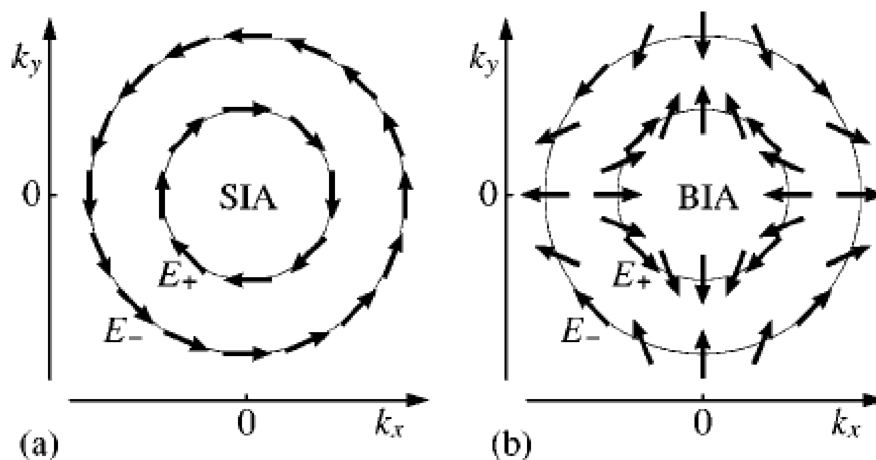

Figure 2.5: Spin orientation of the eigenstates $\Psi^\pm$ (a) due to the Rashba term in a system with SIA and (b) due to the Dresselhaus term in a system with BIA. Source: [Win04].

asymmetric quasi–2D systems the spin distribution is a mixture of both contributions as shown in [Gan03]. Calculations and experiments show that the relative contributions of BIA and SIA based spin splitting to the total spin splitting can be tuned [Sch03] [Gan04]. Both terms can even interfere in such a way that spin splitting effects vanish

completely. This happens if both terms are non–zero but compensate each other.

We consider an electron with $k_y = 0$. At the Fermi energy there are two possible positive k_x with opposite spin orientations. Or, in other terms, for a given $\boldsymbol{k} \neq 0$ there are two energy levels with opposite spin orientations that are separated by

$$\Delta E(\boldsymbol{k}) = 2\alpha \boldsymbol{k} \ . \tag{2.5}$$

This is equivalent to the existence of an effective $\boldsymbol{k}$ dependent magnetic field $\boldsymbol{H}_{\mathit{eff}}$ that interacts with the spin of the electrons in Ψ^+ and Ψ^-. With the introduction of $\boldsymbol{H}_{\mathit{eff}}$ we can revisit two phenomena in a more descriptive way: First, the spin splitting can be ascribed to an effective Zeeman splitting

$$\Delta E_{\mathit{eff}} = g^* \mu_B \mu_0 H_{\mathit{eff}} \ , \tag{2.6}$$

with an effective Landé factor g^* that includes contributions from higher conduction bands [Las85]. Even the zero field splitting can be described with this equation because $\boldsymbol{H}_{\mathit{eff}}$ is also present without external magnetic field. Furthermore the occurrence of a spin precession can be explained by $\boldsymbol{H}_{\mathit{eff}}$ [Kro07]. The time evolution of an electron's spin momentum $\boldsymbol{S}$ in a magnetic field $\boldsymbol{H}_{\mathit{eff}}$ is given by

$$\frac{\partial \boldsymbol{S}}{\partial t} = \mu_0 \boldsymbol{H}_{\mathit{eff}} \times \boldsymbol{S} \ . \tag{2.7}$$

If $\boldsymbol{H}_{\mathit{eff}}$ and $\boldsymbol{S}$ are not parallel, the spin precesses. This precession is the key mechanism of the device proposed by S. Datta and B. Das [Dat90]. They calculated the difference of the two possible electron wave vectors $k_x^{\pm}$ for a given energy and $k_y = 0$ [Dat90]. With equation 2.4 they obtain

$$\Delta k = k^+ - k^- = \frac{2m^*\alpha}{\hbar^2} \ .$$

Now the precession angle φ can be expressed as a function of the spin splitting parameter α, the effective mass m^* and the distance L traveled by the electrons

$$\Delta\varphi = \Delta k L = -\frac{2m^*\alpha}{\hbar^2} L \ . \tag{2.8}$$

The tight–binding approach

In the following we discuss the tight–binding approach to calculate the spin splitting of the energy bands in a III–V SC based QW structure. As already mentioned at the beginning of this section this microscopic theory utilizes a universal Hamiltonian. We define $\boldsymbol{z}$ to be the growth direction of a [001] grown heterostructure with 2DES and the x–axis along the [110] direction. For the nth non–degenerate energy band the relativistic Hamiltonian matrix close to the Brillouin zone center reads

$$H(nk) = \frac{\hbar^2(k_x^2 + k_y^2)}{2m^*} \mathbf{1} + \alpha_{BIA}(-k_y\sigma_x - k_x\sigma_y) + \alpha_{SIA}(k_y\sigma_x - k_x\sigma_y) \ , \tag{2.9}$$

were $\mathbf{1}$ is a 2×2 unity matrix. The constants α_{BIA} and α_{SIA} are already introduced in the subsection about the $\boldsymbol{k} \cdot \boldsymbol{p}$ model, but the tight–binding calculations reveal a substantially different behavior of these parameters [Maj02]. The $\boldsymbol{k}$ dependent energy splitting results from the eigenvalues of the Hamiltonian

$$\Delta E_{BIA,\ SIA} = 2\sqrt{(\alpha_{BIA}^2 + \alpha_{SIA}^2) - 4\alpha_{BIA}\alpha_{SIA}k_xk_y} \ . \tag{2.10}$$

The constants α_{BIA} and α_{SIA} are determined by calculating the band energy splittings in x and y direction in the limit of $\boldsymbol{k} \longrightarrow 0$. The result contains the influence of *all* energy bands. The spin splitting and the relative contributions of BIA and SIA depend strongly on the asymmetry of the conduction band wave function within the QW. This asymmetry is dominated by asymmetric chemical bonds in heterostructure interface layers and is *not* caused by macroscopic electric fields [Maj00]. Thus the design of the heterostructure with respect to material composition and layer thickness is crucial.

Detailed calculations yield the following facts [Vog07]: α_{BIA} is always nonzero and scales with the spin–orbit coupling of the QW material. α_{SIA} reflects the asymmetry of the conduction band wave function and thus is maximal in so–called no–common–atom QW like AlSb/InAs/GaSb or in QW with different barrier heights. For fully symmetric or very wide QW α_{SIA} is zero. α_{BIA} always exceeds α_{SIA}.
This statement conflicts with results from $\boldsymbol{k}{\cdot}\boldsymbol{p}$ theory where the SIA splitting mechanism is predicted to be dominant for 2DES with small band gaps [Lom88]. This is confirmed experimentally by S. D. Ganichev et al. [Gan04] who determined $\alpha_{SIA}/\alpha_{BIA}$ to be 2.15 for an InAs QW. In [Mei07] $|\alpha_{SIA}| \,/\, |\alpha_{BIA}| = 1.1$ is reported for GaAs/InGaAs QW which exhibit larger band gaps than InAs QW. It is important to note that the latter results were obtained in transport experiments, where $\boldsymbol{k} \longrightarrow 0$ is not given.

2.2.2 Tunability of the spin–orbit coupling

In this subsection we discuss the influence of different parameters on the spin–orbit coupling. They address the design of the QW, i.e. the choice of materials and its width. Further we discuss the influence of an externally applied electric field and of the charge carrier density. The coupling strength is expressed by the two constants, α_{BIA} and α_{SIA} or by a superposition α (see section 2.2.1).

In table 2.11 the α parameters and the electron mobility μ for typical 2DES structures are displayed. If a range is given, the value was tuned in the experiment. The particular tuning mechanism is explained in the corresponding reference.

2DES structure	**α (eVÅ)**	**μ (cm^2/Vs)**	**reference**
InGaAs/InAs/InGaAs	0.21–0.45	160 000	[Gru00], [Hu03]
InAlAs/InGaAs/InAlAs	0.06–0.092	36 500	[Nit97]
GaAs/InGaAs	0.0015	10 600	[Mei07]
AlGaAs/GaAs	0.0006	1 600 000	[Sti07], [Kor07]
SiGe/Si/SiGe	0.0055	200 000	[Wil02]
InP/InGaAs/InP	0.06–0.15	200 500	[Eng97]

(2.11)

Values for further heterostructures are given in [Aws02] and in [Fab07] on page 682.

Dependence on the quantum well design

Table 2.11 indicates a variation of the experimentally determined coupling parameters by three orders of magnitude. One can see that α depends crucially on the materials that form the QW. This is confirmed theoretically in [Maj02] and further, a strong dependence on the QW width is predicted. For widths below 20 layers of GaAs the spin–orbit coupling α strongly increases for GaAs based III–V SC heterostructures. Figure 2.6 illustrates this dependence for a symmetrically grown QW structure. For $n > 50$, α_{BIA} and α_{SIA} saturate. This results from the fact that the conduction band

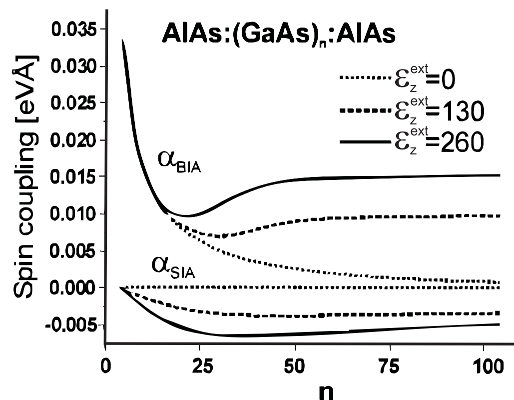

Figure 2.6: Calculated constants α_{BIA} and α_{SIA} for a AlAs/GaAs$_n$/AlAs heterostructure for different external electric fields ε_z^{ext} in (kV/cm) applied perpendicular to the layers. A tight–binding approach was used. The variable on the x axis is the thickness of the quantum well in atomic layers n. The graph is taken from [Maj02].

wave function is mostly localized at one side of the QW as shown in the middle panel of figure 2.4. Enlarging the width of the well beyond $n = 50$ does not influence the coupling parameters anymore, because the prolongation of the well can not be "seen" by the wave function. In figure 2.6, α_{BIA} and α_{SIA} are calculated for three different external electric fields ε_z^{ext}. This dependence is discussed in the next subsection. For $\varepsilon_z^{ext} = 0$ no structure asymmetry is induced, hence the SIA term is zero. For no–common–atom interfaces and ultra short QW α_{SIA} is high and thus, for these QW the highest spin splittings are predicted [Maj02] [Vog07].

In a different approach G. Lommer et al. investigated the dependence of the spin splitting on the energy gap E_g of SC [Lom88]. They found that α_{SIA} is an inverse function of E_g and that the SIA based splitting mechanism becomes dominant in narrow gap SC systems. This results from $\boldsymbol{k} \cdot \boldsymbol{p}$ theory calculations, where the matrix element that quantifies the Rashba spin–orbit interaction increases more rapidly than the BIA spin splitting matrix element when going to smaller band gaps. Thus, in GaAs based 2DES the contributions are of the same order of magnitude, while in InAs heterostructures the SIA mechanism dominates [Ras03]. A similar conclusion can be drawn from [Fab07], where (on page 694) a strong increase of both, α_{SIA} and α_{BIA} is calculated for $E_g < 1$ eV, whereas for larger energy gaps a saturation of the spin–orbit coupling parameters at low values is shown.

These findings can be explained qualitatively using the energy band structure model: The smaller the band gap of the QW material, the higher the band discontinuities at the interfaces to the barrier materials [Las85]. And, as illustrated in figure 2.4, this induces higher asymmetric electric field peaks from the valence band which cause the spin splitting in the conduction band.

Electric field dependence

The concept of a spin field–effect transistor as described in section 2.5 exploits the manipulation of spins within a 2DES. This is realized by tuning the spin–orbit coupling with an electric field ε^{ext}.

The $\boldsymbol{k} \cdot \boldsymbol{p}$ model presented in the previous subsection relates the spin splitting of the conduction band to the resulting asymmetric electric field from the valence bands $\left\langle \varepsilon_z^V \right\rangle$ (see page 9). One can determine the influence of an external electric field ε_z^{ext} on $\left\langle \varepsilon_z^V \right\rangle$. According to [Win03] ε_z^{ext} is weighted with a prefactor including the conduction and valence band offsets Σ_C and Σ_V. The effective electric field from the valence band that causes the splitting of the conduction band reads

$$\left\langle \varepsilon_z^V \right\rangle_C = \frac{\Sigma_C + \Sigma_V}{\Sigma_C} \left\langle \varepsilon_z^{ext} \right\rangle \ . \tag{2.12}$$

Calculations based on $\boldsymbol{k} \cdot \boldsymbol{p}$ theory predict that the spin–orbit coupling parameter α in equation 2.3 depends linearly on an electric field ε_z through the effective energy gap and the effective mass [Aws02].

A further result from $\boldsymbol{k} \cdot \boldsymbol{p}$ theory is that the BIA spin splitting is essentially a fixed material parameter but its relevance varies with the width of the QW and the wave vector $\boldsymbol{k}$ [Win04]. This qualitative argument is confirmed quantitatively in tight–binding calculations for small QW widths [Maj02]: In figure 2.6 one can observe that α_{BIA} does not change for different electric fields up to a well width n of about 15 layers. But for wider QW α_{BIA} and not α_{SIA} dominates the electric field dependence.

The first experiment that demonstrated the influence of an electric field on the spin splitting of the conduction band was performed by J. Nitta et al. [Nit97] on $In_{0.53}Ga_{0.74}As/In_{0.52}Al_{0.48}As$ heterostructures. They induced an external electric field with a single field electrode. This method also affects the charge carrier density n_{2D}. They showed that α varies by a factor of 1.5 with a change of the gate voltage in the range of 2.5 V. This coincides with a variation of n_{2D} from 2.4×10^{12} to 1.6×10^{12} cm^{-2}. They argue that the observed tuning of α is caused by the variation of the electric field rather than the change of n_{2D} or m^*. Although a dependence of α on m^* is documented in [Fab07].

Dependence on electron density

G. Engels et al. explain the change of α with the spin–orbit coupling originating from the QW plus an additional contribution that originates from the leakage of the electron wave function into the barrier layers in a QW with a finite barrier height [Eng97]. To calculate the spin–orbit interaction parameter from their experimental data they use the following expression:

$$\alpha = \frac{(n^+ - n^-)\hbar^2}{m^*} \sqrt{\frac{\pi}{2(n_{2D} - n^+ + n^-)}} \ , \tag{2.13}$$

where n^+ and n^- represent the populations of the spin–split subbands. According to this equation, the spin–orbit coupling depends on the carrier density n_{2D}. But similar to the experiment of J. Nitta et al. [Nit97] they can not distinguish whether the variation of α is caused by the applied electric field which tilts the band structure or by the change of n_{2D}.

D. Grundler presented an experiment on InAs heterostructures [Gru00] to distinguish between these two influences. External electric fields were induced by applying front and back gate voltages. By this means he adjusted the electric field and n_{2D} in the QW independently. They studied the behavior of α as a function of ε_z^{ext} and as a function of n_{2D} *independently.* By a variation of ε_z^{ext} of about 4.6 kV/cm he tuned the

Rashba parameter by 20 %. Calculations of R. Winkler revealed that the influence of external electric fields on the spin splitting of InAs 2DES is larger compared with other materials [Win03]. The variation of n_{2D} in D. Grundler's experiment changes α by more than a factor of 2. In [Win03] two different cases for the relation between α and n_{2D} are presented: First n_{2D} is varied with an external electric field (as in [Nit97], [Eng97] and [Gru00]). For this case the normalized difference of populations of the spin–split subbands is $(n^+ - n^-)/n_{2D} \propto \sqrt{n_{2D}}$ in accordance with an earlier calculation by R. Lassnig [Las85]. Second, n_{2D} is varied but the net electric field is kept constant (as in [Gru00]). Then the proportionality changes to $(n^+ - n^-)/n_{2D} \propto 1/\sqrt{n_{2D}}$. These relations were qualitatively confirmed in the experiment of D. Grundler.

2.2.3 Spin relaxation mechanisms in semiconductors

A spin polarization in a nonmagnetic SC is not an equilibrium state. The polarization randomizes with time via different spin relaxation mechanisms (SRM). The two most relevant mechanisms for the devices discussed in this thesis are described in this subsection. First we explain the Elliott–Yafet (EY) mechanism and then the D'yakonov–Perel' (DP) mechanism. The Bir–Aronov–Pikus (BAP) spin scattering mechanism, caused by electron–hole exchange interaction in p–doped SC, as well as hyperfine interaction mechanisms are not explained in detail. The latter mechanism leads to spin dephasing through magnetic interaction between the electron spin and the magnetic moment of nuclei.
A detailed overview of spin scattering mechanisms is published by I. Žutić et al. [Zut04] and in [Fab07].

One distinguishes between the spin diffusion or relaxation time T_1 and the spin dephasing time T_2. T_1 indicates how long spins keep their polarization in the case of diffusive transport where scattering processes occur. T_2 specifies the depolarization time of an unbiased spin polarized state, e.g. generated by optical excitation. In the latter case spins that initially precess in phase loose their phase after T_2 due to spatial and temporal fluctuations of the precessing frequencies.
In some cases it is indiscriminable whether diffusion or dephasing is involved. Then both mechanisms are referenced as spin relaxation time τ_s.

Elliott–Yafet

This SRM was first reported by R. J. Elliott [Ell54]. For nonzero $\boldsymbol{k}$ the electron states are superpositions of spin–up and spin–down states for a given quantization axis due to spin–orbit coupling. With each momentum scattering process there is a finite probability for a spin flip. Momentum scattering occurs e.g. due to electron—phonon interaction (at high temperatures T) or due to impurities (dominating at low T). The scattering potential must be spin dependent in order to enable a spin flip. This is mostly the case for heavy impurities and ions.

Generally, one can state, the shorter the momentum scattering time the faster the spin relaxation. This is reflected in the Elliott relation [Ell54]. It is an estimation of the relaxation time based on the momentum relaxation time τ_m:

$$\tau_s \approx \frac{\tau_m}{(\Delta g)^2} \ . \tag{2.14}$$

Δg is the difference between the material specific electronic g factor and the free electron factor $g_0 = 2.0023$. In [Fab07] $\tau_s \approx 10^5 \cdot \tau_m$ is mentioned to be a typical relation.

Y. Yafet derived the temperature dependence of this relaxation mechanism on the basis of the temperature dependence of the electrical resistivity [Yaf63]. In this publication he proves that $1/T_1 \sim T^5$ for metals at low temperatures, exactly as for the electrical resistivity. The same approach applied to SC yields $T_1(\Delta g)^2 \sim T^{-7/2}$ for SC with direct band gaps and $T_1(\Delta g)^2 \sim T^{-5/2}$ for indirect band gaps.

D'yakonov–Perel'

The SRM described by M. D'yakonov and V. Perel' is based on spin–orbit coupling effects. As described previously in section 2.2.1 a $\boldsymbol{k}$ dependent effective magnetic field $H_{eff}(\boldsymbol{k})$ is present in inversion asymmetric SC. This H_{eff} forces the electron spin momentum to precess with the Larmor frequency

$$\omega(\boldsymbol{k}) = \gamma\mu_0 H_{eff}(\boldsymbol{k}). \tag{2.15}$$

The gyromagnetic ratio γ is defined as the electron g factor times the Bohr magneton μ_B divided by Planck's constant over 2π: $\gamma = g\mu_B/\hbar$. Hence the precession frequency alters with changes in $\boldsymbol{k}$ due to momentum scattering processes. We consider all individual electron spins as an ensemble and define an average frequency ω_{ave}. In the case that $\omega_{ave}\tau_m \lesssim 1$ the electron spins can not perform a complete precession before being scattered into another momentum state. In this limit one can understand the DP mechanism as a random walk of the spin precession. For this condition, in [D'y71] the spin dephasing time τ_s is estimated to be

$$\frac{1}{\tau_s} \approx \omega_{ave}^2 \tau_m\ . \tag{2.16}$$

The most important difference compared with the EY mechanism is the inverse dependence on τ_m. This means that for high momentum scattering rates the EY mechanism dominates, whereas for low scattering rates the DP mechanism is more effective. The EY mechanism is a frequency conserving process and the dephasing takes place only in the short time *during* a scattering process. In contrast, the DP mechanism randomizes spin polarizations *between* the scattering processes. Thus, the purer the crystal and the longer the mean free paths of the electrons, the more efficient is the DP mechanism.

In [Zut04], [Tac99] and [Son02] the relevance of the SRM are discussed for various materials and parameters. An overview is presented in table 2.17. Note that the dominant SRM for special heterostructure designs might be different.

Material / Conditions	**Dominant SRM**
metals	EY
n–type III–V small-gap SC (e. g. InAs), bulk and QW, $T < 5$ K	EY
n–type III–V middle-gap SC (e. g. GaAs), bulk and QW, $T \gtrsim 5$ K	DP
n–type III–V middle-gap SC (e. g. GaAs), bulk and QW, $T < 5$ K	Bir–Aronov–Pikus [Bir76]
p–type III–V SC, bulk and QW	Bir–Aronov–Pikus and DP

(2.17)

From this table one can deduce that the effectiveness of SRM is temperature dependent. Further it depends on the carrier density, the external magnetic field and strain [Zut04].

Latest experiments in the research group of C. Schüller [Sti07] proved that the spin dephasing time T_2 in a GaAs based QW structure depends on the orientation of the spins relative to the crystal axes. They showed for GaAs 2DES heterostructures an increased spin dephasing time by a factor of two in $\left[1\bar{1}0\right]$ direction compared with the [110] direction. This phenomenon is explained with a spin relaxation mechanism proposed by Wu et al. [Wu00]. This mechanism is based on the $\boldsymbol{k}$ dependence of the transition energies between opposite spin states, which results in an inhomogeneous broadening of spin transitions. In [Sti07] the inhomogeneous broadening is provided by the $\boldsymbol{k}$ dependent Rashba and the Dresselhaus spin–orbit couplings and leads to a spin dephasing. As the couplings are of different strengths in $\left[1\bar{1}0\right]$ and [110] direction, the spin dephasing times differ.

2.2.4 The spin pumping effect and the spin battery

In the so–called macro–spin model the ensemble of microscopic magnetic moments of a FM is described by a large vector $\boldsymbol{M}$. In the presence of an effective magnetic field $\boldsymbol{H}_{\mathit{eff}}$ that includes external, demagnetization and anisotropy fields, the time evolution of $\boldsymbol{M}$ is described by

$$\frac{d\boldsymbol{M}}{dt} = -\gamma\mu_0 \left[\boldsymbol{M} \times \boldsymbol{H}_{\mathit{eff}}\right] + \frac{\alpha_G}{M_{sat}} \left[\boldsymbol{M} \times \frac{d\boldsymbol{M}}{dt}\right] . \tag{2.18}$$

A first version of this relation was derived by L. D. Landau and E. M. Lifshitz [Lan35] [Lan65]. The first term on the right–hand side describes a torque $\boldsymbol{\tau}$ on $\boldsymbol{M}$ and determines the resonance frequency of the resulting precessional motion of $\boldsymbol{M}$. The second term was added later by T. L. Gilbert [Gil04] and thus is commonly called the Gilbert damping term with the phenomenological damping parameter α_G. It includes the saturation magnetization M_{sat}. A detailed overview of magnetization dynamics can be found in the book of B. Hillebrands and K. Ounadjela [Hil02].

It was found experimentally that the damping and thus α_G in a FM/NM bilayer is higher than in single–layer FM [Kat00]. In the latter publication J. A. Katine et al. demonstrate in a spin transfer torque experiment that spin momentum can be transferred into a neighboring FM. The transfer of spins is also called spin pumping. Y. Tserkovnyak et al. use the picture of spin transfer to explain the increased damping in FM/NM hybrid structures [Tse02]. They show that the reduction of precessional motion of $\boldsymbol{M}$ in a FM can be explained by a spin current $\boldsymbol{I}_s$ into an adjacent NM layer. A spin current can be understood as the diffusion of spin polarized electrons into the NM and each electron carries a spin momentum (or torque) of $\hbar/2$.

In an experiment by the group of B. J. van Wees such a spin pumping, or spin current, was detected electrically [Cos06a]. A precession of $\boldsymbol{M}$ in a nanoscopic FM was driven by a rf magnetic field at a frequency ω. They attached NM leads with different spin dephasing lengths to the FM and measured the voltage V_{dc} across the device. V_{dc} increases, if ω equals the FMR frequency of the FM. As a rf magnetic field produces a dc voltage, this type of NM1/FM/NM2 hybrid structure is also called a spin battery device [Bra02].

To explain this voltage, we follow the argumentation in [Wan06], [Bra00] and [vS87]. A detailed summary can be found in the review article by Y. Tserkovnyak et al. [Tse05]. We consider a single FM/NM interface as shown in figure 2.7 and assume a precessing magnetization $\boldsymbol{M}$ in the FM around $\boldsymbol{M}_0$. $\boldsymbol{M}_0$ is the equilibrium magnetization which

points in the direction of $\boldsymbol{H}_{eff}$. $\boldsymbol{M}$ is excited by an applied rf magnetic field $\boldsymbol{h}_{rf}$ that exerts a torque $\boldsymbol{\tau}$ on $\boldsymbol{M}$ and causes a motion $d\boldsymbol{M}/dt$ according to equation 2.18. The precession angle θ can be tuned by the amplitude of $\boldsymbol{h}_{rf}$. In the presence of damping

Figure 2.7: The process of spin transfer across a FM/NM interface is illustrated schematically. See text for details.

the precession tends to relax, what is described by the damping term in equation 2.18[2]. As explained above, damping can also be understood as the emission of a spin current. Its spin points perpendicular to $\boldsymbol{M}$ and $d\boldsymbol{M}/dt$ towards the center of the precession cone (see figure 2.7). In the bulk FM these spins dephase rapidly as no coherent states exist perpendicular to $\boldsymbol{M}$. But close to the interface to a NM, spins from within the ferromagnetic coherence length can diffuse into the NM. Via this mechanism the damping is enhanced as the torque of the precession is transferred into the NM by the electron spins. The spin current $\boldsymbol{I}_s^{pump}$ from the FM into the NM was calculated by Y. Tserkovnyak et al. [Tse02] for the case of resonant precession. It is given by

$$\boldsymbol{I}_s^{pump} = \frac{\hbar}{4\pi}\left(\mathrm{Re}\, g^{\uparrow\downarrow}\boldsymbol{M}\times\frac{d\boldsymbol{M}}{dt} + \mathrm{Im}\, g^{\uparrow\downarrow}\frac{d\boldsymbol{M}}{dt}\right) .$$

We introduced the so–called (complex) spin–mixing conductance $g^{\uparrow\downarrow}$. It describes the transport of spins that are noncollinear to $\boldsymbol{M}$ across an interface. For most systems the imaginary part can be disregarded [Bra02] so in the following we assume $g^{\uparrow\downarrow} = \mathrm{Re}\, g^{\uparrow\downarrow}$. The mixing conductance in the diffuse limit depends on the conductance of the NM only. Hence, $g^{\uparrow\downarrow} = g^{NM}$ which is a consequence of the relaxation of spins noncollinear to $\boldsymbol{M}$ in the FM [Bra00]. For a ballistic contact Brataas et al. find for the spin dependent interface conductances $g^{\uparrow(\downarrow)} = (e^2/h)N^{\uparrow(\downarrow)}$, where N is the (spin dependent) number of transmitted channels, and $g^{\uparrow\downarrow} = \max(g^{\uparrow}, g^{\downarrow})$. This is why the mixing conductance can be approximated as twice the Sharvin conductance G_{Sh} [Sha65] in the ballistic transport regime [Wan06]. The 2D Sharvin conductance is defined by

$$G_{Sh}^{2D} = \frac{2e^2}{h}\frac{k_F l_c}{\pi} , \tag{2.19}$$

where l_c is the length of the contact and k_F the 2D Fermi wave vector. Calculations on spin dependent interface resistances for various material combinations can be found

[2] A dynamic equilibrium is reached if the precession is permanently excited by an rf magnetic field.

in [Xia01].
As depicted in figure 2.7 the polarization of $\boldsymbol{I}_s^{pump}$ has dynamic components perpendicular to $\boldsymbol{M}_0$ and a static component parallel to $\boldsymbol{M}_0$. In the NM no preferred spin direction exists, thus, all spin components enter the NM. The time average of the dynamic components is zero if the dimensions of NM L_{NM} exceed the spin averaging length l_ω. This reduces $\boldsymbol{I}_s^{pump}$ and consequently can be treated like an additional resistance. Including this aspect the effective interface conductances are

$$g_\omega^{\uparrow(\downarrow)} = \frac{g^{\uparrow(\downarrow)}}{1 + g^{\uparrow(\downarrow)}/g_\omega} \text{ and } g_\omega^{\uparrow\downarrow} = \frac{g^{\uparrow\downarrow}}{1 + g^{\uparrow\downarrow}/g_\omega} \ , \tag{2.20}$$

where the conductance $g_\omega = \sigma_{NM} A/l_\omega$ represents the bulk conductance through the area A of a NM of length l_ω. Provided that the spin–flip relaxation rate in the NM is smaller than the injection rate, $\boldsymbol{I}_s^{pump}$ leads to the build–up of a spin accumulation $\boldsymbol{\mu}_s^{NM}$ (in units of $\hbar$) in the NM close to the interface. Its time averaged vector points along $\boldsymbol{M}_0$. $\boldsymbol{\mu}_s^{NM}$ either relaxes within the spin diffusion length λ_{NM} or flows back into the FM as $\boldsymbol{I}_s^{back}$. The time averaged spin accumulation in the NM close to the FM/NM interface reads [Bra02]

$$\boldsymbol{\mu}_s^{NM} = \hbar\omega \frac{\sin^2\theta}{\sin^2\theta + \eta} \ .$$

where η is a reduction factor that includes the ratio between injection and spin relaxation times and θ is the precession cone angle. A detailed evaluation of this term, separated into $\eta_{FM}^{\uparrow\downarrow}$ and η_{NM} is provided in [Wan06].
In the following we discuss some important aspects concerning $\boldsymbol{I}_s^{back}$. In the limit of a high spin–flip rate in the NM, i.e. the MN is a good "spin sink", the spin accumulation in the NM relaxes rapidly. Then $\boldsymbol{I}_s^{back} \to 0$ and $\boldsymbol{I}_s \simeq \boldsymbol{I}_s^{pump}$. For smaller spin–flip rates in the NM, i.e. long λ_{NM}, a spin accumulation $\boldsymbol{\mu}_s^{NM}$ builds up which drives the backflow current. $\boldsymbol{I}_s^{back}$ is spin polarized along $\boldsymbol{M}_0$ and faces spin dependent interface and bulk conductances in the FM. As illustrated in figure 2.7 only the component of $\boldsymbol{I}_s^{back}$ parallel to the instantaneous $\boldsymbol{M}$ can enter the FM. The component transverse to $\boldsymbol{M}$ dephases in the FM within the spin scattering length (typically an atomistic length scale for Fe, Ni, Co) since no coherent states exist for electrons with transverse spins. This is equal to an absorption of the transverse component of $\boldsymbol{I}_s^{back}$ in the FM. So the spin current from the NM into the FM reads [Bra02]

$$\boldsymbol{I}_s^{back} = \frac{g_\omega^{\uparrow\downarrow}}{2\pi n} \left[\boldsymbol{\mu}_s^{NM} - \boldsymbol{M}\left(\boldsymbol{M} \cdot \boldsymbol{\mu}_s^{NM}\right)\right] \ ,$$

where n is the one–spin density of states. Thus a nonzero net spin current $\boldsymbol{I}_s = \boldsymbol{I}_s^{pump} - \boldsymbol{I}_s^{back}$ can occur. $\boldsymbol{I}_s$ gives rise to a nonequilibrium spin accumulation $\boldsymbol{\mu}_s^{FM}$ in the FM, which adjusts such that no net charge current flows in equilibrium. The latter consideration allows to calculate the charge chemical potential difference $\Delta\mu_0$ across the FM/NM interface. This is done in the publication of X. Wang et al. [Wan06]. In a general form it reads

$$\Delta\mu_0 = \frac{p_\omega}{2} \left(\boldsymbol{\mu}_s^{NM} \cos\theta - \boldsymbol{\mu}_s^{FM}\right) \ . \tag{2.21}$$

The interface polarization $p_\omega = \left(g_\omega^{\uparrow} - g_\omega^{\downarrow}\right) / \left(g_\omega^{\uparrow} + g_\omega^{\downarrow}\right)$ is introduced. In the limit of

large spin–flip in the FM and small θ equation 2.21 it is approximated by

$$\Delta\mu_0 \simeq \frac{p_\omega}{2}\hbar\omega\frac{g_\omega^{\uparrow\downarrow}}{\left(1+\frac{g_{NM}}{g_{FM}}\right)(1-p_\omega^2)\left(g_\omega^{\uparrow}+g_\omega^{\downarrow}\right)+2g_{NM}}\theta^2 \ . \tag{2.22}$$

The conductances g_{NM} and g_{FM} refer to the bulk values of the NM and the FM over the distance of the respective spin diffusion length λ_{NM} and λ_{FM}. One obtains the voltage drop across the interface by dividing the chemical potential difference by the electron charge

$$V_{dc} = \frac{\Delta\mu_0}{e}. \tag{2.23}$$

We point out that according to equation 2.22 the voltage drop depends crucially on the spin dependent conductivities $g_\omega^{\uparrow}$ and $g_\omega^{\downarrow}$ in the FM, on the bulk conductivities and and on the interface mixing conductance $g_\omega^{\uparrow\downarrow}$. Further a linear dependence on the rf frequency and a quadratic dependence on the precession angle is predicted.

2.2.5 Spin filtering at ferromagnet/semiconductor interfaces

G. Schmidt et al. pointed out that the large difference in conductivities of FM and SC, and in particular the spin–independent conductivity of SC is a basic obstacle for efficient spin injection in FM/SC devices [Sch00]. In the latter model the spin–split band structures were not included.

A. Fert and H. Jaffrès extended this model by introducing spin dependent interface resistances [Fer01]. Their result clearly indicates that the basic obstacle for spin injection is no longer valid if tunnel barriers or significant spin dependent resistances are inserted between the FM and the SC.

The mechanism of spin filtering at an interface between a FM and a 2DES in a III–V SC heterostructure was investigated by D. Grundler [Gru01b]. He pointed out that a FM/2DES interface can act as a spin filter due to the band structure mismatch of the involved materials. The calculations were performed using the Landauer–Büttiker formalism in the ballistic transport regime [Bue85]. The basic parameters are the different Fermi wave vectors $\boldsymbol{k}_F$ for majority ($\uparrow$) and minority ($\downarrow$) spins at the Fermi energy in the FM. In principle the spin–split states of the 2DES (see section 2.2.1) must be considered as well, but, like in [Gru01a], are neglected for the present discussion of spin filtering. In the latter reference a parabolic subband dispersion was assumed for the 2DES with $\boldsymbol{k}_F = \sqrt{2\pi n_{2D}}$, where n_{2D} is the total 2D charge carrier density. With the definition of the Fermi velocity $v_F = \hbar k_F^{(\uparrow,\downarrow)}/m^*$ using the spin dependent wave vector $k_F^{(\uparrow,\downarrow)}$ and the effective masses $m^*_{(FM,SC)}$ of the two materials the ratios $r_v^{(\uparrow,\downarrow)} = v_{F,SC}/v_{F,FM}^{(\uparrow,\downarrow)}$ can be calculated for the $\uparrow$ and the $\downarrow$ spins of the FM. These two ratios determine the transmission probabilities for electrons through the FM/SC interface for the spin orientations $\uparrow$ and $\downarrow$

$$T^{(\uparrow,\downarrow)} = \frac{1}{1+\left(\frac{(r_v^{(\uparrow,\downarrow)}-1)^2}{4r_v^{(\uparrow,\downarrow)}}\right)}. \tag{2.24}$$

For zero temperature, the Landauer conductance formula reads

$$G = \frac{e^2}{h}\sum_a T_a \tag{2.25}$$

where T_a are the transmission probabilities for all spin–non–degenerate modes participating in electron transport. In a single conductance mode, which can be realized with a FM/2DES interface, only the two $T^{(\uparrow,\downarrow)}$ have to be considered. In [Gru01b] and [Gru01a] the relative conductance change $\Delta G/G_{ave}$ is calculated as a function of n_{2D} for a $Ni_{80}Fe_{20}$/2DES (InAs based) interface and for a Fe/2DES. The carrier density is experimentally tunable via a gate voltage or via the persistent photo effect. ΔG is the difference in conductance that occurs if the magnetization of the FM contact is reversed. The characteristics of the $\Delta G/G_{ave}$ curves changes drastically if the spin splitting of the 2DES is included in the calculation.

In an earlier work M. Johnson also calculated $\Delta G/G_{ave}$ [Joh98] for FM/2DES heterostructures. He included the difference in conductances for $\uparrow$ and $\downarrow$ spin states in the FM but not the band structure mismatch at the interface. He extended his model to the diffusive regime by introducing a spin scattering length λ_s over which spin orientation becomes random. For the switching of one FM's magnetization he obtains a relative resistance change of

$$\frac{\Delta R}{R_{ave}} = 2\exp\left(-\frac{L_x}{\lambda_s}\right)\eta^2 \tag{2.26}$$

where L_x is the 2DES channel length and η the spin polarization of the current crossing the FM/2DES interface.

A general quantum mechanical approach to calculate spin injection was made by C.–M. Hu et al. [Hu01a]. They included the effect of a mismatch of the contact's band structures, spin polarization in the contacts, and interface scattering. They also used the ansatz of R. Landauer and calculate the transmission coefficients as the probability amplitudes for the electron wave functions to traverse the interface. As input parameters they also used the ratios of the effective masses and of the Fermi energies, as well as the ratio of spin polarizations on both sides of the interface. Further a parameter Z_0 describing elastic interface scattering is included. An important result is that Z_0 has a dominant influence on spin injection across a FM/SC junction.

This influence was further investigated by M. Zwiersycki et al. [Zwi03] and O. Wunnicke et al. [Wun02]. They modeled a specular Fe/InAs interface using a tight–binding method in the ballistic limit. Thus the full electronic band structures are included to derive the interface conductance. They find a strong increase of the conductance difference between electrons with majority and minority spins with a raise of the Fermi energy. For a Fermi energy just above the conductance band minimum the InAs behaves metallic. For this regime the calculation yields a current polarization by the interface of up to 98 %.
By substituting In or As atoms with Fe atoms at the interface, an interface disorder is simulated. For only 12 % of substituted atoms the polarization effect almost vanishes. This implies that the spin filtering property of a Fe/InAs interface is very sensitive to interface disorder what has to be considered in the preparation of spin injection devices.

Further evidence for the sensitivity of spin effects on interface resistance is given in a very recent publication [Koo08]. The authors investigate the spin transport signals of a FM/2DES/FM device as a function of the interface resistance R_i. Typical values of R_i to observe clear spin signals for a micron–sized spin valve device are about 0.5 to 250 Ω. This range is between the transparent and the tunneling regime. For experimental reasons they do not favor the tunnel barrier to exhibit the most pronounced spin signals what contradicts the conductivity mismatch theory. They state that due to its high

resistance a tunnel barrier produces a high background noise level. They conclude that the junction needs to be as clean as possible in order to realize high transport efficiency.

2.3 Magnetoresistance effects

In the following subsections some magnetoresistance (MR) effects that are relevant for the present work are discussed. In the first subsection the AMR effect is explained which is a transport phenomenon in FM. The in–plane Hall effect is of the same origin and is reviewed, together with the anomalous Hall effect, in the subsequent subsection. Then we discuss MR effects in SC containing a 2DES in a magnetic field, followed by MR effects in hybrid structures. We focus on the EMR effect and the GMR effect in NM/FM and NM/SC structures.

2.3.1 The anisotropic magnetoresistance effect

In addition to the well–known ordinary MR effect which can be observed in metals, FM have an additional term depending on the relative orientation of the magnetization $\boldsymbol{M}$ and the current $\boldsymbol{j}$. Pioneering experiments to explore this AMR effect were performed by J. Smit in 1951 [Smi51]. In these experiments the MR of different ferromagnetic NiFe alloys and NiCo alloys and, as a reference, a NiCu alloy was measured. The FM were magnetized in a magnetic field. Then $\boldsymbol{j}$ was applied in two directions: parallel and perpendicular to $\boldsymbol{M}$ and the voltage drop was measured to calculate the resistance. They observed a difference between longitudinal and transversal resistance and attributed this to the spin–orbit interaction. Figure 2.8 was adapted from [Jao77] and shows typical AMR curves. To explain this behavior they performed calculations of

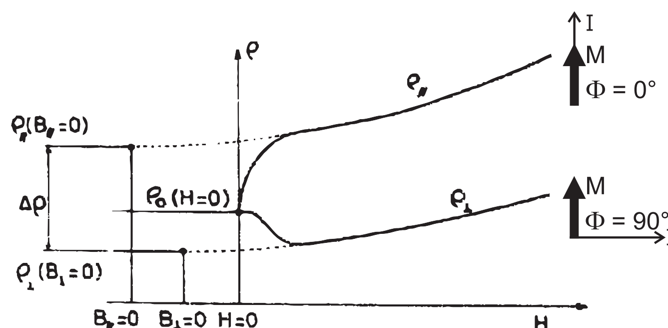

Figure 2.8: Schematic MR curve of a FM sample as a function of applied magnetic field for two angles Φ between the magnetization M and the current I. The magnitude of the AMR effect is obtained by extrapolation. The graph is taken from [Jao77].

the transition probability for an s electron into a d state based on perturbation theory. They found a mixing of parallel and antiparallel states in the d band. This goes beyond our assumptions in section 2.1.2. As a consequence, even at $T = 0$ K, unoccupied parallel d states are present. Further they argue that these holes are not equally distributed over the five possible d orbits, but that there is a deficit of hole–orbits perpendicular to

the magnetization. Accordingly, the scattering rate is low for $\boldsymbol{M} \perp \boldsymbol{j}$. Thus the device resistance in this configuration is lower compared with the parallel orientation $\boldsymbol{M} \parallel \boldsymbol{j}$.

An extensive investigation of the AMR effect in Ni alloys was published by the group of A. Fert in [Jao77]. For a fully magnetized ferromagnetic polycrystal the resistivity is of the form

$$\rho(\Phi) = \rho_0 + \Delta\rho(\cos^2\Phi - \frac{1}{3}) \ . \tag{2.27}$$

$\Delta\rho$ is explained in figure 2.8 and ρ_0 is the residual resistivity of the considered material. So they find a cosine squared behavior of ρ with the angle Φ between $\boldsymbol{M}$ and $\boldsymbol{j}$.

In a more general description the resistivity is written as a tensor $\boldsymbol{\rho}$. For the following we define the x–z plane as the plane of a thin FM film. The current density is given by $\boldsymbol{j} = j(\sin\Phi, 0, \cos\Phi)$, assuming that $\boldsymbol{M}$ points in z direction. Then Ohm's law yields

$$\varepsilon = \boldsymbol{\rho} \cdot \boldsymbol{j} = \begin{pmatrix} \rho_\perp & 0 & 0 \\ 0 & \rho_\perp & 0 \\ 0 & 0 & \rho_\parallel \end{pmatrix} \begin{pmatrix} j\sin\Phi \\ 0 \\ j\cos\Phi \end{pmatrix} \ , \tag{2.28}$$

where $\rho_\perp$ ($\rho_\parallel$) is the resistivity for a current flowing perpendicular (parallel) to $\boldsymbol{M}$. To calculate the electric field component pointing in the film plane along current direction we multiply the electric field ε with the respective unit vector $\boldsymbol{j}/j = (\sin\Phi, 0, \cos\Phi)$ and obtain

$$\begin{aligned} \varepsilon_{AMR} &= \varepsilon^T \cdot \boldsymbol{j}/j = j\left[\rho_\perp + (\rho_\parallel - \rho_\perp)\cos^2\Phi\right] \\ &= j\left[\rho_0 + \Delta\rho\left(\cos^2\Phi - \frac{1}{3}\right)\right] \end{aligned}$$

where $\Delta\rho = \rho_\parallel - \rho_\perp$. This corresponds to the experimental finding in [Jao77] and determines the mean value of of the specific resistivity to $\rho_0 = \left(\rho_\perp + 2\rho_\parallel\right)/3$. The effect is symmetric with respect to $\boldsymbol{j}$. This means that ε_{AMR} is constant if $\boldsymbol{M}$ is rotated from an in–plane direction to an out–of–plane direction (with a finite y component) as long as Φ is unchanged.

2.3.2 The in–plane Hall effect and the anomalous Hall effect

Analog to the previous subsection we consider a FM film, extended in the x–z plane. Its magnetization $\boldsymbol{M}$ points in z direction and a current density $\boldsymbol{j}$ in the x–z plane. Φ is the angle between $\boldsymbol{j}$ and $\boldsymbol{M}$. If the film resistivity $\boldsymbol{\rho}$ exhibits an anisotropy as a result of the magnetization, the electric field ε is given by equation 2.28. To calculate the field ε_{IPHE} perpendicular to $\boldsymbol{j}$ and in the film plane we project ε onto this direction using the unit vector $(-\cos\Phi, 0, \sin\Phi)$

$$\varepsilon_{IPHE} = \varepsilon^T \begin{pmatrix} -\cos\Phi \\ 0 \\ \sin\Phi \end{pmatrix} = j\frac{\Delta\rho}{2}\sin(2\Phi) \tag{2.29}$$

with $\Delta\rho = \rho_\parallel - \rho_\perp$. For nonzero Φ we find a finite in–plane electric field perpendicular to $\boldsymbol{j}$. This effect is called in–plane Hall effect (IPHE). Pioneering investigations are published in [Ky66] and [Yau71]. The IPHE and the AMR effect are of the same physical origin and are calculated using the same resistivity tensor. Thus, ε_{IPHE} also

depends on the angle between $\boldsymbol{j}$ and $\boldsymbol{M}$ and is invariant with respect to rotations of $\boldsymbol{M}$ around $\boldsymbol{j}$ for constant Φ.

A further effect that leads to an electric field perpendicular to $\boldsymbol{j}$ in a FM is the so–called anomalous Hall effect (AHE) [Hal80]. This effect is analog to the ordinary Hall effect, but it depends on the magnetization $\boldsymbol{M}$ instead of the external magnetic field $\boldsymbol{H}$. In FMs the AHE typically dominates the ordinary Hall effect. The AHE can be expressed by adding the resistivity contributions ρ_{AHE} to the resistivity tensor as off–diagonal elements for $\boldsymbol{M}$ pointing in z direction. To focus on the AHE we disregard the diagonal components here. The electric field then takes the general form

$$\varepsilon_{AHE} = \boldsymbol{\rho} \cdot \boldsymbol{j} = \begin{pmatrix} 0 & -\rho_{AHE} & 0 \\ \rho_{AHE} & 0 & 0 \\ 0 & 0 & 0 \end{pmatrix} \begin{pmatrix} j \sin \Phi \\ 0 \\ j \cos \Phi \end{pmatrix} = \begin{pmatrix} 0 \\ j\,(\sin \Phi)\, \rho_{AHE} \\ 0 \end{pmatrix} . \quad (2.30)$$

ε_{AHE} has no components in the film plane. Thus, the in–plane projection preformed in equation 2.29 yields zero. In all other directions a finite contribution of ε_{AHE} is effective. Reversely spoken this means that in a magnetotransport experiment where the voltage is measured across a thin FM film a contribution of the AHE is only measurable if $\boldsymbol{M}$ has a finite component pointing out of the plane. Further, in contrast to the IPHE the AHE is not rotational symmetric for $\boldsymbol{M}$.

2.3.3 Magnetoresistance effects in a two–dimensional electron system

2DES are incorporated in the devices of this work. Thus it is important to discuss their behavior in magnetic fields in the context of magnetotransport experiments. Details about this topic are published in a review article by T. Ando, A. B. Fowler and F. Stern [And82] or in textbooks as e.g. [Iba99]. Here, we focus on the Landau quantization and the Shubnikov–de Haas oscillations resulting from quantization phenomena.

Landau quantization

We consider a SC heterostructure incorporating a QW where z is growth direction. The QW confines a 2DES in the x–y plane. The reduced extension in z direction leads to a quantization of energy E_i^z. For magnetic fields $\mu_0 \boldsymbol{H} = (0, 0, \mu_0 H_z)$ an additional quantization of the electrons' energy spectrum occurs. This is well known as the Landau quantization [Lan30]. The external magnetic field enters the Hamiltonian via a vector potential $\boldsymbol{A}$

$$\hat{\boldsymbol{H}} = \frac{1}{2m^*} (\boldsymbol{p} + e \cdot \boldsymbol{A})^2.$$

With the Landau gauging $\boldsymbol{A} = (0, \mu_0 H_z x, 0)$ the allowed energy levels can be calculated to

$$E_{i,j} = \hbar \omega_c \left(j + \frac{1}{2} \right) + E_i^z \qquad j = 0, 1, 2, ... \quad (2.31)$$

where $\omega_c = e\mu H_z / m^*$ is the cyclotron frequency of the electrons with reduced mass m^*. The Zeeman effect as mentioned in section 2.2.1 is neglected for simplicity. Its contribution was an additional energy splitting of each Landau level lifting the spin degeneracy. So one can understand the first term of equation 2.31 to be discrete Landau energy levels (or simply Landau levels) of orbital shape in $\boldsymbol{k}$ space. On these Landau levels the electrons condense in presence of $\boldsymbol{H}$ and orbit with ω_c.

The total electron density $D^{2D}(E) = dN/dE$ for one z–quantized energy level E_i^z is [Iba99]

$$D^{2D} = \frac{m^*}{2\pi\hbar^2} \; .$$

For $\mu_0 H \neq 0$ electrons from an energy range $\Delta E = \hbar\omega_c$ condense on one Landau level j. Hence, the number of electrons N on this level is

$$N_j = \hbar\omega_c D^{2D} = \frac{e\mu_0 H}{h} \; . \tag{2.32}$$

In a 2DES with a given total electron density n_{2D} one can calculate the number of filled Landau levels

$$\nu = \frac{n_{2D}}{N_j} = \frac{n_{2D} h}{e\mu_0 H} \; . \tag{2.33}$$

This number ν is also called filling factor. With increasing magnetic field at low temperatures N_j of all levels increases. Consequently, for a fixed n_{2D} the occupancy of the highest Landau level decreases because the lower levels are filled. Once the highest Landau level is completely empty, the Fermi energy jumps to the next lower level. In this case the ratio of n_{2D} and H yields integer values for equation 2.33.

In the following we discuss the consequences of such a quantization on transport measurements.

The quantum Hall effect and the Shubnikov–de Haas effect

The model presented in the following does not reflect the latest microscopic understanding of the quantum Hall effect but most aspects are covered by this descriptive picture. A microscopic model will be provided in the last part of this subsection. The QHE is reviewed in detail in an article by H. L. Stormer et al. in [Sto83].

In a conductive material, which is homogeneous in x and y direction but confined in z direction (2DES) electric transport is described by Ohm's law

$$\boldsymbol{J} = \boldsymbol{\sigma}\varepsilon = \begin{pmatrix} \sigma_{xx} & \sigma_{xy} \\ -\sigma_{xy} & \sigma_{xy} \end{pmatrix} \varepsilon \; .$$

If such a 2DES is exposed to a magnetic field H_z and an electric field ε_x which accelerates the electrons in the x direction, H_z deflects the motion into the y direction due to Lorentz force. This results in an orbital motion of the electrons in the x–y plane and a drift of the orbit centers in y direction. Thus the off–diagonal elements of the specific conductivity tensor $\boldsymbol{\sigma}$ are non–zero. The resistivity can be expressed as $\boldsymbol{\rho} = 1/\boldsymbol{\sigma}$ and ρ_{xy} is equal to the Hall resistance R_H in a 2DES.

Classically, the Hall voltage U_H in a 2DES is derived from the equilibrium of Lorentz force and Coulomb repulsion. It is

$$U_H = \frac{\mu_0 H_z}{n_{2D} e} I_x \; ,$$

where I_x is the current in x direction. As previously shown, quantum mechanics is needed to describe a 2DES in a magnetic field.

If Landau quantization is included, equations 2.32 and 2.33 are used to express n_{2D}. We obtain

$$U_H = \frac{h}{\nu e^2} I_x = R_H I_x \ . \tag{2.34}$$

In equation 2.34 we find a quantization of the Hall resistance due to the integer filling factors of the Landau levels. The quantization steps resulting from this rather simple picture were confirmed by R. B. Laughlin [Lau81]. He deduced the same magnitude of the quantization in a more general way from gauge invariances. Thus he verified the quantized values ab initio, independent of geometrical details and impurity effects in the experiment.

In the simple picture described above the signatures found in experiments can not be fully explained. For example in a transport experiment with increasing n_{2D} and fixed H the resistivities ρ_{xx} and ρ_{xy} would only take finite values at integer filling factors. Otherwise there are no energy states at the Fermi energy and transport will be suppressed. But real measurements behave differently: extended ranges of almost zero ρ_{xx} are measured around integer filling factors and ρ_{xy} increases in discrete steps of $\Delta\rho_{xy} = h/(\nu e^2)$ [Kli80][Kli93]. This prominent signature is shown in figure 2.9 and is called quantum Hall effect (QHE).

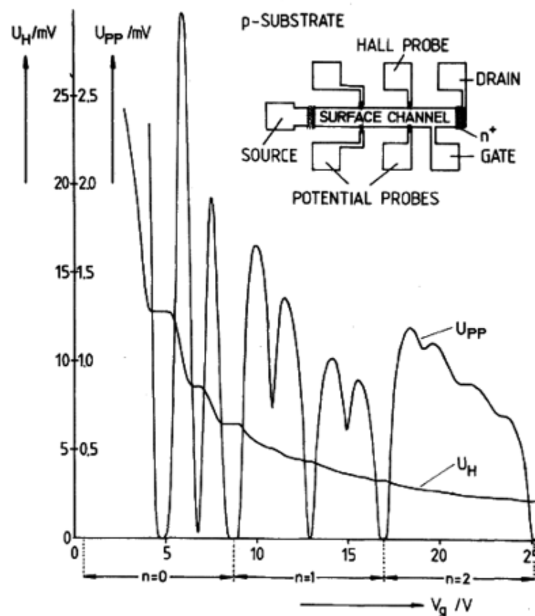

Figure 2.9: Hall voltage (U_H) and longitudinal voltage (U_{PP}) measured on a MOSFET device as a function of the gate voltage. The Hall voltage curve exhibits the quantum Hall effect with its typical plateaus. The figure is taken from a publication of K. von Klitzing et. al. [Kli80].

In order to improve the latter simple picture, impurities within the 2DES have to be included. They provide localization centers for the electrons leading to localized energy states between the Landau levels. Further, boundary induced edge states in finite 2DES occur on both sides of the originally delta shaped Landau levels [Sch84]. They are predicted to be independent of disorder. This means that also the energy space

between the Landau levels can be populated. But as these states between two Landau levels are *localized* states, they do not contribute to the electric current. Consequently, transport properties of the system remain constant as long as the Fermi energy E_F resides in this regime. The current is carried entirely dissipationless by a few spatially extended, delocalized edge states with energies near the center of each Landau level. This explains the extended plateaus in ρ_{xy} and $\rho_{xx} = 0$, respectively in this regime. If the Fermi energy matches a broadened Landau level, electron scattering is enabled. Then, ρ_{xy} increases and ρ_{xx} takes a finite value.

As already denoted, a further consequence of Landau quantization is zero conductivity σ_{xx} whenever the Fermi energy E_F resides between two Landau levels. A handwaving explanation is given in [Kli93]. K. von Klitzing argues that under these conditions the electrons are moving like free particles exclusively perpendicular to the electric field. And in this state no unbound energy levels are available at E_F. Thus, no diffusion in the x direction is possible. It follows that $\sigma_{xx} = 0$. The first observation of this phenomenon was reported by L. Shubnikov and W. J. de Haas in 1930 [Shu30][3]. They observed an oscillation of the MR in a Bi crystal, but a theoretical interpretation was not given. After its discoverers the effect is called the Shubnikov–de Haas effect.

In a magnetotransport experiment one can determine the 2DES carrier density n_{2D} from equations 2.32 and 2.33

$$n_{2D} = \nu \frac{e}{h} \mu_0 H_\nu \tag{2.35}$$

by counting the filling factor and measuring the magnetic field $\mu_0 H_\nu$ at integer ν. This condition is fulfilled on the plateaus of ρ_{xy} and in the minima of σ_{xx}.

From the definition of the specific conductivity $\sigma_{xx} = e n_{2D} \mu$ one can determine the mobility μ of the 2DES. With $\sigma_{xx} = 1/\rho_{xx}$ and $\rho_{xx} = R_{xx} W/L$ (W is the width and L is the length of the measured active area) in an extended 2DES we obtain

$$\mu = \frac{1}{e n_{2D} R_{xx}(H=0) \frac{W}{L}} \ . \tag{2.36}$$

It should be mentioned that each of the Landau levels is treated as spin degenerated so far. In the presence of the high magnetic fields used in experiments to resolve the QHE this degeneracy is lifted by Zeeman splitting.

Although the QHE is used as a quantum resistance standard and as a method for determining the fine structure constant [Sto83], a microscopic picture that describes all experimentally discovered features of the QHE is still not available. In a review article K. von Klitzing et al. discuss latest developments concerning the QHE [Kli05][4]. According to this article the most promising theory describes the QHE using compressible and incompressible areas within the sample in the presence of high magnetic fields. Dissipationless current transport occurs in the incompressible areas. This picture was developed by D. B. Chklovskii and B. I. Shklovskii et al. [Chk92]. The areas of different compressibility arise from the quantized density of states (DOS) at high H. The quantized DOS is also responsible for a stepwise increase of electron density from the edge of a sample towards the middle. The distribution of these steps depends on H and n_{2D}. Due to the difference in conductivity the distribution of compressible and incompressible areas can be mapped as a potential landscape with an atomic force microscope [Ahl01]. Such data is shown in figure 2.10. Close to integer filling factors on

[3]Article in German language.
[4]Article in German language.

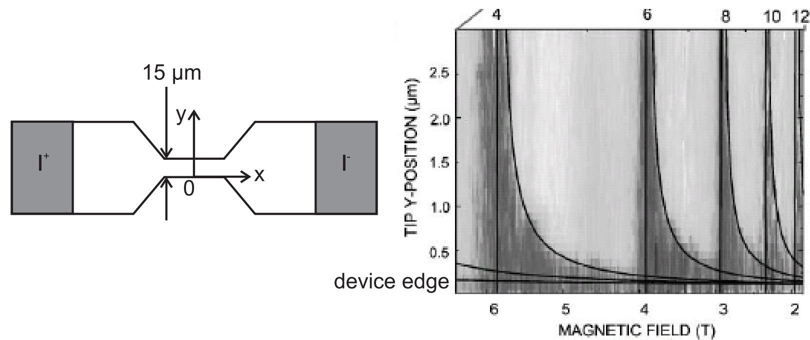

Figure 2.10: The grayscale plot (right) shows the Hall potential profile of a Hall bar (left) in y direction at $x = 0$ for different magnetic fields (in z direction). Dark (incompressible) areas indicate low potential, bright (compressible) areas indicate high potential. Integer filling factors are reached at the positions of the vertical lines and labeled at the top axis. The graph is taken from [Ahl01].

the Hall plateaus the 2DES is predominantly incompressible (dark areas) (with some imbedded compressible islands). But with decreasing magnetic field it becomes compressible (bright areas), whereas the incompressible region is shifted outwards to the edges. An incompressible area separating the two sides of the sample is always present in the plateau regions in figure 2.9. Charge transport within incompressible regions is dissipationless, thus the Hall current flows without scattering, building up the Hall voltage. The compressible areas are field free because charge redistribution shields the Hall field. If H or n_{2D} is changed within the limits of a Hall plateau, U_H remains constant because the distribution of compressible and incompressible areas changes and adjusts the voltage drop.

Further, dissipationless transport is also given in x direction for integer ν. Thus $R_{xx} = 0$. Far from integer filling factors the 2DES is entirely compressible. In this regime transport in x direction is entirely dissipative and scattering processes occur. As a consequence R_{xx} is nonzero and the Hall voltage follows equation 2.34 until the next plateau region is reached.

2.3.4 Magnetoresistance effects in hybrid structures

Following the idea of adjusting the MR behavior with conductivity inhomogeneities leads to hybrid structures consisting of NM, FM and SC materials including 2DES heterostructures. In this subsection two important MR effects in hybrid structures are presented.

The extraordinary magnetoresistance effect

The EMR effect is based on a Lorentz force induced current redistribution in a SC/NM hybrid structure.

S. A. Solin et al. fabricated samples based on van–der–Pauw discs [vdP58] with an Au disc placed in the middle of the structure [Sol00]. The area of the flat devices is in the x–y plane. The metal acts as a short for a current that is passed through the device in the plane. Without external magnetic field H the vector of the current density $\boldsymbol{j}$

points in the x–y plane and perpendicular to the Au equipotential surface. With H_z applied perpendicular to the device, $\boldsymbol{j}$ is deflected by Lorentz force by the so–called Hall angle θ. For high H_z, θ reaches 90°. In this case $\boldsymbol{j}$ points parallel to the surface of the Au disc. This means the current flows around the metallic short and entirely within the SC with a higher resistivity. The relative change in the device resistance, measured in four point geometry $R(\mu_0 H = 1\ \mathrm{T}) - R(\mu_0 H = 0)/R(\mu_0 H = 0)$ was a factor of 1000 at room temperature. T. Zhou et al. worked on linear EMR structures [Zho01]. They replaced the Au core in the SC disc by a thick metallic sheet on the edge of a square shaped SC. Their published data is shown in figure 2.11. In the asymmetric configuration (a)

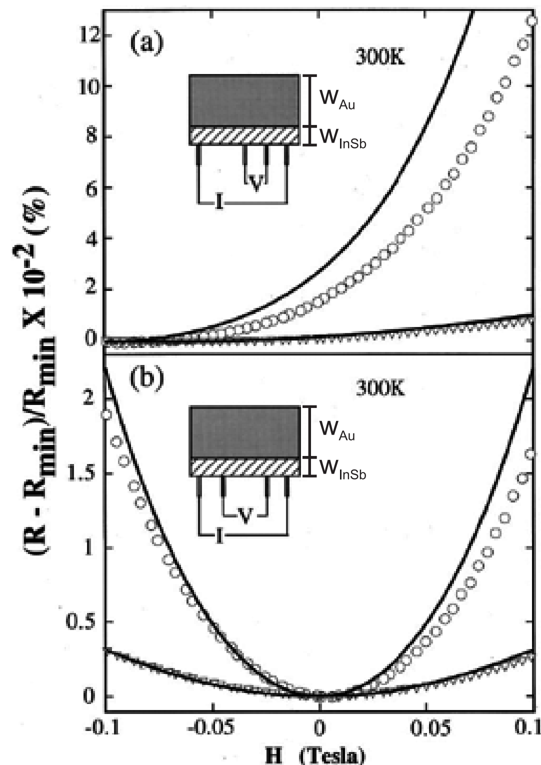

Figure 2.11: Original EMR measurements of Zhou et al. on a linear sample [Zho01]. The insets depict a scheme of the Au/InSb hybrid system with the probes along the semiconductor bar. In (a) the voltage probes were in the asymmetric, in (b) in the symmetric configuration. Solid lines show the calculation, the symbols represent experimental data. The width ratio w_{InSb}/w_{Al} for the circles is 0.1 mm/0.9 mm and for the triangles 0.3 mm/0.9 mm. The measurements have been performed at room temperature.

the MR exhibits an offset magnetic field, which is called the self–biasing field. In (b) a parabola–shaped is observed for a symmetric configuration. The different signals for different ratios w_{InSb}/w_{Au} in both panels indicate a strong dependence of the EMR signal on the device geometry.

At the same time Möller et al. reached a factor of 1150 using CEO techniques [Möl02] at $T = 4.2$ K. Detailed experiments on such EMR devices and investigations on the influence of the device geometry can be found in the Ph.D. thesis of O. Kronenwerth

[Kro04b][5] and in [Hol03a][Hol03b].

The giant magnetoresistance effect

To explain the GMR effect we consider the spin momentum $\boldsymbol{S}$ of electrons. The GMR effect can be observed in FM/NM/FM devices as shown in figure 2.12(a) where a spin polarized current flows to a FM drain contact. If the magnetization $\boldsymbol{M}$ of this drain contact is parallel (antiparallel) to the spin polarization of the current, the device resistance and the voltage V will be low (high). Figure 2.12(b) shows typical experimental data of such structures. The switching fields of the FM layers are indicated by the numbers (1) and (2) for the down–sweep of the magnetic field, and by (2) and (3) for the up–sweep. This effect was discovered independently by the groups of A. Fert

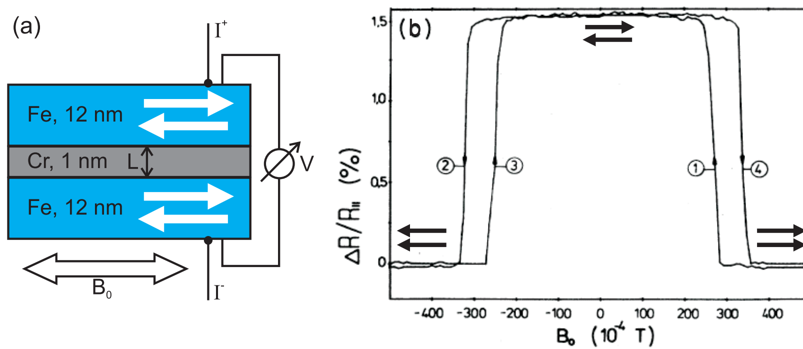

Figure 2.12: (a) Schematic picture of a GMR device, here a Fe/Cr/Fe hybridstructure. (b) Typical relative magnetoresistance curves measured at a device like sketched in (a).

[Bai89] and P. Grünberg [Bin89] in 1988 in Fe/Cr/Fe devices.

The spin polarization of a current within a FM is described in section 2.1.2. In a biased device the polarized electrons enter the NM of thickness L. Here they preserve their spin polarization if spin scattering processes can be neglected. At the interface to the second FM a spin–dependent scattering occurs. In [Bas90] the experimental data found by P. Grünberg et al. are explained by assuming different interface scattering rates for spins aligned parallel or antiparallel to $\boldsymbol{M}$. The FM provides less energy states for electrons with antiparallel spin orientation. Thus electrons with antiparallel spin must scatter including a spin flip to enter the FM.

Device designs following this principle are called spin valves. They are used in nowadays read heads in hard drives and in a wide range of sensoric applications [Gru07].

If the NM in the above structure is replaced by a 2DES the diffusive and the ballistic transport regime can be realized depending on the channel length L. Long L have two consequences. First, the device is in the diffusive regime and the spin scattering mechanisms explained in subsection 2.2.3 are effective. Second, in the framework of diffusive transport a general obstacle for spin polarized transport is predicted due to the conductivity mismatch between the SC and the FM [Sch00].
If L is shorter than the electrons' mean free path the ballistic picture is valid. In this regime spin scattering processes are minimized and the conductivity mismatch is not relevant. In [Gru01a] and [Hu01a] a finite GMR effect was predicted for ballistic

[5] Thesis in German language

FM/2DES/FM devices. They point out that in such devices spin filtering at the interfaces plays an important role (see section 2.2.5). In an experiment by C.–M. Hu et al. the GMR effect was investigated as a function of L [Hu01b]. They report a spin polarization of up to 4.5 % for the current driven through a FM/2DES/FM device in the ballistic regime with $L < 2\ \mu$m.

2.4 Microwave induced photovoltage

The following model explains the occurrence of a dc voltage drop V across a FM film in an external magnetic field $\mu_0 \boldsymbol{H}$ under rf irradiation. We first note that in contrast to the model used in [Cos06a], no NM contacts or spin transfer across FM/NM interfaces are necessary here. The rectification effect of a microwave acting upon a FM film was already found experimentally in 1959 [Tan59]. Latest experiments on this topic were performed in the group of C.–M. Hu [Gui07][Mec07]. It is based on both, the AMR effect, which is described in subsection 2.3.1, and Ohm's law. An review of this model is presented in the Ph.D. thesis of N. Mecking [Mec08]. We focus on two effects that occur, if a FM film with magnetization $\boldsymbol{M}$ is exposed to a rf electromagnetic field with frequency ω: (i.) a rf current density $\boldsymbol{j}_{rf}(t) = \boldsymbol{j}_1 \cos(\omega t)$ is induced in the FM. Its direction is parallel to the electric component of the rf field, following the argumentation in [Mec07]. The angle between $\boldsymbol{j}_{rf}$ and $\boldsymbol{M}$ is Φ. (ii.) If the magnetic component of the rf field $\boldsymbol{h}_{rf}$ exerts a torque on $\boldsymbol{M}$, i.e. $\boldsymbol{M} \times \boldsymbol{h}_{rf} \neq 0$, $\boldsymbol{M}$ precesses around its equilibrium direction $\boldsymbol{M}_0$. Important vectors and angles of this subsection are sketched in figure 2.13.

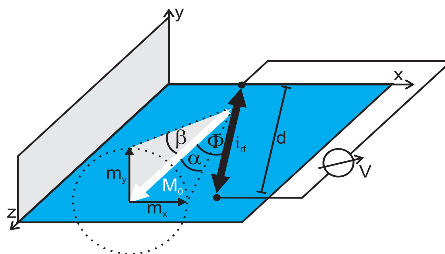

Figure 2.13: Schematic picture of the mechanism that induces a photovoltage. The orientations of the vectors described in the text are depicted.

As a consequence of the precession, the angle Φ oscillates. Plugging the oscillating $\boldsymbol{j}_{rf}(t)$ and $\Phi(t)$ into equation 2.28 yields nonzero values for the electric field ε in time average. In [Mec07] these dc components are calculated. The angle $\Phi\,(t)$ is split into a static and a time dependent component, Φ_0 and $\Phi_1\,(t)$. Further the angle components in the x–z plane and in the y–z plane are considered separately and defined by $\alpha\,(t) = \alpha_0 + \alpha_1\,(t)$ and $\beta\,(t) = \beta_0 + \beta_1\,(t)$. For the maximum deflection angles of $\boldsymbol{M}$ we find $\sin \alpha_1^{\max} = m_x/M_0 \approx \alpha_1^{\max}$ and $\sin \beta_1^{\max} = m_x/M_0 \approx \beta_1^{\max}$, with m_x and m_y being the precession amplitudes in x and y direction. For small amplitudes and under the assumption of elliptical precession the following relations are valid

$$\begin{aligned} \alpha\,(t) &\approx \alpha_0 + \frac{m_x}{M_0} \cos\left(\omega t - \theta_m\right) \\ \beta\,(t) &\approx \beta_0 - \frac{m_y}{M_0} \sin\left(\omega t - \theta_m\right) \ . \end{aligned} \tag{2.37}$$

θ_m is the phase shift between the precession and the exciting rf field. Then the relation

$$\cos\Phi\left(\alpha\left(t\right),\beta\left(t\right)\right)=\cos\alpha\left(t\right)\cos\beta\left(t\right) \tag{2.38}$$

applies. The AMR effect is a function of $\cos^2\Phi$ according to equation 2.28. In [Mec07] an in–plane magnetization (i.e. $\beta_0 = 0$) is discussed with and $\alpha_0 = \Phi_0$. In order to evaluate the time dependent terms, they use a second order approximation of $\cos^2\Phi\left(t\right)$ using equations 2.37 and find

$$\begin{aligned}\cos^2\Phi\left(\alpha\left(t\right),\beta\left(t\right)\right) &\approx \cos^2\Phi_0-\frac{m_x}{M_0}\sin 2\Phi_0\cos\left(\omega t-\theta_m\right)\\ &-\left(\frac{m_x}{M_0}\right)^2\cos 2\Phi_0\cos\left(\omega t-\theta_m\right)\\ &-\left(\frac{m_y}{M_0}\right)^2\cos^2\Phi_0\sin^2\left(\omega t-\theta_m\right)\ .\end{aligned} \tag{2.39}$$

This result and $\boldsymbol{j}_{rf}\left(t\right)$ is plugged into equation 2.28 reading

$$\varepsilon_j=\left(\rho_0+\Delta\rho\cos^2\Phi\left(t\right)\right)\left(j_1\cos\left(\omega t\right)\right)\ .$$

The time average of this function is

$$\left\langle\varepsilon_j\right\rangle_t=-j_1\Delta\rho\frac{m_x}{M_0}\sin 2\Phi_0\frac{\cos(\theta_m)}{2}\ , \tag{2.40}$$

representing the dc component of the electric field in $\boldsymbol{j}_{rf}$ direction. Multiplication of $\left\langle\varepsilon_j\right\rangle_t$ with the distance d between two voltage probes along $\boldsymbol{j}_{rf}$ results in the rf induced dc photovoltage.

2.5 The spin field–effect transistor

Lateral FM/2DES/FM devices are discussed to operate as spin field–effect transistors (spin FETs). In such transistors not the charge of the electron but its spin momentum is intended to switch between the "on" and "off" state of the transistor. This is why the optimization of spin transport properties and spin manipulation in the device plays a crucial role.

As shown in figure 2.14(a) a spin FET based on the idea of S. Datta and B. Das [Dat90] consists of FM source and drain contacts. These are separated by a 2DES with the length L. A gate electrode is used to induce an electric field ε in the 2DES channel.

Electrons become spin polarized when they pass through FM1 (see section 2.1.2). So one important issue is a high degree of spin polarization in the source contact.
This spin polarization can be transferred into the 2DES if an efficient spin injection is provided across the FM/2DES interface. Depending on the interface quality and the choice of materials the interface can act as a spin diffuser or spin filter (see section 2.2.5). To avoid unwanted scattering processes at the interface it is favorable to provide a clean and epitaxial FM/2DES interface.
The magnitude of the expected MR effect scales with the degree of spin polarization reaching the drain contact. Thus the 2DES channel must be designed to minimize depolarization effects.

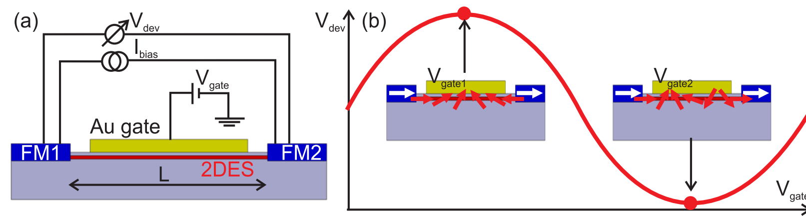

Figure 2.14: a) Schematics of a spin FET based on S. Datta and B. Das in reference [Dat90]. b) A variation of the gate voltage V_g changes the spin–orbit interaction and therewith the precession angle θ at FM2. The voltage drop across the device is plotted as a function of V_g. At the extrema devices with $\theta = 0°$ and $\theta = 180°$ are depicted.

The working principle of this device was proposed in analogy to the electro–optic modulator [Dat90]. The spin polarized current I_{bias} between the source and the drain contact is modulated by changing the spin–orbit coupling of the 2DES channel with ε. This field is proportional to the gate voltage V_{gate}. The influence of ε on the spin–orbit coupling is described in subsection 2.2.2.

In subsection 2.2.1 we showed that the spin of an electron in a 2DES precesses under certain conditions. The precession frequency is governed by the spin–orbit coupling parameter α. With equation 2.8 one can calculate the angle θ by which the spin has precessed after travelling through the 2DES channel with length L. In figure 2.14(b) the expected voltage drop across the device V_{dev} is shown as a function of the gate voltage. The two extreme cases $\theta = 180°$ and $\theta = 0°$ are pointed out. The two sketches of samples in the graph illustrate the evolution of the spins in the 2DES at these points. In analogy to the GMR effect that is explained in section 2.3.4, the different V_{dev} occur due to different interface scattering conditions the 2DES/FM2 interface. As θ changes continuously from 0° to 360° with increasing V_{gate} the voltage drop describes a sine function.

The realization of a Si based spin FET was reported recently [Hua07]. But the working principle is based on the variation of the electrons' transit time through the SC channel rather than a variation of the spin–orbit coupling [App07]. No experiment was presented so far that reproduces the curve as indicated in figure 2.14(b).

A transistor with the same FM/2DES/FM device structure but with a different working principle was proposed by J. Schliemann et al. [Sch03]. It is operated by the variation of α_{SIA} relative to α_{BIA} by an electric field. This transistor is in its "off state" if $\alpha_{SIA} \neq \alpha_{BIA}$. If α_{SIA} is tuned such that $\alpha_{SIA} = \alpha_{BIA}$ the transistor is in the "on state". For $\alpha_{SIA} = \alpha_{BIA}$ the spin states in the 2DES are independent of the wave vector $\boldsymbol{k}$. Under this condition no spin scattering processes occur as shown in section 2.2.3 and the device resistance is low. For $\alpha_{SIA} \neq \alpha_{BIA}$ the spin states are $\boldsymbol{k}$ dependent and thus get randomized if the system is in the diffusive regime. This results in a higher device resistance.

Chapter 3

Preparation and measurement techniques

3.1 Spin FET devices

To prepare a prototype of a spin FET as described in section 2.5 we developed a novel lateral sample design based on FM contacts on a SC heterostructure which incorporates an InAs 2DES. A fundamental advantage of using SC for spin transport devices is that longer spin relaxation lengths can be realized compared with metals [vW07]. The following sections provide details to our QW heterostructure and explain the CEO method and the subsequent structuring of contacts on the cleaved edge. The last sections in this chapter describe the experimental setup and measurement techniques.

3.1.1 Properties of the InAs heterostructure

As semiconducting channel we chose a strained InAs 2DES incorporated in a heterostructure. These high electron mobility systems are designed and grown in the group of W. Hansen[1] using molecular beam epitaxy. A transmission electron microscope picture and a schematic picture of the layer structure is shown in figure 3.1(a). Details to the growth conditions can be found in [Ric00], [Men01] and [Hey02]. As the doping layer is grown prior to the QW and due to the high electron mobility, the structure is called inverted high electron mobility transistor (HEMT). The band structure calculated with the program *1D Poisson* by G. Snider [Sni07] is displayed in figure 3.1(b). The band structure is asymmetric. The modulation doping produces an inherent electric field in growth direction. This gives rise to structure inversion asymmetry (SIA). As a narrow–gap SC bulk InAs exhibits a band gap of only 0.42 eV.

Typical values for the electron density in the 2DES n_{2D} and the electron mobility μ are $n_{2D} = 2.85 \times 10^{11}$ cm^{-2} to 5.7×10^{11} cm^{-2} and $\mu = 62\,100$ cm^2/Vs to $149\,000$ cm^2/Vs. These values are taken from [Möl03a] and measured in van der Pauw [vdP58] geometry and the material properties were tuned by means of the persistent photo effect. Further in [Löh03] $n_{2D} = 6.3 \times 10^{11}$ cm^{-2} and $\mu = 160\,000$ cm^2/Vs are measured using a Hall bar geometry. The samples of both cited experiments are InAs QW structures with the same layer sequence as the heterostructure presented here.

The use of InAs for our spin FET devices implies two advantages compared with other SC materials. First, it forms no Schottky barrier at the interface to a metal

[1]Institut für Angewandte Physik, Universität Hamburg

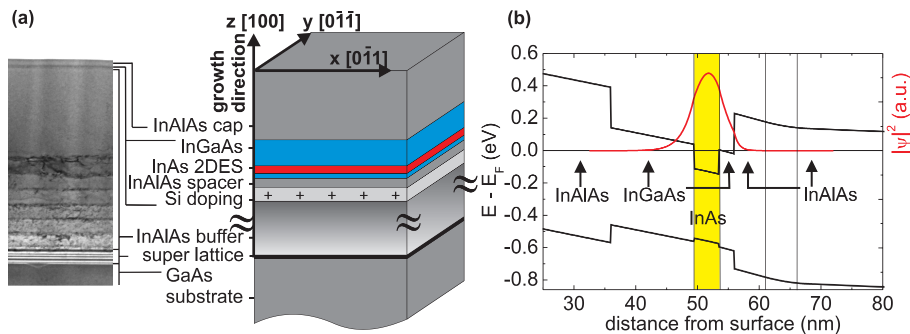

Figure 3.1: (a) TEM picture of the InAs heterostructure used in our experiments taken from [Men01] and schematic picture of the layer sequence. The InAs 2DES channel is 50 nm below the surface. (b) The edges of the conduction and valence band are shown as a function of the distance to the sample's surface. The shaded area is the section of the InAs channel where the probability density for electrons has its maximum (right axis).

contact [Kro04a]. The absence of a barrier is a prerequisite for highly transmissive interfaces [Ric00]. The transport characteristic across interfaces is determined by the shape of the band structure. Close to an InAs/metal interface, the conduction band of the InAs is lowered in energy. This leads to an Ohmic interface characteristic.

A further advantage of InAs is its high spin–orbit coupling. A comparison of spin–orbit coupling constants is given in table 2.11 in subsection 2.2.2. This parameter and, in particular, its tunability is a decisive factor for a spin FET.

3.1.2 Cleaved–edge overgrowth

In this section the initial steps of the sample preparation will be explained in detail. The aim is to produce a clean and atomically flat surface. Therefore we cleave our samples in situ and instantaneously cover them with a Co layer to avoid contamination of the FM/2DES interface. The preparation is illustrated in figure 3.2.

We start with a 4×4 mm^2 square of InAs heterostructure as described in the previous section. The pieces are taken from a 2" wafer by cleaving it along its crystal axes. The coordinates x, y and z in 3.2(a) represent the crystal directions $[1\bar{1}0]$, $[\bar{1}\bar{1}0]$ and [001], respectively.

The sample is provided with a predetermined breaking line, which is a scratch with a length of 0.5 mm placed in the center of one edge and parallel to a crystal axis. In preliminary tests we found that depth, parallel orientation to the crystal axis and the quality of the scratch are crucial for the texture of the cleaved surface. This is why we designed an align fixture (figure 3.3(a)) that allows us to move the sample parallel to its x direction. We use a diamond tip to perform the scratching. The tip is mounted at the end of a movable arm with a counterweight to adjust the bearing strength of the tip on the sample. So we adjust the depth of the scratch. Best results are achieved with a bearing strength of 20 g. With this parameter we are able to produce shallow scratches with very smooth side walls. We place the predetermined breaking line in the center of a y edge as shown in figure 3.2. By choosing this side, we make sure that

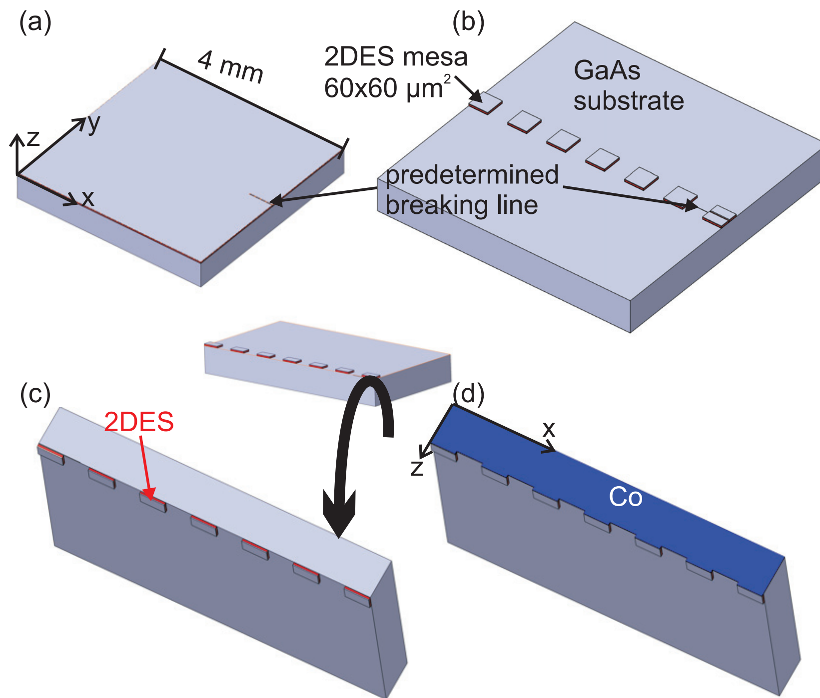

Figure 3.2: Schematic picture of the CEO process: (a) The predetermined breaking line is set with a diamond tip in x direction and along the $[1\bar{1}0]$ crystal axis. (b) After a dry etching process only quadratic mesas of 2DES are left along the predetermined breaking line. (c) The sample is cleaved in high vacuum at a pressure of about 10^{-7} mbar while the Co source is already heated. (d) A Co layer is deposited on the cleaved edge.

the spins are polarized in the x direction in our transport experiments. At the end of subsection 2.2.3 we explain, why this direction is favorable.

Figure 3.2(b) illustrates that the 2DES is structured into squares of 60×60 μm along the predetermined breaking line. By this means we define the area of possible current flow to these small squares close to the future cleaved edge. Thus we avoid long current paths that do not contribute to the spin dependent signal in our experiments. Structuring is done by standard photolithography followed by ion beam etching with Ar ions. The etching time is 30 minutes with an acceleration voltage of 400 V and a beam current of 30 mA. AFM measurements yield an etched depth of 570 nm. With a built–in secondary ion mass spectrometer we can monitor the etched material composition during the etching process. We observe a decreasing In rate following the stepwise decrease of In content in the layer compositions shown in figure 3.1(a). Although the 2DES is located only 50 nm below the surface we found that deeper etching is necessary to avoid leakage currents between neighboring mesas. Such currents might occur in the buffer layers with a high In content.

The sample with the 2DES mesa structure is fixed in a sample holder as shown in figure 3.3(b). The sample holder is designed to position the sample in y direction so that the predetermined breaking line sits right below the clamp. Furthermore the sample's x direction is aligned parallel to the edges of the clamp. This is crucial for the surface quality of the cleaved edge. After the alignment the sample is fixed in the sample holder by closing the clamp. Then we put the sample holder into a high vacuum

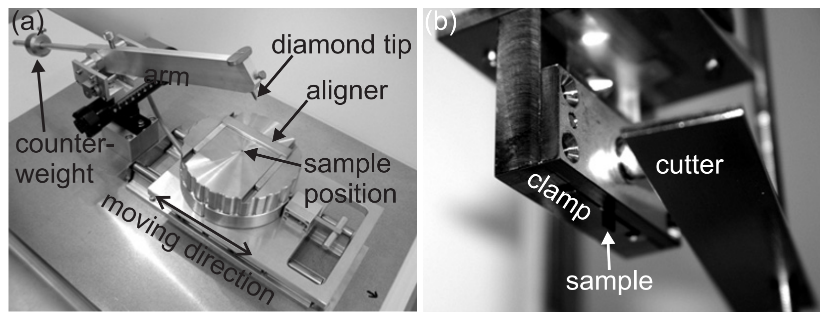

Figure 3.3: (a) Picture of the aligner with diamond tip that is used to set the predetermined breaking line for cleaving the sample. (b) Picture of the sample holder used for in situ cleaving.

chamber. At a base pressure well below 1×10^{-6} mbar the thermal evaporation process is started. The Co evaporation rate is set to 0.5 nm/s and the evaporation pressure is in the range of 10^{-6} mbar. For these parameters we estimate to deposit one monolayer per second, assuming a sticking coefficient of 1 [Hey08]. Under these conditions the sample is cleaved, so we make sure that the cleaved edge is covered instantaneously with the evaporating Co. At a layer thickness of 20 nm the deposition is stopped.

As reference samples we also prepared hybrid structures with different thicknesses of the Co layers and with Fe as FM.

3.1.3 Photolithography on the cleaved edge

To prepare microstructures on a cleaved edge using photolithography we modified some of the conventionally used techniques. The area of the cleaved edge covered with Co has a length of 4 mm and a width of 0.5 mm. The aim in this preparation step is to pattern four leads with pads at the ends which will be used for wire bonding to contact the source and drain contacts. A microscopic picture showing this pattern on the cleaved edge of a sample is shown in figure 3.4(right).

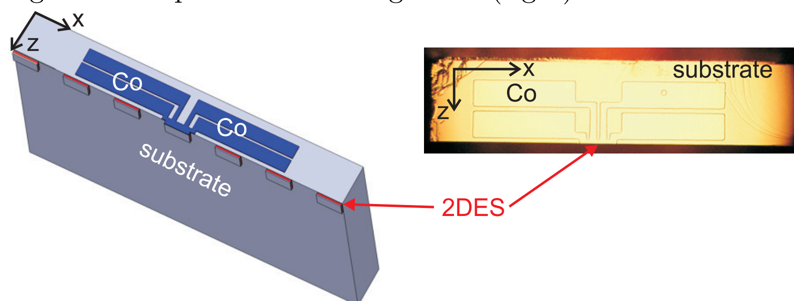

Figure 3.4: Left: The bond pad pattern on the cleaved edge after the photolithography and ion beam etching process. Right: Optical micrograph of the cleaved edge with bond pads and leads which were etched using an ion beam.

The sample must be in an upright position to deposit the photoresist. We use the photoresist *Microposit S1813* manufactured by *Rohm & Haas*. Due to the non–planar geometry, the cleaved edge can not be spin coated, as the sample would tip on the

rotating chuck. Another difference to planar structuring is that the surface tension of the resist dominates the layer thickness due to the small dimensions in z direction. This results in an extremely inhomogeneous distribution of the photoresist across the cleaved edge. In the middle the resist layer is very thick, whereas the edges were even not covered at all.

We solved these problems by diluting the photoresist with *Microposit EC Solvent* at a ratio 1:4. This yields two advantages: First, the diluted resist shows a reduced surface tension so, if deposited directly from a droplet at the end of a cannula, it covers the whole surface including the edge regions. Second, the *EC Solvent* evaporates during the bakeout process of 45 minutes at 90° C. So the thickness of the remaining photoresist layer is comparable with conventionally spun–on layers on planar structures after the bakeout. The sample is placed upright under the chromium mask of a mask aligner manufactured by *Karl Süss*. With an exposure time of 6 s at an intensity of 12 mW/cm^2, measured at a wavelength of 365 nm, we obtain a well defined resist structure on the cleaved edge.

The sample with the photoresist mask is exposed to a directed Ar ion beam. The areas of the Co film that are not covered with photoresist are removed. To perform this dry etching process, the sample is built into a vacuum chamber and tilted by an angle of 45° in $-z$ direction so that the 2DES is protected from being exposed to the ion beam. Etching is performed at an acceleration voltage of 400 V and a beam current density of 1.5 mA/cm^{-2} for 15 minutes.

3.1.4 Shaping source and drain contacts with a focused ion beam

In this preparation step the source and drain contacts are defined. We start from the rectangular Co area between the bond pads that was etched by the Ar ion beam (see section 3.1.3). The nanolithography is performed using a focused ion beam (FIB). In particular we use Ga ions to etch the spin injection and spin detection contacts with a resolution of 50 nm[2]. These structures are shown in figure 3.5. They are typically 3×12 μm and 5×12 μm in size. Contact B is wider in z direction compared with contact A. The aim is to achieve an insulation between the contacts A and B and to

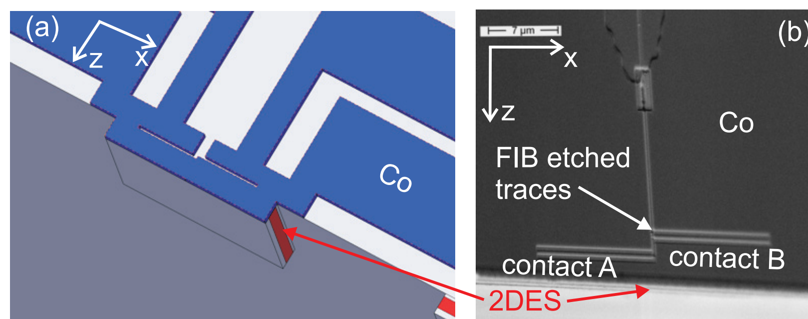

Figure 3.5: Hybrid structure after FIB etching: (a) shows a schematic view, (b) is a SEM picture. The Co contacts A and B are shaped differently in z direction introducing different magnetic shape anisotropy terms. We do not expose the 2DES to the FIB.

realize different coercive fields H_{coe} due to shape anisotropy. The latter mechanism is

[2]The FIB etching process was performed in cooperation with D. Stickler at the Universität Hamburg.

explained in subsection 2.1.1. Different H_{coe} allow us to manipulate the magnetizations M of contact A and B separately.

It is important not to expose the 2DES to the ion beam. High energetic Ga ions could be implanted in the QW structure and act as electron and spin scatterers (see section 2.2.3). This would reduce the mobility of the 2DES and reduce spin polarization. This is why we do not use FIB alone to separate the contacts completely.

3.1.5 Separation of source and drain contacts with nanoindenting

The final separation of source and drain contact is done with nanoindenting with a diamond tip of an atomic force microscope[3] (AFM) manufactured by *Veeco Instruments*. The development of this technique included experiments with Si tips and tips coated with diamond like carbon (DLC). The advantage of Si tips is a very small tip radius of 10 nm but the material is not hard enough to pierce into the 20 nm thick Co layers. Tests showed that not only the hardness of the tip but also the stiffness of the supporting cantilever are relevant. We tried DLC coated tips with a force constant of the cantilever of 42 N/m but the best results were obtained with a pure diamond tip with a force constant of 150 N/m and a tip radius of 40 nm. To measure the quality of the nanoindentation we monitored the resistance R of a test structure while performing the indentation. We found that during indentation the resistance increased by orders of magnitude resulting in an insulation with $R > 40$ MΩ.

The use of this technique for our spin FET devices meets the demands that are discussed in sections 2.2.5, 2.5 and 3.1.4. The tip radius of 40 nm allows us to indent triangularly shaped trenches below 100 nm in width and up to 50 nm deep. Thus the Co film can be electrically separated into source and drain contacts with an extremely small spacing. In figure 3.6 the resulting structure is depicted. The length of the semiconducting channel between the contacts is below 100 nm. The white arrows in (b) and (d) indicate the magnetizations $\boldsymbol{M}_A$ ($\boldsymbol{M}_B$) of contact A (B). They can be adjusted to be parallel or antiparallel.

This method needs no chemical or ion based etching processes so we can assume that the 2DES channel is unharmed. We performed magnetotransport measurements on Hall bar structured reference samples taken from the same wafer. We could show that the carrier density and the mobility of the nanoindented devices is not reduced compared with these reference samples.

3.1.6 Preparation of the gate electrode

In this subsection we describe the preparation of a gate electrode on top of the cleaved edge. The process is schematically illustrated in figure 3.7. First an insulating layer of SiO_2 is deposited in a plasma enhanced chemical vapor deposition (PECVD). The sample is placed upright in a PECVD chamber. It is evacuated and heated to a temperature of 150° C. This temperature differs from the standard parameter of 300° C but we have to consider that high temperatures could damage the QW structure due to diffusion of In atoms into the neighboring layers. 150° C was found to be high enough to produce insulating SiO_2 layers but low enough to avoid the diffusion effects. During the deposition a constant flow of $SiCl_4$ and O_2 and a rf power of 20 W was adjusted. The nominal thickness of the insulating layer is 300 nm. AFM measurements yielded

[3] Nanoindenting was performed in cooperation with K. Rachor at the Universität Hamburg.

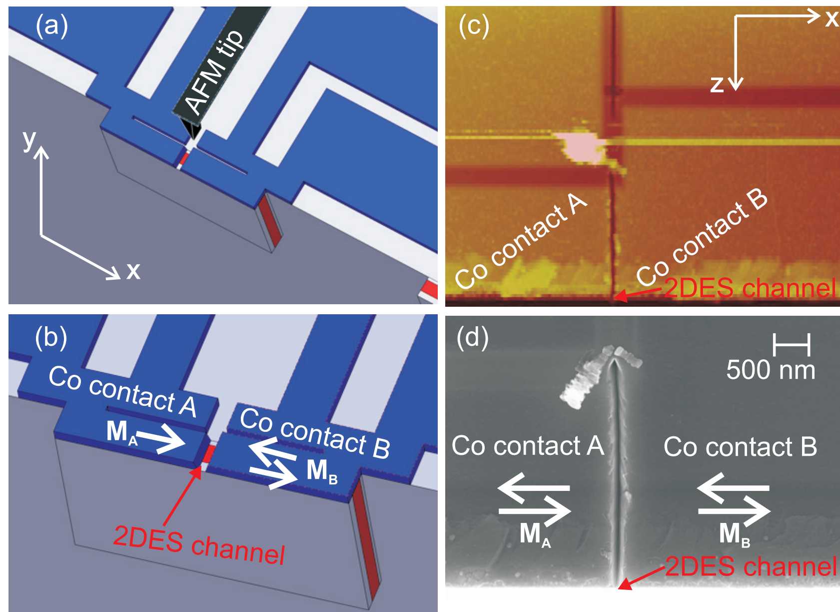

Figure 3.6: (a) and (b): Schematic picture of the nanoindenting process with an AFM tip. The prestructured Co film is separated in source and drain contacts connected by a 2DES channel. (c): AFM picture of the cleaved edge after nanoindenting. (d): SEM picture after nanoindention. The length of the 2DES channel is below 100 nm. At the upper end of the indentation the removed material is seen. The white arrows in (b) and (d) represent magnetizations $\boldsymbol{M}$ of the FM contacts.

SiO_2 thicknesses on the cleaved edge of about 500 nm. It is known that the strength of the RF field in the PECVD chamber has maxima at the edges of the sample. As our sample is in an upright position, we assume a higher plasma density resulting in a higher deposition rate on the cleaved edge. Figure 3.7(a) shows this preparation state schematically and a SEM picture of a cross section. We find that the SiO_2 encloses the cleaved edge completely providing a good insulation across the whole surface. On top of this insulating layer we deposit the 20 nm thick Au gate electrode in a thermal evaporation process (see figure 3.7(b)).
We are able to apply voltages higher than 500 V between the Au electrode and the Co contacts without exceeding a leakage current of a micro ampere. This results in a breakthrough voltage of over 10 MV/cm what is comparable to nowadays industrially produced insulating layers [Int07].
In the following step the contacts have to be connected. This is why the gate electrode and the oxide have to be removed partly as shown in Figure 3.7(c). We found a very easy method with no need of any chemical treatment of the sample. An adhesive tape (manufacturer: *tesa AG*) is placed on the cleaved edge, covering the area to be bared from the oxide. Then the tape is pulled abruptly in vertical direction. The Au and the SiO_2 stick to the tape, whereas the Co structure remains on the cleaved edge. We found that this technique to remove SiO_2 is not applicable to planar structures. The reason why it works with our samples might be the extremely flat surface of the cleaved edge on which the SiO_2 is deposited.

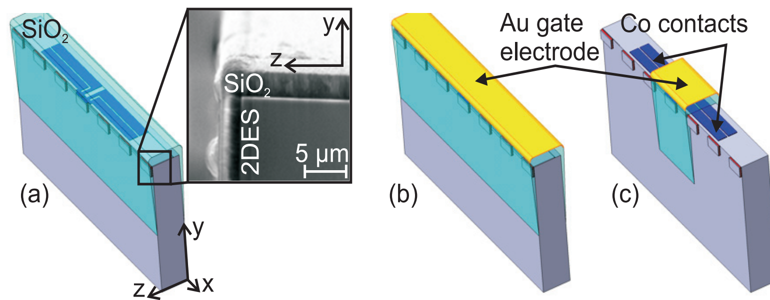

Figure 3.7: Illustration of the gate preparation process. (a) SiO_2 is deposited on the cleaved edge in a PECVD process. The SEM picture of a cross section details the SiO_2 growth around the corners. (b) The Au gate electrode is thermally evaporated on the cleaved edge. (c) We remove parts of the gate electrode and the insulating layer to uncover the Co pads. In the next step the pads are contacted using wire bonding.

3.1.7 Contacting the sample

To perform transport experiments, the sample is connected electrically to the measurement electronics. First the upright–standing sample is glued to a Cu carrier with insulating superglue. It is placed in the middle of an epoxy ring that contains several Cu contacts as shown in figure 3.8(a). The Co contacts are connected to these Cu contacts by wire bonding. We use a *F&K Delvotec 53xx* semiautomatic wedge bonder with 25 μm thick Al wire. The gate electrode can not be connected by wire bonding because the SiO_2 layer would be destroyed by the ultrasonic pulse of the wedge bonder. Thus we use conductive silver for this contact. The Cu contacts on the epoxy ring are used to solder Cu wires leading to the measurement electronics. We use flexible wire strands with a diameter of only 0.1 mm^2 which provide enough flexibility at low temperatures to rotate the sample on the rotation stage. In figure 3.8(b) the sample is shown, mounted on the rotation stage of the sample holder with the soldered Cu wires. More details concerning the measurement setup are provided in the following section.

3.1.8 Cryogenic magnetotransport setup

The measurement setup is shown in figure 3.9. We use a cryostat filled with liquid helium. In the cryostat superconducting coils powered by a stabilized bipolar power supply (*Oxford Instruments*) generate a magnetic field $\mu_0 H$ up to 9 T at 4.2 K and 11 T at 2.2 K (reached by reducing the pressure in the cryostat). This field is homogenous to 1 part in 10^{-4} in a volume of at least 1 cm^3 at the position of the sample. The sample is mounted on the sample holder as shown in figure 3.8(b) and inserted in a stainless steel can to protect it from direct contact with the liquid helium. With this setup we reach a base temperature of 4.4 K at the position of the sample.

We designed a sample holder that allows us to tune variables like the magnetic field angle, the temperature and the illumination state of the sample. It provides 24 Cu leads to connect the sample and two shielded cables for HF applications. The sample mount is a Swedish rotator so we could rotate the sample with respect to the magnetic field around one axis. A detailed picture can be found in figure 3.8(b) in subsection 3.1.7. The rotation stage is equipped with a calibrated Hall sensor to monitor the magnetic field component perpendicular to the plane of the rotation stage via the Hall voltage. By

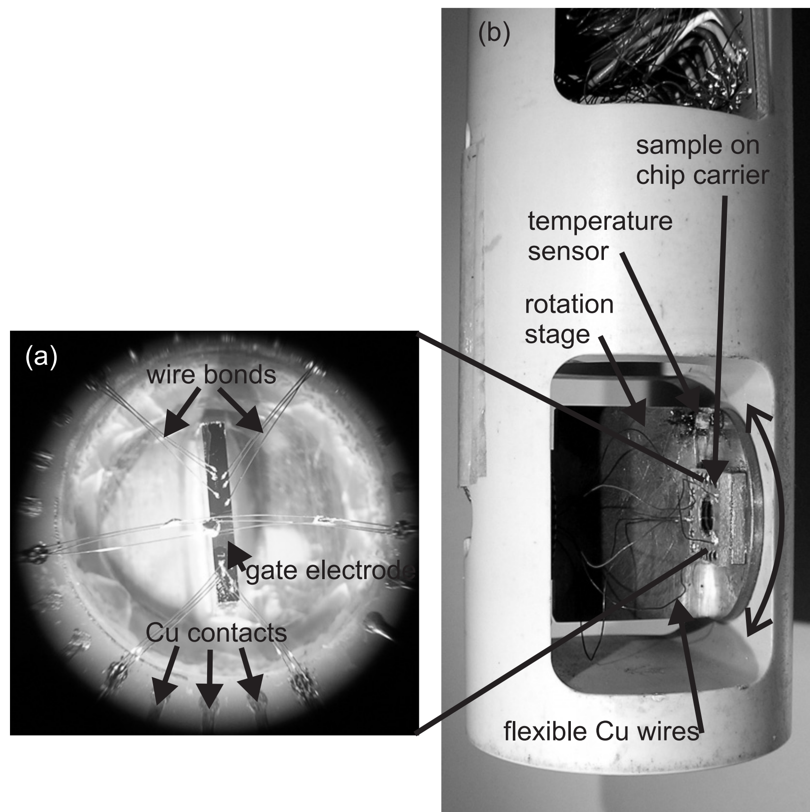

Figure 3.8: Photographs of the sample mounted on the rotation stage of the sample holder. (a) shows a top view on the cleaved edge with the electrodes connected by wire bonding. (b) illustrates the mounting position of the chip carrier on the rotation stage.

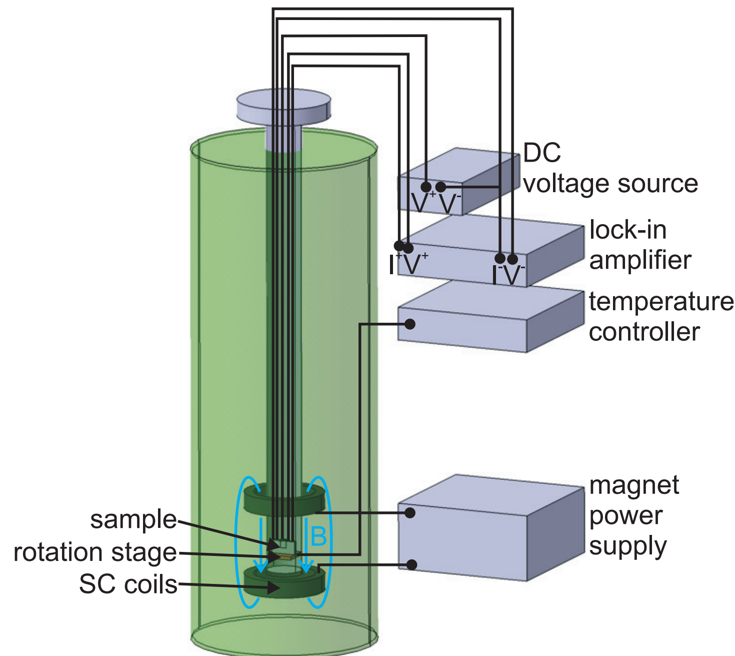

Figure 3.9: Schematic picture of the measurement setup.

this means we can calculate the tilt angle θ of the Swedish rotator. With an integrated *Cernox* temperature sensor and a 50 Ohm heating coil we adjust the temperature of the sample from base temperature up to 70 K using a *Neocera* temperature controller. The rotation stage is made of Cu to ensure good thermal contact to the chip carrier. As our chip carrier is also made of Cu we assume equal temperatures at the sample and at the sensor. All parts of the sample mount are made of non–FM materials to avoid unwanted influences of magnetic stray fields on our magnetotransport measurements.

The four terminal measurements are performed with *Stanford Research Systems SR830* lock–in amplifiers (LIA). A dc voltage source manufactured by *Yokogawa* provides gate voltages in the range of ± 110 V.

With an integrated red LED the sample can be illuminated. By this means we use the persistent photo effect to increase the carrier density in the 2DES channel.

In figure 3.10 the wiring for two different types of measurements is displayed. Figure 3.10(a) shows the four terminal setup for current modulated measurements. It is used in section 7.1. The bias current is applied from contact A to contact B. It is generated by the sine voltage of the LIA V_{LI}^{ac} connected via a series resistor of 1 MΩ. The sample resistance is in the range of 1 kΩ, so we can assume to deal with a current biased device. The voltage drop V_{dev} is measured between the contacts C and D.. The input impedance of the LIA is 50 MΩ. We use a low modulation frequency of 36 Hz. I_{bias}^{ac} depends on the experiment and is given in section 7.1. Additionally we can superimpose a variable dc current in the range of ± 50 μA by tuning V_{LI}^{dc} or fixed dc currents by using a battery with a resistor of 100 kΩ connected in series. The capacitor is inserted in the ac circuit to avoid a feedback of the dc source to the ac voltage source and vice versa. The voltage drop across the hybrid structure is measured from contact C to D using the differential input of the LIA. Gate voltages V_{gate}^{dc} are applied between the gate electrode and the drain contact B.

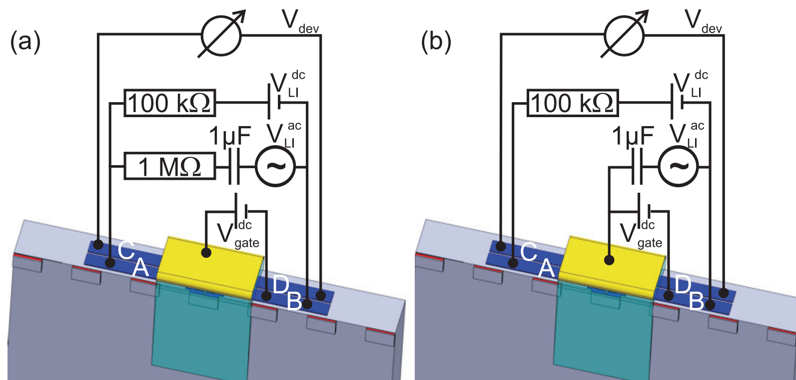

Figure 3.10: Wiring for (a) current modulated and (b) gate voltage modulated measurements.

With the setup displayed in figure 3.10(b) gate voltage modulated measurements are performed. It is used in section 7.1 Here we apply a dc bias current $I^{dc}_{bias} = 90\ \mu$A from contact A to B and measure the voltage drop at the contacts C and D. The dc gate voltage V^{dc}_{gate} is modulated typically with $V^{dc}_{gate} = 0.5$ V (rms) and 36 Hz. The electric field between the gate electrode and contact B varies the conductivity of the SC channel. The measured quantity is $\partial V_{dev}/\partial V_{gate}$. The dynamic resistance R^{dyn}_{dev} is calculated by multiplication with the dc bias current I^{dc}_{bias}

$$R^{dyn}_{dev} = \frac{\partial V_{dev}}{\partial V^{dc}_{gate}} \cdot I^{dc}_{bias}. \tag{3.1}$$

With the modulation of the gate voltage we do not alter the electronic properties of the FM contacts but, as we will see, the electron density in the 2DES. Accordingly, using lock–in technique with modulated V_{gate}, we focus on effects originating from the 2DES.

3.2 Spin battery devices

In the following we describe the preparation of the samples that are used to measure photovoltages under rf irradiation. These are 2DES/FM/NM hybrid structures. The preparations steps are illustrated in figure 3.11. We start with a 4×4 mm^2 piece of an InAs heterostructure that incorporates a 2DES. It is the same QW structure that is used for the spin FET devices. Its properties are provided in subsection 3.1.1. On this piece we prepare a macroscopic circular Al contact with a diameter of 2 mm. We use standard photolithography followed by thermal evaporation of the Al and a lift–off process. Then we deposit a 20 nm thick Co layer on the cleaved x–z surface using a CEO process. This process is described in detail in subsection 3.1.2. The Co connects the 2DES with the Al contact. The inset in figure 3.11(b) shows the 2DES channel at the cleaved edge. The distance between the 2DES and the Al contact is 50 nm. With our preparation method we realize a nanoscopic 2DES/FM/NM junction with a homogeneous geometry over a macroscopic length of 2 mm.

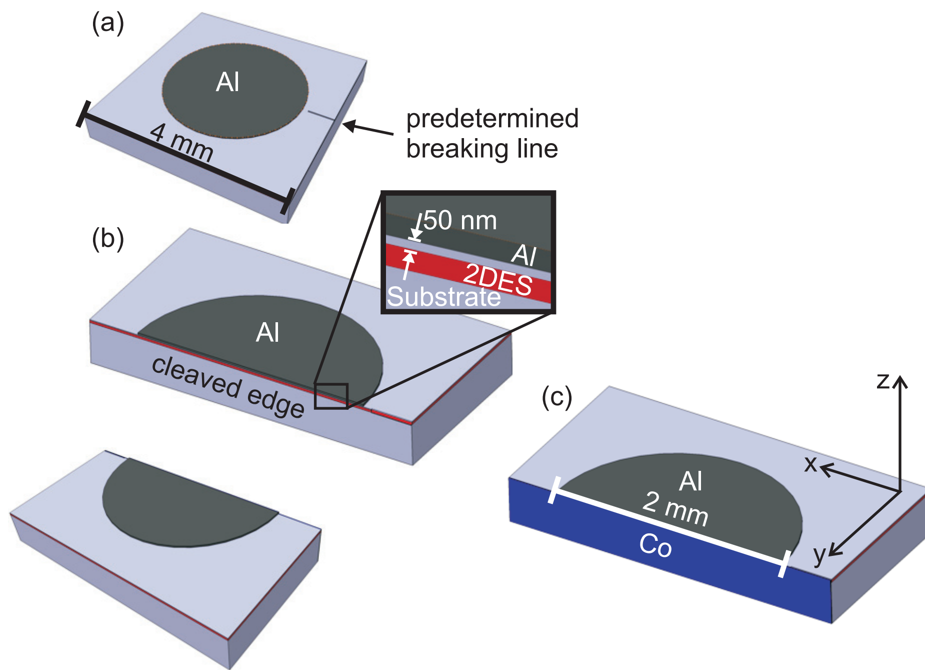

Figure 3.11: Schematic preparation sequence of the sample used for detecting photovoltages under microwave irradiation. (a) 4×4 mm^2 piece of the InAs heterostructure as described in section 3.1.1, here with an Al contact. (b) Sample after in situ cleavage. The inset shows that the Al contact and the 2DES are separated by only 50 nm. (c) A Co layer is evaporated on the cleaved edge connecting the 2DES and the Al contact. The dimensions of the 2DES/Al junction are 2 mm $\times$ 50 nm.

3.2.1 Measurement setup for spin battery devices

Concerning the microwave setup and the measurement technique we give just a rough overview in this subsection. Details can be taken from [Gie05], [Pod06] and [Bot06a][4]. With this setup two experiments are performed. For both experiments we use the same sample design as presented above in this section. The sample is placed on a coplanar waveguide (CPW) with the Co film face down. We assume that the spacing between the Co film and the CPW is in the range of an average dust particle, i.e. $\sim 1\ \mu$m. It is aligned such that the 2DES and the Al contact are standing on the central conductor which has a width of 200 μm. This setting is drawn in figure 3.12(a). A CPW is

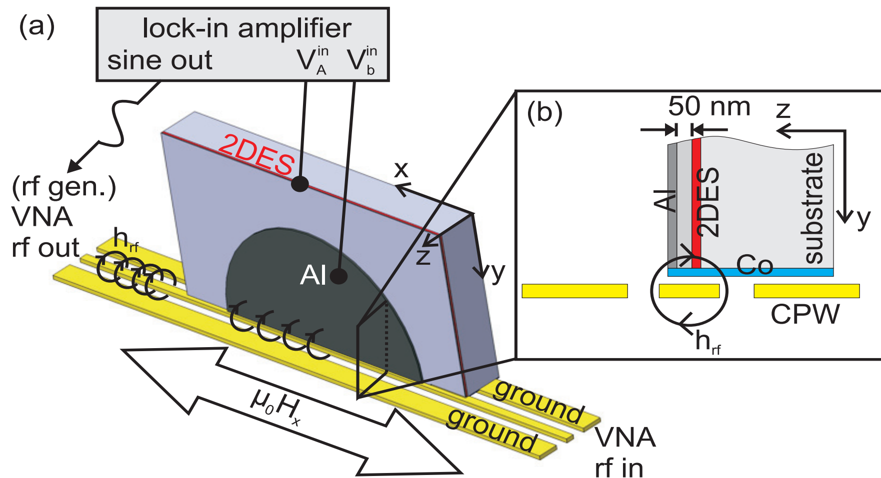

Figure 3.12: Setup to measure the FMR and the photovoltage. The sample is aligned along the coplanar wave guide (CPW). A microwave generator (rf gen.) or a vector network analyzer (VNA) generates a microwave signal through the CPW. The magnetic component $\boldsymbol{h}_{rf}$ of the microwave is indicated. To magnetize the Co layer we apply a magnetic field $\mu_0 H$. With the lock-in amplifier the rf amplitude can be modulated. We measure the transmission coefficient of the rf signal and the voltage between the Al contact and the 2DES. (b) shows a cross section of the Al/Co/2DES hybrid structure.

used to guide microwaves. It is important not to short the central conductor and the grounds. The microwaves are generated by a vector network analyzer (VNA) by *Hewlett–Packard, HP8720C*. The VNA detects the rf signal transmitted through the CPW and provides the transmission matrix $\boldsymbol{S}$. This matrix depends on the quality of the wave guide, connectors and on the absorption of the sample on the CPW. The output rf frequency f ranges from 50 MHz to 20 GHz with a maximum output power P_{rf} of 20 dBm. For rf sweeps in section 8.1 we use a resolution of 1600 steps within the range between 50 MHz and 20 GHz.

If a rf signal is present, it causes a high frequency magnetic component $\boldsymbol{h}_{rf}$ that surrounds the central conductor as shown in figure 3.12(b). We simulated the rf field using the commercial software *CST microwave studio*[5]. Figure 3.13 depicts the field distributions for the Co film positioned at a distance of (a) 1 μm and (b) 50 μm above the CPW. P_{rf} is 30 dBm. The maximal magnitude of $\boldsymbol{h}_{rf}$ at the Co film is 684 A/m in

[4]Thesis in German language
[5]www.cst.com

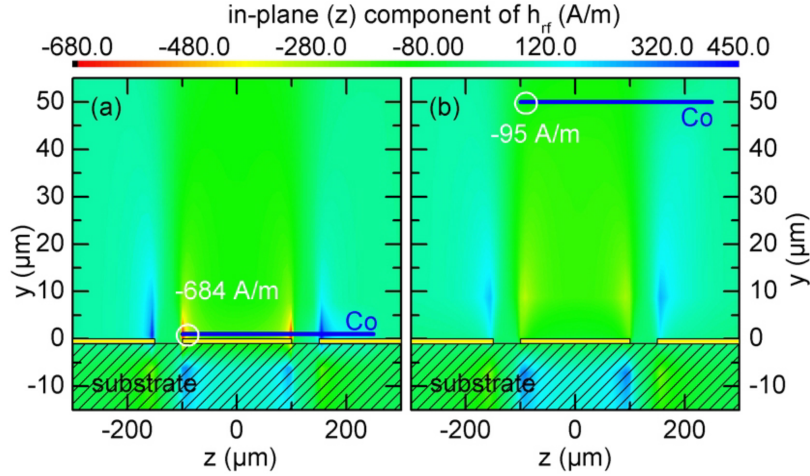

Figure 3.13: Simulated amplitude of the z component of the rf magnetic field. The yellow rectangles indicate the position of the CPW. The blue line shows the position of the Co film. In (a) it is 1 μm above the CPW, in (b) it is 50 μm above the CPW.

(a) and $\sim$ 95 A/m in (b) within the white circles in the graphs. This is the position of the Al/Co/2DES junction. On top of the CPW $\boldsymbol{h}_{rf}$ points predominantly in z direction, perpendicular to the 2DES and the Al contact and in the plane of the Co film. The y component of $\boldsymbol{h}_{rf}$ was also extracted and found to be one order of magnitude smaller. To calculate $\boldsymbol{h}_{rf}$ for other rf powers we exploit the proportionality between $\boldsymbol{h}_{rf}$ and the current I_{rf} in the CPW according to the Biot–Savart law. We use

$$I_{rf}\left(P_{rf}\right) = \sqrt{\frac{P_{rf}\,[\mathrm{mW}]}{50\ \Omega}} \quad \text{and} \quad \frac{I_{rf}\left(P_{rf,\,1}\right)}{I_{rf}\left(P_{rf,\,2}\right)} = \frac{\boldsymbol{h}_{rf,\,1}}{\boldsymbol{h}_{rf,\,2}}\ . \tag{3.2}$$

We apply a magnetic field $\boldsymbol{H}$ to magnetize the Co film. The maximum field is $\mu_0 H =$ 130 mT. It is applied in x direction and, for reference measurements, in z direction. If the Co layer is magnetized in x direction and $\boldsymbol{h}_{rf}$ in z direction, the magnetization $\boldsymbol{M}$ is forced to precess. At resonance frequency the absorption is enhanced. Thus, with this setup we determine the FMR of the FM on the CPW as a function of H_x.

In a second type of experiment presented in section 8.2 we detect the microwave induced dc voltage V_{dev} across the hybrid structure. We use a microwave generator (*Hewlett–Packard, HP83752B*) and perform rf sweeps from $f = 1$ GHz to 15 GHz in 1400 steps at a rf power of typically $P_{rf} = 8$ dBm. If other parameters are used it is indicated separately. A sine voltage of 5 V (rms) generated by the LIA modulates the rf amplitude by 5 dBm. We connect the 2DES to the V_A^{in} and the Al contact to the V_B^{in} input of the LIA which has an input impedance of 50 MΩ and measure $\partial V_{dev}/\partial P_{rf} = \partial\left(V_A^{in} - V_B^{in}\right)/\partial P_{rf}$. The wires are connected to the sample with conductive silver. It is important to use shielded and twisted wires to reduce the coupling of the microwave to the measurement signal. We measure V_{dev} as a function of the rf frequency and of the magnetic field H_x.

Chapter 4

Spin–orbit interaction in InAs quantum well structures

In sections 2.2 and 2.5 we outlined the importance of the spin–orbit coupling and its tunability for our experiments. To investigate theoretically the band structure properties and spin–orbit interaction of the InAs heterostructure presented in subsection 3.1.1 we established a cooperation with the research group of P. Vogl at the *Walter Schottky Institut, Technische Universität München*.

First, P. Vogl calculated the energy states that result from the material properties and the quantization conditions of this heterostructure using a tight–binding model. The formalism allows to simulate applied electric fields ε_z^{ext} in z direction, i.e. in growth direction of the heterostructure. Figure 4.1 shows the first and the second electron energy levels E_1 and E_2 and the highest hole energy level E_0.

Further the material sequence is indicated. In the simulation we focussed on the relevant region of the heterostructure consisting of the InGaAs/InAs/InGaAs asymmetric QW and the InAlAs spacer layer. Here the probability density Ψ^2 for the 2D electrons is non–zero. The exact layer thicknesses are $d_{InAlAs} = 2.2$ nm, $d_{InGaAs} = 2.4$ nm, $d_{InAs} = 4.0$ nm and $d_{InGaAs} = 13.5$ nm remodeling the QW used in our experiments. The electron states in the conduction band are assumed to be unoccupied, whereas E_0 is fully occupied. The intrinsic asymmetry of the band structure due to asymmetric modulation doping is not included. The solid (dotted) red (green) lines are the calculated edges of the valence and the conduction bands for $\varepsilon_z^{ext} = 0$ kV/cm ($\varepsilon_z^{ext} = 250$ kV/cm). This calculation is based on the interpolated energy gaps of the bulk materials including strain effects. E_1 is confined within the barriers of the InAs QW for electric fields $\varepsilon_z^{ext} \leq 250$ kV/cm. The calculated energy gap of the InAs between the highest hole state and the lowest electron state is $\Delta E_g = E_1 - E_0 = 0.6$ eV and further $E_2 - E_1 = 125$ meV. From experimentally determined values we estimate the Fermi energy according to

$$E_F = \frac{\hbar^2 k_F^2}{2m^*} = \frac{\hbar^2(2\pi n_{2D})}{2m^*} \ .$$

With $n_{2D} = 3.9 \times 10^{11}$ cm^{-2} from section 7.1.2 and $m^* = 0.039\, m_e$ from [Hu03] we obtain $E_F = 24$ meV. As $E_2 - E_1 << E_F$ the second electron energy level can be assumed to be unpopulated.

In the next step the BIA and SIA based spin–orbit coupling constants α_{BIA} and α_{SIA} for the first electron energy level E_1 are deduced from the energy splitting of

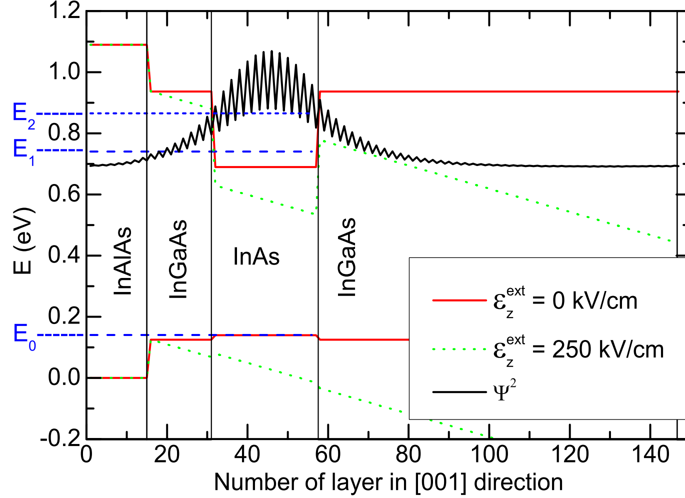

Figure 4.1: Calculated energy states for holes (E_0) and electrons (E_1 and E_2) of the InAs quatum well. The solid red (dotted green) lines indicate the band structure for an applied electic field $\varepsilon_z^{ext} = 0$ kV/cm (250 kV/cm). Ψ^2 is the probability density of the electrons with a maximum in the quantum well.

the conduction band for $k \to 0$. The behavior of α_{BIA} and α_{SIA} for ε_z^{ext} between 0 and 250 kV/cm is shown in figure 4.2(a). In our magnetotransport experiments the electrons are subject to a total spin–orbit coupling that is expressed by a total α and produces a spin splitting ΔE. To find this α we use equation 2.10 and, introducing polar coordinates, calculate the quantity $\Delta E/\,|k|$ in the (001) crystal plane as a function of the angle φ between $\boldsymbol{k}$ and the [100] axis. $\Delta E/\,|k|$ is a measure for the spin splitting. The curves in figure 4.2(b) show the results. For each electric field the respective α_{BIA} and α_{SIA} from (a) were used for the calculation. In the experiments presented in chapter 7 the electron transport takes place mainly collinear to the $[1\bar{1}0]$ crystal axis. This corresponds to $\varphi = 135°$ or $315°$, where the spin splitting for all ε_z^{ext} is maximal. Here equation 2.10 reads $\Delta E/\,|k| = \alpha_{BIA} + \alpha_{SIA}$. Thus, in our transport direction, the spin splitting results from the sum of α_{BIA} and α_{SIA}. This sum is also plotted in figure 4.2(a).

The total spin–orbit coupling parameter α varies with the external electric field. An almost linear increase is found. The calculations yield two important results that are in contrast to widespread assumptions and support recent experimental findings of the group of K. Ensslin [Mei07]: First, α_{BIA} is in the same order of magnitude as α_{SIA} and dominates the spin–orbit coupling. Second, the tunability of the spin–orbit coupling by an external gate voltage is based on a variation of α_{BIA} rather than on α_{SIA}. It was shown that the microscopic arrangement of atoms at the QW interfaces, rather than the macroscopic field, determines the spin–orbit coupling [Maj00]. Thus, we attribute our striking results to the fact that polarization effects at the interface are included in our atomistic model of the InAs heterostructure.

To demonstrate the electric field dependence of the spin–orbit coupling we perform

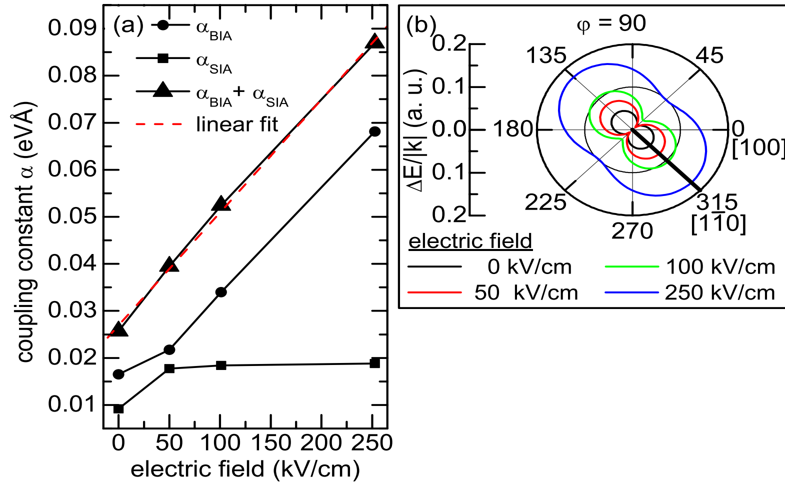

Figure 4.2: (a) Spin–orbit coupling constants for E_1 due to bulk inversion asymmetry (BIA) and structure inversion asymmetry (SIA). The calculations were performed by P. Vogl for an InAlAs/InGaAs/InAs/InGaAs/InAlAs asymmetric quantum well (see figure 4.1). (b) $\Delta E/|k|$ is a measure for the spin splitting. In [1$\bar{1}$0] direction the splitting is maximal for all ε_z^{ext} and $\alpha = \alpha_{BIA} + \alpha_{SIA}$ is valid.

a linear fit of the $\alpha_{BIA} + \alpha_{SIA}$ curve and obtain $\Delta\alpha/\Delta\varepsilon_z^{ext} = 2.7 \times 10^{-11}$ (eV)m/V. We conclude that a tunability of the spin–orbit coupling with an external electric field is predicted for the InAs heterostructures used in this work. However, the calculated absolute values of α are a factor of 10 smaller than calculated from experimental magnetotransport data [Gru00] and spectroscopy [Hu03] (see table 2.11). One might speculate that not considering the additional electric field due to the incorporated doping layer in the real sample leads to this difference.

Chapter 5

Calculated impact of a gate voltage

The calculations presented in the following are performed with the simulation software *nextnano*^{3} in the framework of a collaboration with S. Birner[1].

For the interpretation of the results in section 7.2 it is important to know the influence of the applied gate voltage V_{gate} on the InAs based 2DES in our devices. We can not use a simple electrostatic calculation, because V_{gate} is applied between the gate electrode on the cleaved edge and the drain contact and no back–gate is implemented. The geometry for with the simulations are performed is illustrated in figure 5.1(a). Implementing such a field–effect electrode goes beyond the work of R. Haug [Hau92]. He used macroscopic source and drain contacts on the cleaved edge of a 20 nm wide InAs QW to observe 1D electron transport behavior without being able to vary the electric field in the plane of the 2DES.

For the simulation we set the potential of the gate electrode to −6 V and both, the source and the drain contact to 0 V. Using the *nextnano*^{3} software we calculate the potential landscape of the device. For this we use a classical approach and the software solves the Poisson equation self–consistently. A detailed description of the software is published in [Tre06]. The band parameters for InAs are taken from the review paper of I. Vurgaftman et al. [Vur01]. Further input values and values that differ from standard material parameters are summarized in table 5.1.

parameter	**value**
temperature	4.2 K
carrier density in the 4 nm wide QW	5×10^{17} cm^{-3}
dielectric constant InAs	15.15
conduction band mass InAs	0.026 m_e

(5.1)

The simulation returns the potential distribution in the x–y plane. It is plotted in figure 5.1(b) on a relative scale. The gate electrode area as well as the source and drain contact areas are not included in the calculation. The magnitudes of their potentials are set manually below the calculated area to highlight these areas. The major part of the potential difference drops almost linearly in the region of the SiO_2. As expected, the metallic contacts are equipotential areas. Between the contacts the potential increases

[1] Member of the research group of P. Vogl at the Walter Schottky Institut, Technische Universität München, CEO of *nextnano*^{3} (www.nextnano.de).

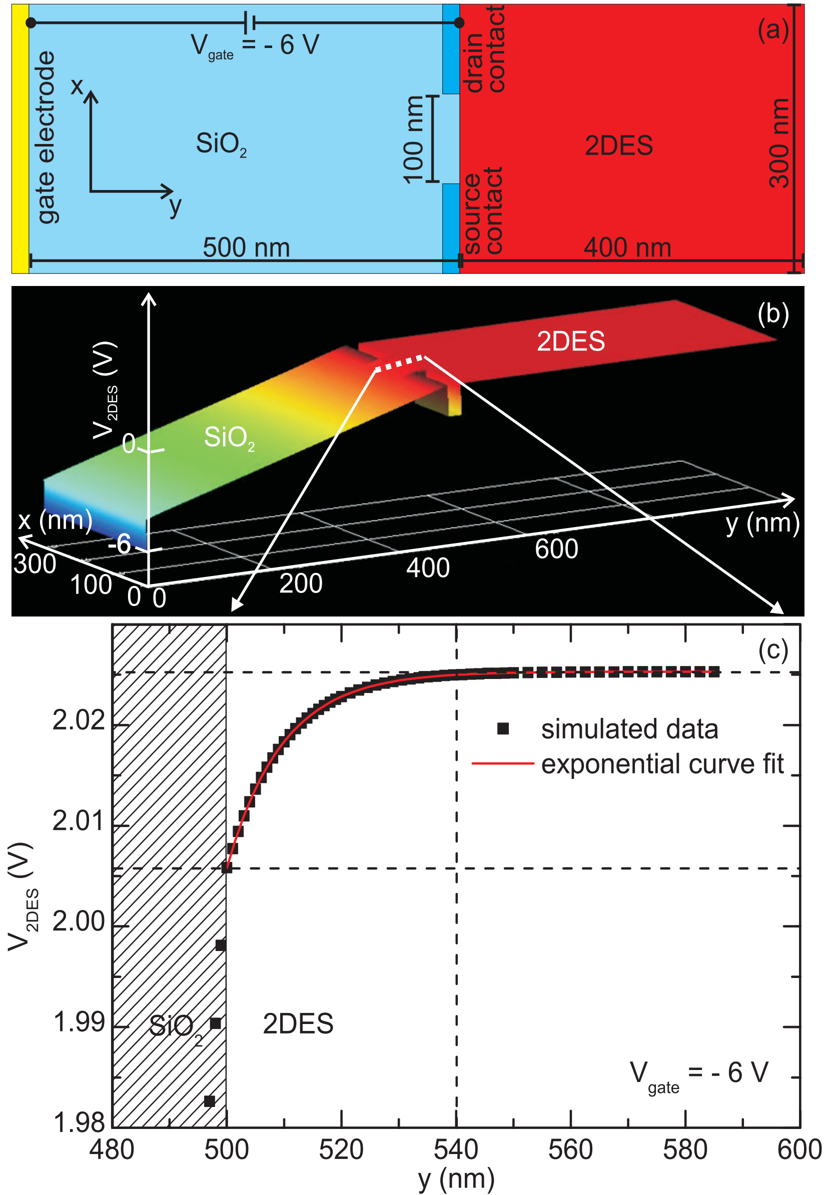

Figure 5.1: (a) Model of the hybrid structure that was used to simulate the potential distribution. (b) Potential landscape for an applied gate voltage of −6 V between the gate electrode ($y = 0$ nm) and the drain contact ($y = 480$ nm). The dotted line indicates the 2D cross section plotted in (c). The graph illustrates the distance of the potential drop in the 2DES between the source and the drain contact.

almost with the same slope as within the rest of the SiO_2. To find out how far the potential drop penetrates into the 2DES we plot a cross section of the interface region. Figure 5.1(c) shows the potential V_{2DES} along the dotted line in (b). We fitted the exponential equation

$$V_{2DES} = 2.03 \text{ V} + 4.64 \times 10^{20} \cdot 0.90^{y} \text{ V} \qquad y \text{ in [nm]}$$

to the data within the 2DES region. The potential saturates exponentially within 40 nm. Within this distance the potential V_{2DES} rises from 2.006 V to 2.025 V. In a linear approximation this corresponds to an electric field of $\varepsilon_y = 4.75$ kV/cm in the 2DES. We further found in our calculations that the penetration depth of the potential depends on the carrier density n_{2D}. The higher n_{2D} the smaller the penetration depth.

In figure 5.2(a) a cross section through the potential landscape in the 2DES is plotted for different gate voltages. The cross section covers a distance of 40 nm in y

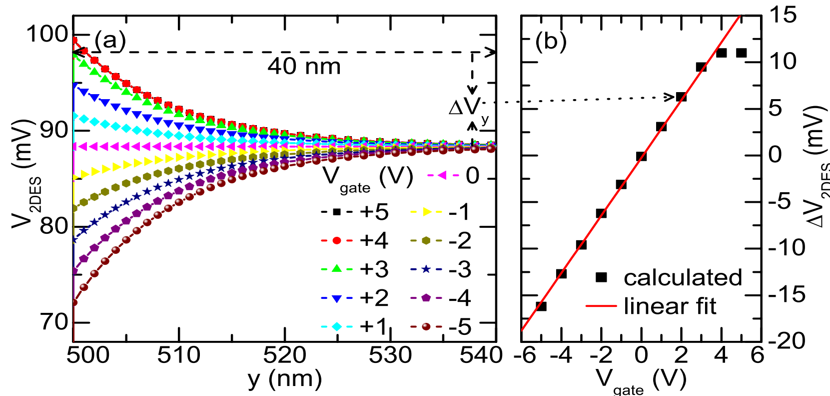

Figure 5.2: (a) Cross section through the potential landscape in the 2DES at $x =$ 150 nm for different gate voltages. (b) Potential drop ΔV_{2DES} in the 2DES between $y = 500$ nm and 540 nm as a function of the gate voltage.

direction starting from $y = 500$ nm at $x = 150$ nm, i.e. right between the source and drain contacts (compare figure 5.1(a)). In figure 5.2(b) the voltage drop across a 40 nm distance in the 2DES is plotted as a function of V_{gate}. A linear fit of the data points excluding the point at $V_{gate} = 5$ V yields the equation

$$\Delta V_{2DES} \text{ [mV]} = -0.3 \text{ V} + 3.1 \cdot V_{gate} \text{ [V]} \ . \tag{5.2}$$

For $|V_{gate}|$ exceeding the range plotted in figure 5.2(b) the values of ΔV_{2DES} saturate. This behavior is a result of the way the software simulates the band structure of the device and is an artefact.

In figure 5.3 the distribution of the electron density is displayed for a potential of -6 V at the gate electrode and 0 V at the source and drain contact. The density of free electrons is zero in the SiO_2 area and takes a constant value in the 2DES. A reduced density is found in the area of the 2DES between the source and the drain contact. This is expected because the negative applied potential acts repulsive on electrons. So

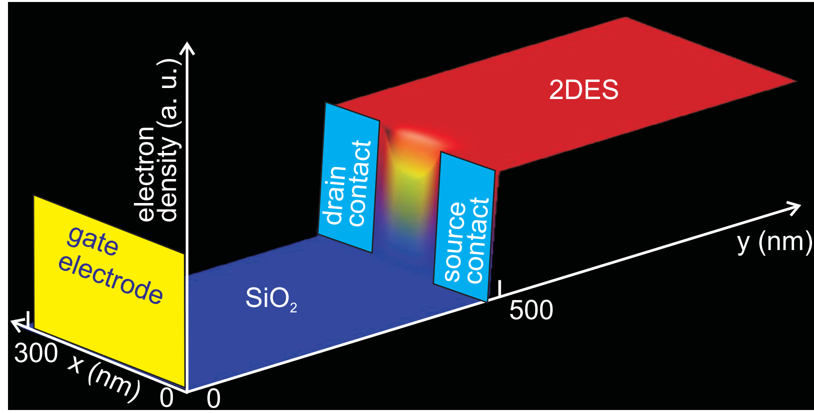

Figure 5.3: Simulated electron density distribution in the gate oxide and the 2DES of our hybrid structure. A potential of −6 V is applied at the gate electrode. At the source and the drain contact the potential is set to zero.

we found that we can tune the electron concentration in the 2DES channel with V_{gate}. The depleted area is limited in y direction to about 40 nm. In subsection 7.2.1 we report a measured change of n_{2D} as a function of V_{gate}. This means that we are sensitive to electron density variations within an area of only 100×40 nm^2 with our magnetotransport measurements. In subsection 7.1.1 we calculate a spin scattering length of 19 nm. We conclude that we mainly modulate the electric field (and therewith n_{2D}) of an area of the 2DES where quasi–ballistic spin transport is expected.

Chapter 6

Calculations on spin dependent transport

To understand the spin polarized transport in our devices we performed computer simulations based on a nanoscopic FM/InAs/FM device. The software was written and adapted by T. Kubis[1] in the framework of a cooperation. The algorithm is based on ballistic nonequilibrium Green's function theory in envelope function approximation. From this the current transmission through the device is obtained. The software allows one to include a gate voltage V_y and to consider spin–orbit coupling in the SC.

First the device geometry is defined. The chosen geometry remodels our real device structure (see section 3.1) within the limits given by the software and the computation time. The simulated device is shown in figure 6.1. It consists of a 70×40 nm^2

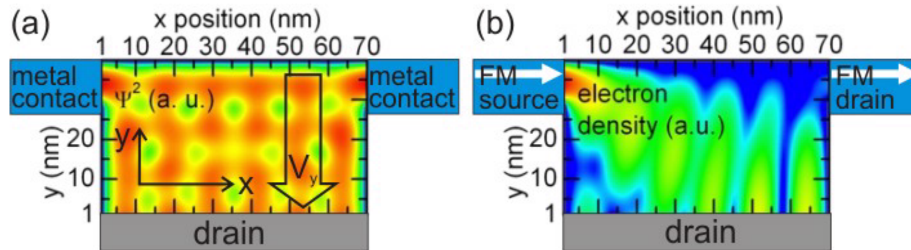

Figure 6.1: Simulation of a 70×40 nm^2 InAs mesa containing a 2DES. (a) Square of the electron wave function reflecting the allowed electron states. No current is applied. The amplitude in the red (green) regions is high (low). (b) A spin polarized current enters the device from the FM source contact. The color–scale plot shows the calculated electron density distribution. Red (blue) indicates a high (low) electron density.

rectangular InAs mesa with metallic source and drain contacts attached to the upper left and right corner. By defining a spin splitting of the electron energy, these contacts behave like FM. The magnetization of these contacts is indicated by the white arrows in figure 6.1(b). At the lower boundary an additional drain contact is attached to simulate an infinite device extension in $-y$ direction to model our real devices. The confinement at the upper, left and right boundary is realized by potential barriers

[1]Member of the research group of P. Vogl at the Walter Schottky Institut, Technische Universität München.

with $e \cdot V_{barrier} >> E_F$. Due to the confinement the simulations are very sensitive to the assumed device geometry. If e.g. the length is changed by a few nanometers the device's transmission coefficient might change from a finite value to zero. Since we observe transmission in our experiment we adapted the length appropriately to model our observation.
We simulated a gate voltage V_y that tilts the conduction band along the y direction as indicated by the arrow in figure 6.1(a). V_y is applied between a gate electrode at $y = 0$ along the edge of the device and the lower drain electrode. It is constant in x direction throughout the structure.

6.1 Calculating the transmission function

In a first step the square of the wave function Ψ^2 and the electron density distribution are calculated for $V_y = 0$. The results are shown in figure 6.1(a) and (b). The plots give a qualitative overview of the generated conditions in the structure. In (a) the allowed electron states are depicted. We observe a periodically modulated Ψ^2 that indicates nodes and bellies of the electron wave function Ψ. This is expected for a nanoscopic quantum mechanical system. In (b) one can see how the electrons distribute across the InAs if a finite electron concentration is assumed in the source contact, whereas the electron concentration is set to zero in the drain contacts. Dark blue areas indicate a low density. At the drain contact the density is low due to a displacement of the electron density towards the lower drain. We conclude that the large extension of the device in y direction leads to a reduced electron density at the drain contact.
By comparison of figures (a) and (b) we find that the electron density is governed by the probability density function. From (a) we deduce the important information that Ψ^2 is large at both, the source and drain contact. This means that they are interconnected and the transmission is non–zero.

In figure 6.2 the calculated transmission T from the source to the drain contact is plotted as a function of the electron energy. The black squares in (a) show the original output data of the simulation. No spin dependent energy splitting is effective in the metal contacts and V_y, as well as the spin orbit coupling in the device are set to zero. T is normalized to a maximum value of 2, what represents the sum of two spin channels. The curve with the filled squares shows its first nonzero value at a minimum energy of $E_1 = 105$ meV. This energy is necessary to initiate a transmission and equals the lowest resonant state of the device. With increasing electron energy the second energy state of the system at $E_2 = 146$ meV is populated. At this energy we observe the second peak in the transmission curve. We define the energy in this system such that $E_1 = 0$. This is why we shift the transmission function by E_1. The result is depicted in figure 6.2(a) using filled circles.

To enable a qualitative comparison of these simulations with our transport experiments we find a relation between the calculated transmission and the voltage drop measured between the source and the drain contact in an experiment. The current density through the device is proportional to the integral over the transmission times the Fermi distribution f_F,

$$j\left(E_F\right) \propto \int_{E_F - e\Delta V/2}^{E_F + e\Delta V/2} T\left(E\right) f_F(E) dE \ .$$

We integrate over a small energy interval around the Fermi energy E_F which is defined

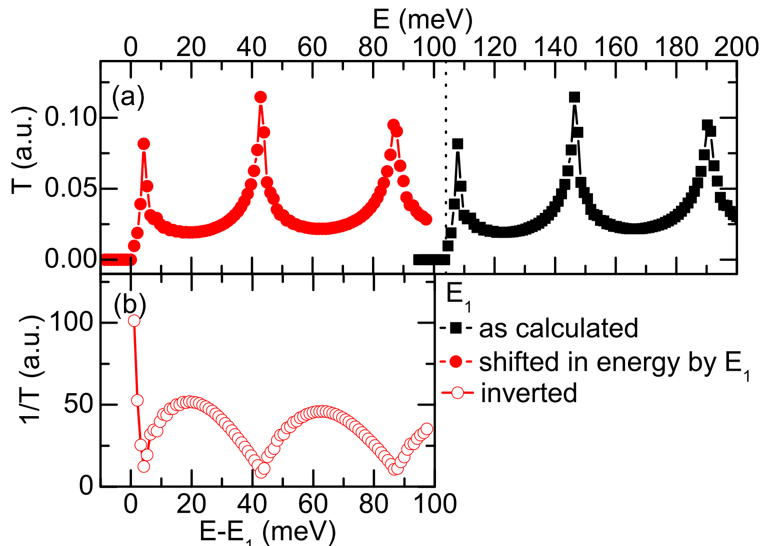

Figure 6.2: Calculated transmission for the device geometry shown in figure 6.1. (a) The filled squares represent the original data. They are shifted in energy for later comparison (filled circles) such that the transmission starts at zero electron energy. (b) The inverted transmission data is shown. In a transport measurement the observed signal is proportional to this quantity.

by the source–drain voltage ΔV. At low temperatures one can assume $f_F = 1$ for $E - E_1 < E_F$ and $f_F = 0$ for $E - E_1 > E_F$. Further, for small ΔV, the transmission is approximately independent of the energy. So we find

$$j\left(E_F\right) \propto T\left(E_F\right) \int_{E_F - e\Delta V/2}^{E_F + e\Delta V/2} dE = T\left(E_F\right) \cdot e\Delta V \ .$$

In a transport experiment we measure the voltage drop across the device at a fixed bias current. Thus the proportionality

$$\Delta V\left(E_F\right) \propto \frac{1}{T\left(E_F\right)}$$

will be observed if E_F is varied. This is plotted in figure 6.2(b). As the inverted T is experimentally accessible we will focus on this quantity in the rest of the chapter.

6.2 Gate voltage dependent transmission

In the following we discuss the effect of an applied voltage in y direction. A nonzero V_y affects the potential landscape and the electron wave function in the device. Accordingly, E_1 changes. As described above, we shift each curve by its particular value E_1 to compare the curves for different V_y. By this means the transmission of each curve has its first nonzero value at $E - E_1 = 0$. This implies that in this simulation the Fermi

energy in the device exclusively determined via the contact states, i.e. the electron density in the InAs is zero without contacts. Figure 6.3(a) shows exemplarily 5 out of 11 inverted transmission curves for V_y between +100 mV and −50 mV. As shown

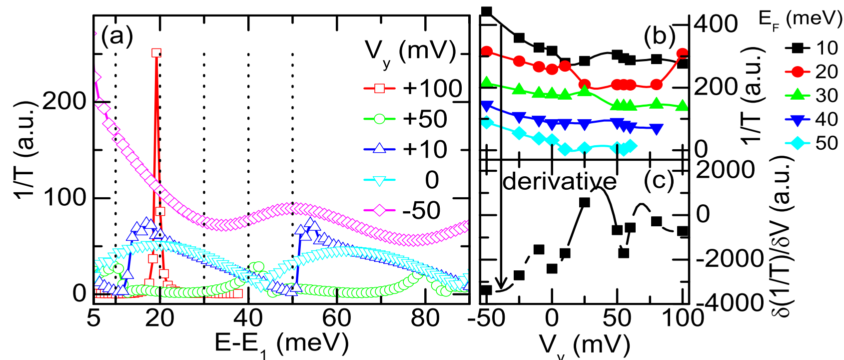

Figure 6.3: (a) Inverted transmission through a NM/InAs (2DES)/NM junction calculated for different voltages V_y applied across the device in y direction. The electrons are not spin polarized and the spin–orbit coupling in the 2DES is set to zero. Thus no spin effects occur. (b) Inverted transmissions as a function of V_y. The curves are offset for clarity. Each curve represents a different energy indicated by the dotted lines in (a). Graph (c) is the derivative of the $1/T(V_y)$ curve at $E_F = 10$ meV. It represents the signal measured in a transport measurement with V_y modulated with time.

above, the inverted transmission is proportional to the voltage signal of a transport measurement. The magnetization of the source and the drain contact is switched off by setting the spin dependent energy splitting ΔE_S to zero. This means that the contacts are nonmagnetic and the current is not spin polarized. Further the spin–orbit coupling constant α is set to zero. Under these conditions we can observe the influence on the transmission if *only* the electric field is varied but *not* the spin–orbit coupling. For high positive V_y we find low values of $1/T$ indicating low device resistances. This is an expected behavior because positive V_y attract electrons towards the region between the source and the drain electrode. Later in this section we will show that the conduction band is lowered at $y = 0$ and obtains a triangular shape at the edge of the InAs. This is reflected in the transmission curves by a shift of the peak positions for different V_y.

We assume different Fermi energies between $E - E_1 = E_F = 10$ meV and 50 meV. These are indicated by the dotted vertical lines in figure 6.3(a). The values of $1/T$ for each V_y along these lines is plotted in figure 6.3(b). The curves are offset for clarity. We find that the transmission variation is not strictly monotonic as a function of V_y. The characteristics of a $1/T\,(V_y)$ curve depends on the Fermi energy. An oscillating behavior occurs which is more pronounced for lower E_F. The curve at $E_F = 10$ meV shows the highest total variation of $\Delta\,(1/T) = -160$. This corresponds to an absolute value of the relative variation of $\Delta\,(1/T)\,/\,(1/T_{low}) = 100\,\%$.

In our experiments we modulate the gate voltage as a function of time (see section 3.1.8). Thus, the measurement signal is proportional to $\partial V_{dev}/\partial V_y$ according to equation 3.1. To compare the findings in this section qualitatively with the experiment we calculate the derivative of the $1/T\,(V_y)$ curve. The result is shown in 6.3(c). The data

points are connected with spline curves as a guide to the eye. We find that this curve exhibits 3 full oscillations within the given range of V_y. The amplitude covers 3 orders of magnitude.

To find out whether the observed characteristics of the $1/T\,(V_y)$ curve is spin dependent or not, we recalculated the curves in figure 6.3 with spin polarized current. This is realized by assuming parallel $\boldsymbol{M}$ of both contacts with a spin dependent energy splitting of $\Delta E_S = 2$ meV. This value of ΔE_S is underestimating the spin splitting in a real FM. But in the simulations we neglect spin scattering at the interfaces that depolarizes the current. The smaller ΔE_S is intended to mimic a realistic spin polarization in the InAs. The spin–orbit coupling α is set to zero. The software distinguishes between the two spin polarizations parallel and antiparallel to the magnetization direction $\boldsymbol{M}$ of the source contact. The transmission T is the sum of both spin orientations. In figure 6.4 the data with polarized current (filled symbols) is compared with the data for unpolarized current (open symbols). The data are offset for clarity. If any spin

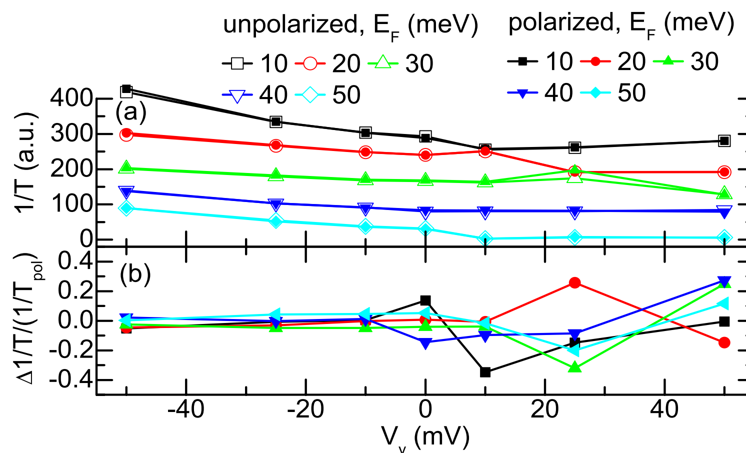

Figure 6.4: Inverted transmission as a function of the applied voltage in y direction. Different symbols represent different E_F. In (a) the open symbols are calculated with unpolarized current. For the filled symbols a nonzero Zeeman splitting is effective in the source and drain contacts. In (b) the relative difference between the unpolarized and the polarized curves is plotted for each E_F.

dependent effect was present in our calculation we would expect different transmission characteristics comparing the results for spin polarized and unpolarized current. In (b) we calculated the relative difference according to $(T_{unpol} - T_{pol})/T_{pol}$. Below $V_y = 0$ meV the relative deviation of the polarized dataset is below 10 % whereas for positive V_y the relative deviation increases to absolute values above 30 % at $E_F = 10$ meV and 30 meV. We conclude that a variation of V_y does not affect electrons of both spin orientations equally. The transmission is spin dependent, although the spin orbit interaction α in the InAs is set to zero in this simulation. We explain this behavior with the splitting of the energy states in the contacts for the spin polarized case. The splitting of $\Delta E_S = 2$ meV changes the matching condition with the electron states in the InAs that propagate from the source to the drain contact.

In a real device not only the potential landscape but also the Fermi energy changes in the presence of a gate voltage. In our devices the gate voltage is applied in y direction between the gate electrode and the source and drain electrodes (see figure 5.1(a)). We used *nextnano*^{3} to determine the dependence of E_F on V_y. Accordingly, in this case E_F is not related to E_1 but an absolute quantity. The potential curves in figure 5.2(a) represent the negative of the conduction band edges. In the simulations the energies $E_{CB}(y)$ of the conduction band edges are calculated relative to $E'_F = 0$. Thus, to determine the Fermi energies we use $E_F = E'_F - E_{CB}\,(y = 500\text{ nm})$. Note the different y scale in chapter 5. This quantity is evaluated as a function of the respective potential drop V_y across a distance of 40 nm in the InAs for each gate voltage. We find a linear behavior of $E_F\,(V_y)$ with a slope of nearly 1. A variation of E_F is expected, as the electron density varies locally within 40 nm from the edge of the InAs between the source and drain contacts as a function of V_y. In figure 6.5(a) the inverted transmission is plotted for different V_y. For clarity we plotted only 3 out of 7 curves.

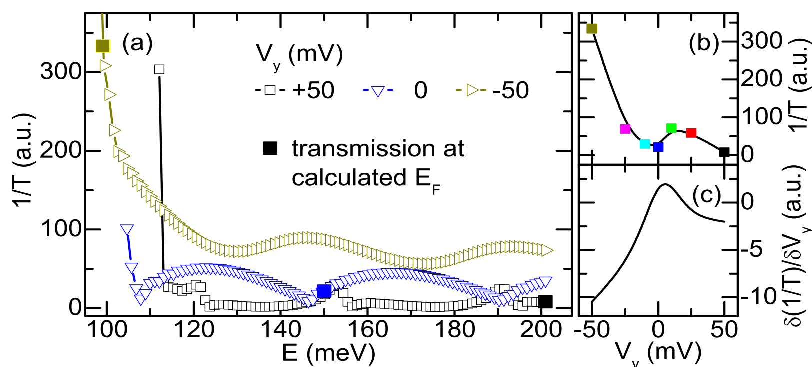

Figure 6.5: (a) Inverted transmission through a NM/InAs (2DES)/NM junction for three different voltages V_y. The filled squares represent the calculated Fermi energies for the respective gate voltages. (b) The transmission at E_F as a function of the gate voltage exhibits oscillatory behavior is shown. Here we included results from additional calculations of $1/T$ for 7 different V_y. The line is a guide to the eye. (c) Derivative of the curve in (b) representing the signal expected for a transport measurement with modulated gate voltage.

The spin dependent energy splitting in the contacts and the spin–orbit coupling in the InAs are set to zero. Unlike in figure 6.3(a), here the curves are not shifted by E_1. A constant offset is added to the calculated E_F such that the Fermi energy is above the energy E_1 at which transmission is initiated for all $1/T$ curves. The positions of the E_F are plotted as a filled squares for each curve in (a). The values of $1/T$ at E_F are shown in (b) as a function of V_y. Note that in this graph data points from 7 calculated inverted transmission curves are plotted. The squares at $V_y = +50$ V, 0 V and -50 V are plotted in the same color as the respective data in (a). The line is a guide to the eye and indicates that $1/T$ exhibits one full oscillation between $V_y = -25$ mV and $+25$ mV. According to equation 5.2 this range will be covered by gate voltages from -8 to $+8$ V what is experimentally accessible. So again, an oscillatory behavior is observed in absence of spin–orbit coupling in the InAs.

In 6.5(c) the derivative $\partial\left(1/T\right)/\partial V_y$ is plotted. The oscillation period is longer than in the oscillations shown in 6.3(c). Further, the amplitude is reduced by about a factor of 10. Transferred to real devices this means that substantially different measurement signals are expected if the electron concentration (i.e. Fermi energy) is kept constant and if the electron concentration changes with an applied gate voltage. We point out that so far no spin–orbit coupling effects were considered in this section.

6.3 Spin–orbit coupling dependent transmission

Now we investigate the complementary case: We keep the potential V_y fixed at $V_y = -10$ mV and the varied parameter is the strength of the spin–orbit coupling α. At constant V_y the Fermi energy does not change. Thus, for qualitative investigations of the $1/T(\alpha)$ behavior we use the same data interpretation procedure as in figure 6.3 in the previous section. We define parallel magnetizations of the source and drain contacts with $\Delta E_S = 2$ meV and vary α between 0 and 0.25 eVÅ. The resulting inverted transmission curves are shown in figure 6.6(a).

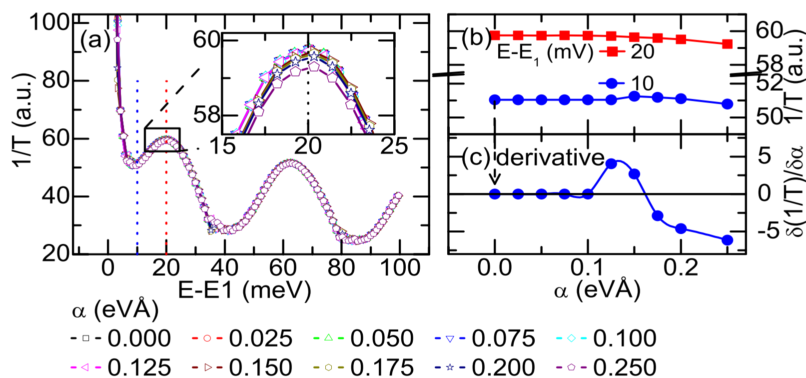

Figure 6.6: Inverted total transmissions for different spin–orbit coupling strengths α. We use $V_y = -10$ mV. (a) shows $1/T$ as a function of electron energy for parallel magnetization of the source and the drain contacts. The inset is a blow-up of the region around $E - E_1 = 20$ meV. In (b) $1/T$ is plotted as a function of α for 10 meV and 20 meV. (c) is the derivative of the $1/T\left(\alpha\right)$ at $E - E_1 = 10$ meV. It represents the measured signal in a transport experiment where α is modulated periodically as a function of time.

The chosen tuning range of α is experimentally accessible (see section 2.2.2). The characteristic behavior of the transmission with energy is similar for different α, the small differences are emphasized in the inset. For $E - E_1 = 10$ meV and 20 meV (dotted lines in (a)) we investigate the variation of $1/T$ with α. Figure 6.6(b) shows the resulting curves. They exhibit small relative variations below 1 %. In section 6.2 we found for a variation of V_y at the same E_F an effect of 100 %. Accordingly, in our simulations the tuning of V_y has a higher influence on the device resistance than the tuning of α. This is a very important result for the discussion of the oscillations observed in experiments on our real devices in section 7.2.

Figure 6.6(c) shows the derivative of the $1/T(\alpha)$ curve at $E_F = 10$ meV. The data points are connected with spline curves to guide the eye. The derivative represents the expected signal measured with a LIA and α modulated at lock–in frequency. In contrast to the $1/T(\alpha)$ curve in (b) the derivative exhibits a significant oscillation between $\alpha = 0.1$ eVÅ and 0.2 eVÅ. The amplitude is 3 orders of magnitude smaller than the signature shown in figure 6.3(c).

We conclude that in a transport experiment, where α is intended to be varied via a gate voltage as shown in section 2.5, one has to carefully distinguish between the signal resulting from the variation of the potential landscape and the spin–orbit related effect. An oscillating variation of $1/T$ can be caused independently by both parameters, V_y and α. The calculations suggest that the variation of the potential landscape with V_y predominantly changes $1/T$ in our nanoscopic device and not so much the spin–obit coupling itself.

6.4 Calculated giant magnetoresistance effect

In section 7.1.1 we report the investigation of the GMR effect in our device, i.e. the change in device resistance caused by switching from parallel to antiparallel magnetization $\boldsymbol{M}$ of the source and drain contacts (see subsection 2.3.4). The simulation of such an experiment is presented in the following. For different spin–orbit coupling strengths α and voltages V_y the transmission is calculated for the two magnetization configurations. The magnetization is tuned by adjusting the spin dependent splitting in the contacts to $|\Delta E_S| = 2$ meV. These data are plotted in figure 6.7(a). Filled (open)

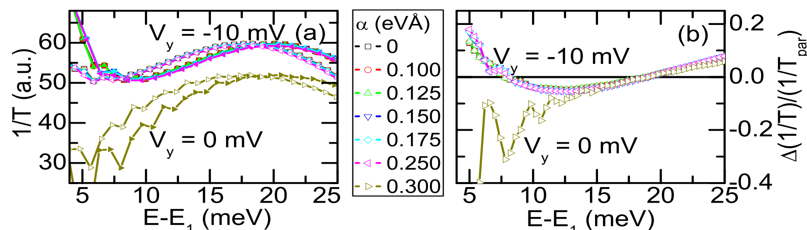

Figure 6.7: Graph (a) shows calculated inverted transmission curves for different spin–orbit coupling strengths. The offset energy E_1 is subtracted. Filled (open) symbols represent parallel (antiparallel) magnetization of the FM contacts. The values of V_y are given in the graph. In (b) the relative change in transmission for switching from parallel to antiparallel is plotted.

symbols are the simulated data with parallel (antiparallel) $\boldsymbol{M}$. For $\alpha = 0$ to 0.25 eVÅ a voltage of $V_y = -10$ meV was set. Only the curve for $\alpha = 0.3$ eVÅ (right–pointing triangles) is calculated at $V_y = 0$. Consistent with figures 6.3 and 6.6 we determined the minimum energy E_1 at which the transmission obtains nonzero values and plotted the data as a function of $E - E_1$.

We find that switching the magnetization from parallel to antiparallel $\boldsymbol{M}$ shifts E_1 by 2 meV to smaller energies. This equals the magnitude of the spin dependent energy splitting in the contacts. The shift can be understood as follows: We assume that in

the source contact the majority spins are $\uparrow$ spins. The spin splitting is defined such that the energy of these $\uparrow$ electrons is raised by 1 meV. After travelling through the InAs, they find the energy state for the $\uparrow$ electrons also shifted up by 1 meV in the drain contact in the parallel configuration. In the antiparallel configuration the energy state for the $\uparrow$ electrons is shifted down by 1 meV in the drain contact. Consequently, a potential drop of 2 meV arises across the device for the $\uparrow$ spins when $\boldsymbol{M}$ of the drain contact is switched from parallel to antiparallel with respect to the source contact. This explains, why the energy of the first coherent state in the antiparallel configuration is 2 meV below E_1 of the parallel configuration.

The shift of the curves is reflected in the relative inverted transmission difference $\Delta\,(1/T)\,/\,(1/T_{par}) = (1/T_{par} - 1/T_{antipar})\,/\,(1/T_{par})$. This quantity is also called GMR effect (see section 2.3.4). It is plotted in figure 6.7(b). For all α between 0 eVÅ and $\alpha = 0.25$ eVÅ we find positive values for energies below $E - E_1 = 8$ meV and above 19 meV. Between these energies the GMR effect is negative. The total variation of the GMR effect was found to be 23 %. The curve for $\alpha = 0.3$ eVÅ shows a different behavior. In section 6.2 we demonstrated the strong impact of V_y on the transmission what explains the different GMR behavior of the curves for $V_y = -10$ meV and 0 meV. Our result predicts that the GMR effect can be tuned by the Fermi energy from positive to negative values. Experimentally the Fermi energy can be tuned by means of the persistent photo effect or a gate voltage. The effect depends on the spin dependent energy splitting in the drain contact and on the applied gate voltage.

Chapter 7

Magnetotransport measurements on spin FET devices

The data presented in this chapter are taken from Co/InAs (2DES)/Co hybrid devices that are fabricated as shown in section 3.1. The cryogenic measurement setup is explained in subsection 3.1.8.

Due to the complex sample design and the novel geometry of the hybrid structure we have to discuss separately the different MR effects in detail that have been observed. We have performed magnetotransport experiments in different configurations with respect to magnetic field, current and gate voltage in order to extract the characteristic properties of the FM contacts and the 2DES separately. In the first section we present data that show signatures of the GMR effect. In particular we will discuss the magnetic properties of the FM contacts and spin injection. Then we focus on the field effect. Here we demonstrate the influence of an applied gate voltage on the 2DES. In the second section we present the device resistance as a function of the gate voltage. We demonstrate that the MR effect that we observe, depends characteristically on the magnetic field angle and on temperature.

7.1 Magnetoresistance at fixed electron density

In this section we focus on electron transport from the FM source to the FM drain electrode and vary the magnetic field at constant electron density in the 2DES. No voltage is applied at the field–effect electrode (open contact).

7.1.1 Signatures of the GMR effect

The traces shown in figure 7.1 are typical magnetotransport measurements on sample 1146_34[1]. The orientation of H was parallel to the 2DES in the x direction. This geometry rules out effects caused by Landau quantization or by Lorentz force (see chapter 2) because magnetic field components perpendicular to the 2DES are not present. We applied an ac current of $I_{bias}^{ac} = 5$ μA from the source to the drain contact and measured the voltage drop ${V_{dev}}^2$ across the device at $T = 4.5$ K. The device resistance was calculated using $R_{dev} = V_{dev}/I_{bias}$. The squares (red curve) represent a section of the down–sweep from $\mu_0 H = +1$ T to $\mu_0 H = -1$ T, the circles

[1]Internal reference number of the sample: Wafer number 1146, piece number 34.

[2]*dev* stands for "device"

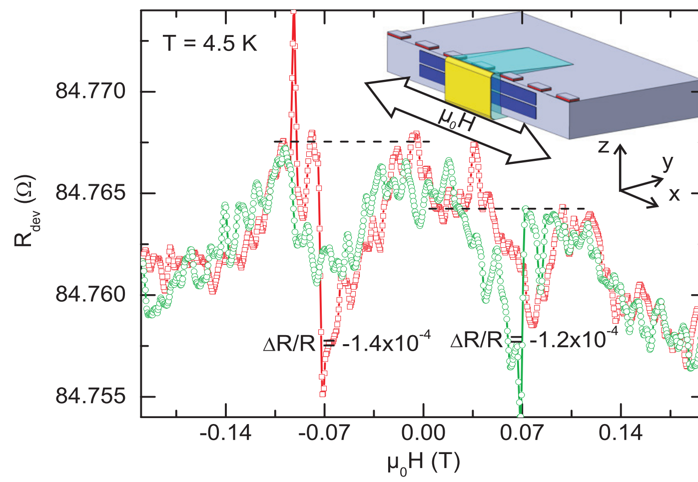

Figure 7.1: Four point MR measurement of the Co/InAs (2DES)/Co hybrid structure. The magnetic field H is applied parallel to the 2DES. The curve with the quadratic (round) symbols shows a section of the down–(up–)sweep from +1 T (−1 T). The abrupt changes of the device resistance are attributed to the magnetization switching of the FM electrodes. The values of $\Delta R/R$ are used in this subsection for an estimation of the spin polarization.

(green curve) show the up–sweep, respectively. Following the down–sweep starting at $\mu_0 H = +200$ mT we observe a first dip at +80 mT. From $\mu_0 H = 0$ mT the curve decreases slowly followed by an abrupt rise at −70 mT. The relative depth of the signature is $\Delta R/R = (R_{high} - R_{low})/R_{high} = -1.4 \times 10^{-4}$. The levels of R_{high} are indicated in figure 7.1 by the dashed horizontal lines. A consistent behavior is observed for the up sweep. Here $\Delta R/R$ is -1.2×10^{-4}.

The following analysis of the measured MR curves allows conclusions about the magnetization M of the Co contacts. The slow decrease of the red (green) curve starting at $H = 0$ for decreasing (increasing) H indicates a multi domain switching of M. We expect this because the dimensions of the FM contacts exceed 0.15 μm. Below this size Co patterns behave as single domains [New96]. The existence of the first dip before reaching zero field can be explained with a so–called hard axis behavior. This is consistent with the results from FMR measurements on unstructured Co films on a cleaved edge presented in chapter 8. We have evidence that M points perpendicular to the plane of the Co film between $\mu_0 H = -40$ mT and +40 mT.

At this point we can not exclude the AMR effect to cause the observed signature. In section 7.2 we demonstrate a gate voltage dependence of the observed signal. The AMR effect does not depend on the gate voltage. Thus, in the following we will interpret the data in the picture of the GMR effect. In this picture the resistance changes coincide with a magnetization switching of the Co contacts.

We compare our result with the calculated GMR effect in chapter 6. For this we evaluate the Fermi energy for the device according to

$$E_F = \frac{\hbar^2 k_F^2}{2m^*} = \frac{\hbar^2 \pi n_{2D}}{m^*} = 24 \text{ meV} \tag{7.1}$$

where $n_{2D} = 3.9 \times 10^{11}$ cm^{-2} from section 7.1.2 and $m^* = 0.039\, m_e$ from [Hu03]. For this E_F we calculated a relative GMR effect of 0.05 (see figure 6.7(b)). The deviation from the measured value is two orders of magnitude. This indicates that the model calculations can not be interpreted quantitatively to discuss our measured data. Reasons are provided in chapter 6.

In the following we compare our result of $\Delta R/R$ with the published values of other authors.

In [Gru01a] we find theoretical predictions for a model of two Fe contacts coupled via a ballistic InAs 2DES. D. Grundler calculates a relative conductance change between parallel and antiparallel magnetization of the Fe contacts to be 3×10^{-3} for $n_{2D} = 5 \times 10^{11}$ cm^{-2} neglecting spin–orbit coupling in the 2DES.

The calculations presented in [Mat02] include spin–orbit interaction and are also based on a Fe/InAs(2DES)/Fe junction. The assumed magnetization direction of the Fe contacts and the 2DES channel length correspond to our experimental configuration. T. Matsuyama et al. obtain a relative conductance change of −0.01 for $n_{2D} = 5 \times 10^{11}$ cm^{-2}.

In the experiment reported in [Hu01b] the dependence of the spin valve effect was measured as a function of the InAs (2DES) channel length. They found a linear increase of the relative effect $\Delta R/R$ for decreasing channel lengths. The minimum channel length was 500 nm with a relative MR effect $\Delta R/R$ of 2×10^{-3}. To compare our data with their result we extrapolate the curve to a channel length of 100 nm. This yields $\Delta R/R = 3 \times 10^{-3}$.

The magnetotransport effects of all three cited authors exceed the value measured in our experiment by an order of magnitude. The theoretical works of D. Grundler and T.

Matsuyama et al. discuss the ideal ballistic case of electron transport through an InAs (2DES) channel as we do in our calculations in chapter 6. They assume atomically flat Fe/InAs (2DES) interfaces and thus neglect effects like impurity scattering or electron–phonon scattering that might occur in a real experiment.

The existence of a GMR signature implies spin transport from the FM source to the FM drain contact. So this experiment proves the injection of a spin polarized current across the Co/InAs (2DES) interface in our hybrid structures.

In the following we estimate the spin diffusion length λ_s in the InAs QW. InAs is a narrow band gap SC, and according to table 2.17, the Elliott–Yafet mechanism spin scattering mechanism dominates. We repeat equation 2.14 that relates the spin scattering time τ_s to the momentum scattering time τ_m

$$\tau_s \approx \frac{\tau_m}{(\Delta g)^2} \ .$$

First we calculate τ_m. Using the electron mobility which is determined in subsection 7.1.2 to be $\mu = 289\,000\ \mathrm{cm}^2/(\mathrm{Vs})$ and $m^* = 0.039\,m_e$ from [Hu03] we obtain $\tau_m = \mu m^*/e = 6.4$ ps. The Landé factor $g = 6$ was measured on samples with the same QW design [Möl03b]. Thus equation 2.14 yields $\tau_s \approx 0.4$ ps. An electron at Fermi velocity

$$v_F = \frac{\hbar k_F}{m^*} = \frac{\hbar\sqrt{2\pi n_{2D}}}{m^*} = 4.7 \times 10^5\ \frac{\mathrm{m}}{\mathrm{s}} \ , \tag{7.2}$$

with $n_{2D} = 3.9 \times 10^{11}\ \mathrm{cm}^{-2}$ from section 7.1.2, travels on average $\lambda_s = v_F \tau_s = 190$ nm between two spin scattering processes. This result indicates that the electrons close to the direct path from source to drain with a distance below 100 nm are not spin scattered. Accordingly, we assume a quasi 1D spin channel. The spin relaxation length was determined experimentally to be ~ 200 nm [Han05] for an InAs nanowire what is in accordance with our data.

With equation 2.26 we estimate the spin polarization η of the current at the FM/2DES interfaces. Assuming ballistic spin transport it reduces to

$$\eta = \sqrt{\frac{1}{2}\frac{\Delta R}{R}} \ .$$

With an average relative resistance change of $\Delta R/R = 1.4 \times 10^{-4}$ we obtain a spin polarization of $\eta \approx 1\,\%$. This order of magnitude is consistent with reported values of 5 %, calculated for an ideal Fe/InAs interface, or $\eta \approx 4.5\,\%$ [Hu01b] measured on a $Ni_{40}Fe_{60}$/InAs (2DES) device.

7.1.2 Signatures of the EMR effect

In figure 7.2 the data of a typical four point measurement of the spin FET device 1146_34 is shown. The configuration displayed in figure 3.10(a) was used to measure the device resistance as a function of the magnetic field H at $T = 4.6$ K. As shown in the inset of figure 7.2, H is oriented perpendicular to the 2DES. The two data sets represent different illumination states of the 2DES. We modulated I_{bias} with an amplitude of 1 μA (rms) and observed the voltage drop across the device V_{dev}. The resistance was calculated using $R_{dev} = V_{dev}/I_{bias}$. The data represented by red squares was measured with no LED illumination. The data represented by the green circles was measured after illumination with a red LED. During the illumination with a current of

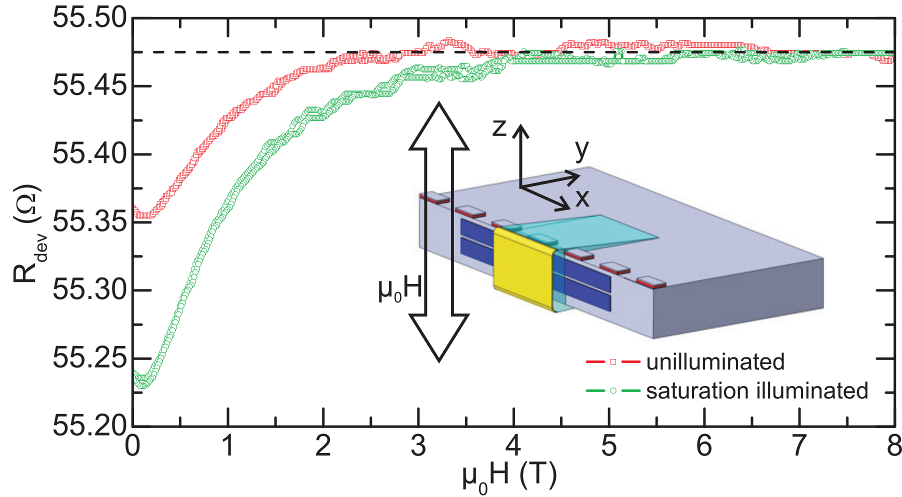

Figure 7.2: Four point magnetoresistance measurement of the Co/InAs (2DES)/Co hybrid structure. The magnetic field $\mu_0 H$ was applied perpendicular to the 2DES. Two illumination states are shown: unilluminated, represented by the squares (red curve) and maximum illumination represented by circles (green curve). From the oscillations we determined the carrier density $n_s = 3.9 \times 10^{11}$ cm^{-2} (unilluminated) and $n_s = 5.1 \times 10^{11}$ cm^{-2} (max. illumination).

200 μA through the LED R_{dev} at $H = 0$ was monitored. R_{dev} decreased from 55.36 Ω to 55.24 Ω.

Starting at $H = 0$ both curves show a resistance minimum at $\mu_0 H = 0.1$ T followed by an increase. The MR saturates around $\mu_0 H = 2$ T. As shown in chapter 2 this characteristics is known from the EMR effect in NM/SC hybrid structures. With magnitudes of $\Delta R/R = R(1\text{ T}) - R(0\text{ T})/R(0\text{ T}) = 0.18$ (red squares) and 0.51 (green circles) the observed effect is small compared with the results of [Möl02] where a maximum value of up to $\Delta R/R = 1150$ was measured. C. H. Möller et al. used a different sample design but the same 2DES heterostructures as presented in this work. In [Hoe06] the authors discuss the dependence of the EMR effect on the ratio W/L, the length to width ratio of the 2DES mesa. We compare the findings in [Hoe06] with our data. The width of our 2DES mesa is 30 μm and the channel length is 100 nm (see section 3.1). We obtain $W/L = 300$. The extrapolation of the data given in [Hoe06] to $W/L = 300$ yields an EMR effect well below 1. This explains our small value for $\Delta R/R$. Our sample design is not optimized for large EMR effects [Hol06]. M. Holz et al. developed a program to simulate EMR devices to predict the MR effect [Hol03a]. In this publication a decrease of the electron mobility μ by 75 % caused an increase of $\Delta R/R$ by 350 %. In our experiment μ decreases by 23 % and $\Delta R/R$ increases by 183 %. The relative change of the EMR effect in our device is in qualitative agreement with [Hol03a].

For $\mu_0 H > 2$ T the curves show oscillations. These oscillations can be interpreted as Shubnikov–de Haas oscillations and based on equation 2.35 we calculate the electron density in the 2DES. We obtain $n_{2D} = 3.9 \times 10^{11}$ cm^{-2} for the unilluminated case and $n_{2D} = 5.1 \times 10^{11}$ cm^{-2} after illumination. The increase of the carrier density is due to the persistent photo effect which is explained in [Wei86]. According to the

theory of the EMR effect we assume that the high resistance value of $R = 55.475\ \Omega$ (dashed line in figure 7.2) is dominated by the SC bulk resistance. Using this resistance value and $W/L = 300$ we calculate the mobility according to equation 2.36. We obtain for the unilluminated (illuminated) case $\mu = 960$ cm^2/(Vs) ($\mu = 735$ cm^2/(Vs)). The uncertainty of these values is very high because the oscillations are not very pronounced and the EMR background makes the interpretation more difficult. The mobility of an unilluminated reference sample from the same wafer at $n_{2D} = 2.85 \times 10^{11}$ cm^{-2} was found to be $\mu = 62\,100$ cm^2/Vs [Möl03a]. We attribute the difference of about two orders of magnitude to an overestimation of our W/L. One might speculate that electrons contributing to the source–drain current, do not flow homogeneously through the 2DES mesa. Assuming $W = 500$ nm, yields $W/L = 5$ and $\mu = 58\,000$ cm^2/Vs what is much closer to the reference value. This result suggests that current close to the cleaved edge dominates the transport properties of our device.

First, our results show clearly that the contacts were well separated during the AFM nanoindenting process. Oscillating behavior would have not been expected if the metallic source and drain contacts were shorted. Second, the values of the carrier density are comparable with measurements on QW structures with the same layer sequence in van der Pauw [vdP58][Möl03a] and Hall bar geometry [Löh03]. The electron density and the mobility was tunable and depended on the illumination dose.

7.2 Magnetotransport with modulated gate voltage

In this section we present the results of measurements with modulated gate voltage V_{gate}^{ac} and a fixed dc bias current of I_{bias}^{dc}. A dc voltage V_{gate}^{dc} between the gate electrode and the FM drain contacting the 2DES was superimposed and the influence of V_{gate} on the 2DES is investigated.

7.2.1 Impact of the gate voltage

The applied voltage V_{gate}^{dc} induces an electric field ε_y^{ext} which acts on the carrier density in the 2DES. To explore this relation we apply an external magnetic field in z direction, i.e. perpendicular to the 2DES. It was swept from $\mu_0 H = 0$ T to 8 T at $T = 4.6$ K. The sweeps were performed for three dc gate voltages. The graphs presented in figure 7.3 show the dynamic device resistance R_{dev}^{dyn} (see equation 3.1) plotted versus the reciprocal magnetic field. The periods of the oscillations are indicated by the equally spaced vertical grid lines. The data is analyzed according to equation 2.35. We summarized the values for the carrier densities n_{2D} in table 7.3.

$\mathbf{V_{gate}^{dc}}$ (V)	$\boldsymbol{n_{2D}}$ (cm^{-2})
-10	4.2×10^{11}
0	4.65×10^{11}
$+10$	5.1×10^{11}

(7.3)

We find a decrease of n_{2D} for negative gate voltages and an increase for positive V_{gate}^{dc}. This behavior is known from conventional MOSFETs and is attributed to the field effect.

A total variation of V_{gate}^{dc} of 20 V changes n_{2D} by 0.9×10^{11} cm^{-2}. Thus, the impact of the gate voltage on the electron density is $\Delta n_{2D}/\Delta V_{gate}^{dc} = 4.5 \times 10^9$ (V cm)$^{-1}$. From this value one can extrapolate that we expect total depletion, i.e. $n_{2D} = 0$, at

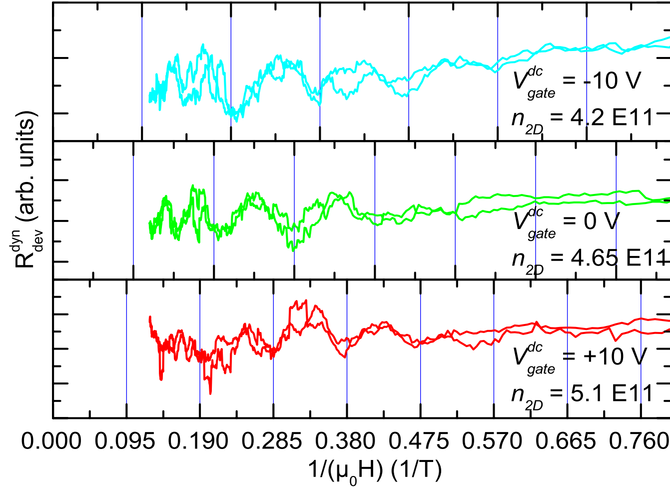

Figure 7.3: The dynamic resistance of a spin FET device is shown as a function of the reciprocal magnetic field. The gate voltage is modulated and a dc voltage of -10 V (top), 0 V (middle) and +10 V (bottom) is applied. The periodicity in $1/(\mu_0 H)$ is indicated by vertical lines. The carrier densities n_{2D} are given in units of cm^{-2}.

$V_{gate}^{dc} = -100$ V. In chapter 5 we derived equation 5.2 that relates the applied gate voltage to the corresponding voltage drop in the 2DES. Using this relation we calculate for $\Delta V_{gate} = 20$ V a voltage variation of $\Delta V_{2DES} = 62$ mV. This voltage drops between the source and the drain contact in the 2DES mesa perpendicular to the cleaved edge within 40 nm.

7.2.2 Angular dependence of oscillating device resistance

The data presented in figure 7.4 show the dynamic device resistance R_{dev}^{dyn} as a function of the dc gate voltage V_{gate}^{dc}. With V_{gate}^{dc} we tune the electric field ε_y^{ext} in y direction, i.e. perpendicular to the cleaved–edge at the position of the 2DES channel. Each curve represents a different angle θ between the externally applied magnetic field H and the 2DES. With θ we adjust the direction of the magnetization $\boldsymbol{M}$ of the FM contacts and therewith the polarization direction $\boldsymbol{S}$ of the injected spins. The data sets are smoothed and the curves are offset in y direction for clarity. The external magnetic field H was set to 1 T. From subsection 7.1.1 we know that the fully magnetized state of the FM contacts is reached for $\mu_0 H > 0.1$ T. At $\theta = 90°$ we observe no characteristic change of the dynamic resistance with the gate voltage. For decreasing angles the signal shows oscillations. These oscillations become more pronounced and the averaged amplitude reaches a maximum of $\Delta R/R_0 = 0.009$ at $\theta = -5°$.

We compare these oscillations of R_{dev}^{dyn} with the predicted behavior of a spin FET as described in section 2.5. In this model, ε_y^{ext} varies the spin–orbit coupling α in such a way that the spin precession angle φ at the drain contact changes by 360° within an oscillation period of R_{dev}^{dyn}.

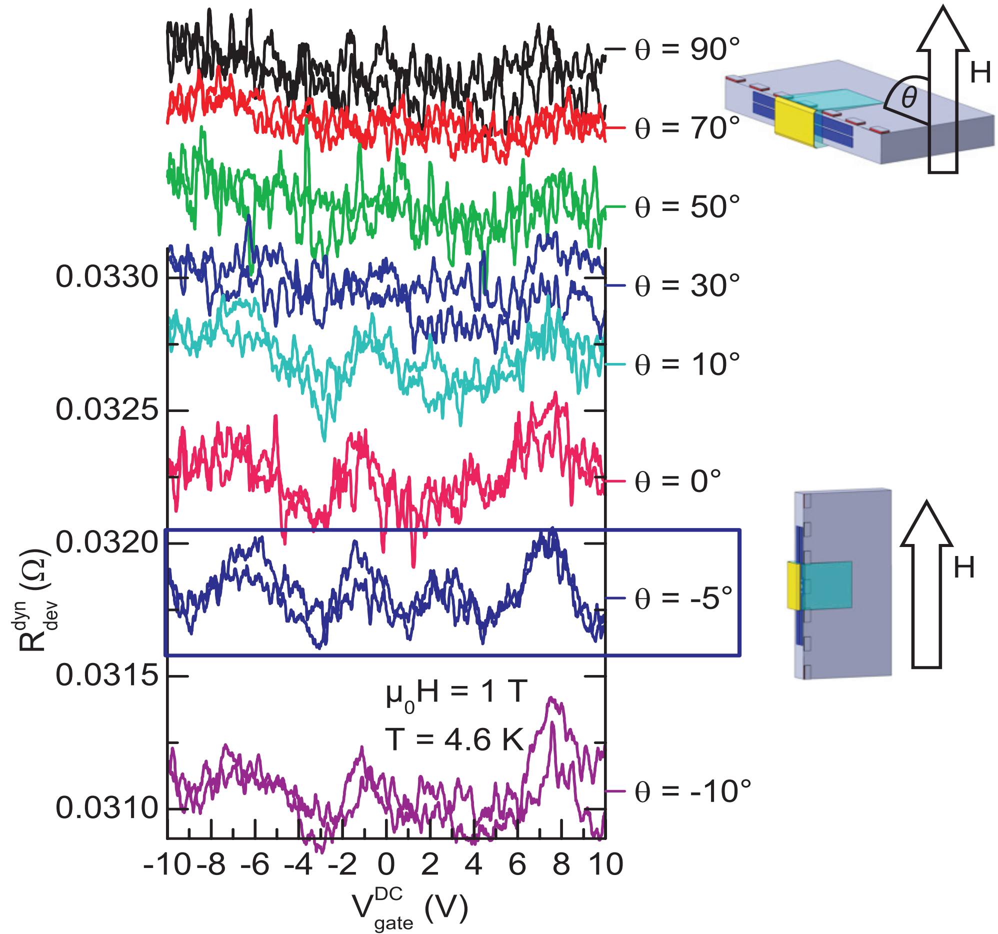

Figure 7.4: Dynamic device resistance as a function of the dc gate voltage for different angles θ between the 2DES and the magnetic field H. $\mu_0 H = 1$ T is applied to saturate the Co contacts in different in–plane directions collinear to H. The curves are equally scaled and shifted in y direction for clarity.

For $\theta = 90°$ $\boldsymbol{M}$ and, correspondingly, $\boldsymbol{S}$ points in z direction. For this orientation the oscillations almost vanish. So we find that the impact of V_{gate}^{dc} on φ depends on the orientation of $\boldsymbol{S}$ and is maximal for $\boldsymbol{S}$ pointing in x direction.

7.2.3 Temperature dependence

We measured the temperature dependence of the oscillations described in the previous subsection. A constant magnetic field of $\mu_0 H = 1$ T at an angle $\theta = 0°$ is applied to magnetize the source and drain contacts. The data is shown in figure 7.5. On the left side we plotted the dynamic device resistance R_{dev}^{dyn} as a function of the gate voltage V_{gate}^{dc}. Each graph represents a different temperature T and includes an up–sweep and a down–sweep of V_{gate}^{dc} to show that the curves are reproducible. All curves are scaled equally, the data is smoothed and offset for clarity. One observes a well defined

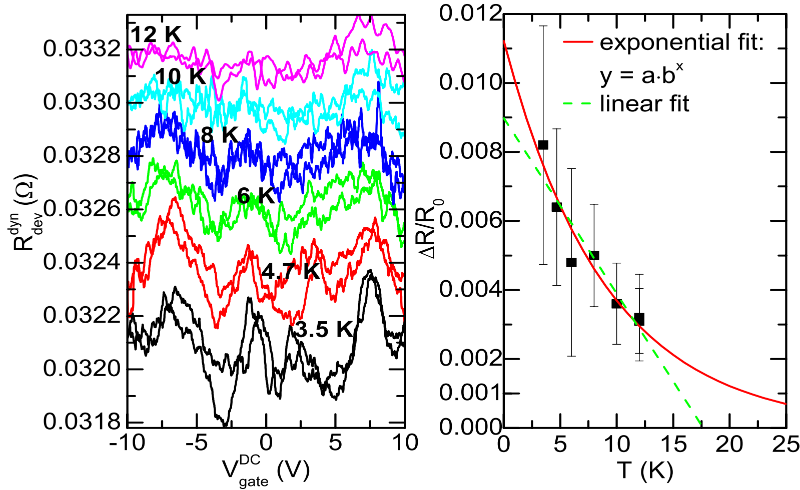

Figure 7.5: Left: Dynamic device resistance as a function of the dc gate voltage for different temperatures. The curves are shifted in y direction but scaled equally. The absolute values of the y scale are not relevant. Right: The average of the oscillation amplitudes is plotted as a function of the temperature. The straight line is a linear fit of the data.

oscillatory behavior of the dynamic resistance at 3.5 K. It decreases in magnitude with increasing temperature. At 6 K the first oscillation vanishes at $V_{gate}^{dc} = +2.5$ V. At 12 K only the most pronounced signatures are still visible.

To analyze the temperature dependence quantitatively we determine the average magnitude of the oscillations for each curve. For that, we determine $(R_{high} - R_{low})/R_{low}$ of each oscillation separately and average over all oscillations of each curve. We obtain the total $\Delta R/R_0$ for the corresponding temperature. The right graph of figure 7.5 shows $\Delta R/R_0$ as a function of temperature. The error bars represent the standard deviation of the averaged oscillation amplitudes. We assume an exponential behavior of the effect height with T in accordance with [Hu01b]. The solid line in the right graph represents a fit of the data using the function $y = a \cdot b^x$. The extrapolation yields

that $\Delta R/R_0$ falls below the noise level of about 0.001 at $T_0 = 21$ K. We further find $\Delta R/R_0 = 0.011$ at $T = 0$ K. Using equation 2.26 we calculate a spin polarization for ballistic electrons at the FM/2DES interfaces of

$$\eta = \sqrt{\frac{1}{2}\frac{\Delta R}{R_0}} = 0.07$$

at $T = 0$. At $T = 4.7$ K we measure $\Delta R/R_0 = 0.0064$ and obtain $\eta = 0.06$. This spin polarization is an order of magnitude higher than the value of $\eta = 0.008$ presented in subsection 7.1.1 for $T = 4.5$ K. We explain the discrepancy with the measurement techniques. In the experiment described in subsection 7.1.1 we modulate the source–drain current. Thus, our signal contains all electrons reaching the drain contact including the non–ballistic ones that take long current paths through the 2DES. These are subject to spin scattering processes and consequently are unpolarized at the drain contact. These electrons produce a voltage offset but do not contribute to the oscillating signature. This is different for the gate modulated measurement configuration. In chapter 5 we found that only a small 2DES area of 100×40 nm^2 between the FM contacts is modulated and that we expect quasi–ballistic spin transport within this area. Accordingly, we detect electrons that are less (spin) scattered what leads to the higher polarization η.

The rapid decrease of a spin valve effect with temperature agrees with experiments by C.–M. Hu et al. in [Hu01b]. In this reference $\Delta R/R_0$ of a FM/InAs (2DES)/FM device decreased from about 2×10^{-3} at $T = 2$ K to 5×10^{-4} at 10 K. They also modulated the bias current, so the same arguments as given above explain the smaller values of $\Delta R/R_0$. But regardless of the measurement technique, the temperatures T_0 where the signatures have vanished are comparable. An extrapolation of C.–M. Hu's data yields that the observed spin effect has vanished at about $T_0 = 16$ K. As explained above, we find $T_0 = 21$ K. Our higher T_0 can be explained by considering the quality of the FM/2DES interfaces: The interfaces in [Hu01b] are treated with a plasma to remove surface oxides at the SC prior to thermal evaporation of the FM contacts. Plasma etching produces rough surfaces. Our interfaces are created in an in situ CEO process and consequently are clean and flat.

7.2.4 Interpretation

In the following we discuss our measured data considering three models. These provide different explanations for an oscillating device resistance as a function of the applied gate voltage.

Model A

The first model we discuss is the Bychkov–Rashba spin–orbit interaction. The mechanism is described in section 2.2. According to this model the spin–orbit coupling is caused by a net electric field ε_z^V from the valence bands arising from structure inversion asymmetry in combination with a voltage bias transverse to the QW. In our case this voltage bias is intrinsic due to the asymmetric doping of the heterostructure (see chapter 3). This mechanism can be tuned by superposing an external field ε^{ext}. But this only affects the spin–orbit coupling if it is applied in growth direction z. On the other hand, in this experiment the external electric field ε_y^{ext} always points in y direc-

tion, parallel to the QW structure. Thus this mechanism can not be the reason for the oscillations in our measured data.

Model B

Now we discuss an effect that could cause a change of φ based on a variation of ε_y^{ext}. It is a spin–orbit coupling of the electron spins with a magnetic field H_R. This field is often called the Rashba field and results from Lorentz transformation of ε_y^{ext} in the inertial system of the moving electron. We use the values calculated in subsection 7.1.1 and assume an electron velocity of $v_x = v_F = 4.65 \times 10^5$ m/s. With the Lorentz transformation

$$-H_z' = \frac{1}{\mu_0} \frac{1}{\sqrt{1 - \frac{v_x^2}{c^2}}} \cdot \frac{v_x}{c^2} \cdot \varepsilon_y^{ext} = H_R$$

and an electric field of $\varepsilon_y^{ext} = 475$ kV/m in the 2DES (from chapter 5) we obtain $\mu_0 H_R = 2.46 \times 10^{-6}$ T. We now assume that this is the only effective magnetic field in $-z$ direction that interacts with the electron spins. For $\theta = 0°$ the spins are polarized in x direction at the source contact. Following equation 2.7 the spins start to precess with the Larmor frequency f_L. The gyromagnetic ratio γ in our InAs heterostructures is $\gamma = \frac{g\mu_B}{\hbar} = 5.28 \times 10^{11}$ (Ts)$^{-1}$. We used the experimentally determined value for the Landé factor $g = 6$ from [Möl03b]. Now, using equation 2.15 we obtain $f_L = 1.30$ MHz. The time for an electron to traverse the 100 nm 2DES channel with Fermi velocity (see equation 7.2) is $t_{2DES} = 0.22$ ps. Within this time and at f_L, the electron spin precesses by $\varphi = 1.03 \times 10^{-4} \cdot 360° = 0.04°$.
We conclude that by this mechanism, the electron spin is not rotated significantly. We find that the influence of the magnetic field that results from Lorentz transformation of the externally applied electric field is negligible. This agrees with the arguments in [Win03].

Model C

In the literature the tuning of the spin–orbit coupling α is mostly accompanied by a variation of the electron density n_{2D}. This suggests that n_{2D} tunes the spin–orbit interaction. It has already been demonstrated that the variation of an applied electric field at constant n_{2D} changes α [Gru00]. Nevertheless it is instructive to compare the influence of the electron density on α in our device with experiments reported in literature.

In subsection 7.2.1 we showed that n_{2D} can be tuned by V_{gate}^{dc} in our device. At $\theta = -5°$ we count 4.25 oscillation periods for the voltage range between $V_{gate}^{dc} = -10$ V and +10 V. This corresponds to a total precession angle of $\Delta\varphi = 1530°$. We use equation 2.8 to calculate the total variation of α for this angle and obtain

$$\Delta\alpha = \frac{\Delta\varphi}{360°} \cdot \frac{\hbar^2}{2m^* L} = 0.42 \text{ eVÅ} .$$

This $\Delta\alpha$ coincides with a variation of n_{2D} by 0.9×10^{11} cm^{-2} (see subsection 7.2.1). Thus we obtain

$$\frac{\Delta\alpha}{\Delta n_{2D}} = 4.7 \times 10^{-26} \text{ eVm}^3 .$$

We compare our result with the experimental data of other research groups. In [Nit97] we find

$$\frac{\Delta\alpha}{\Delta n_{2D}} = \frac{0.3 \times 10^{-11}}{8 \times 10^{15}} \text{ eVm}^3 = 0.04 \times 10^{-26} \text{ eVm}^3 \ .$$

This was measured on an inverted InGaAs/InAlAs QW. Further, from [Eng97] we determine

$$\frac{\Delta\alpha}{\Delta n_{2D}} = \frac{0.9 \times 10^{-11}}{8.8 \times 10^{15}} \text{ eVm}^3 = 0.1 \times 10^{-26} \text{ eVm}^3$$

for an InP/InGaAs/InP QW. We find that our $\Delta\alpha/\Delta n_{2D}$ exceeds these values by more than one order of magnitude. We attribute the difference to the results of J. Nitta et al. and G. Engels et al. to the different QW materials. So not n_{2D} alone, but also the heterostructure design determines α. In accordance with [Win03] we find that the tuning of α is more effective for InAs based QW. Although, this statement in the latter reference is based on the calculated influence of electric fields and not on the influence of n_{2D}.
In [Gru00] the same layer sequence of the InAs heterostructure was used as in our experiments. The electron density was tuned at constant electric field ε^{ext} across the QW by means of a front *and* a back gate electrode. An electron density variation of $\Delta n_{2D} = 3.9 \times 10^{11}$ cm^{-2} causes a change of α by 0.24 eVÅ and we calculate

$$\frac{\Delta\alpha}{\Delta n_{2D}} = 0.61 \times 10^{-26} \text{ eVm}^3 \ .$$

This value of $\Delta\alpha/\Delta n_{2D}$ differs from our result by a factor of about 8 in spite of using the same heterostructure designs. This suggests an additional parameter to govern the spin–orbit coupling. Comparing the device geometries we find that D. Grundler applies ε^{ext} in growth direction of the heterostructure, whereas our electric field points parallel to the 2DES. The direction of ε^{ext} has a stronger influence on α than n_{2D} [Vog07] what is supported by our data.

Model D

None of the previous models explains the observed signal. This gives rise to speculate that an effect other than a variation of the spin–orbit coupling might cause the observed signature. In chapter 6 we found that the variation of the voltage V_y without changing the spin–orbit coupling, leads to an oscillatory behavior of the device resistance. This is due to a quantization in current (x) direction and a variation of the quantization condition in y direction. For example, for positive gate voltages the conduction band edge forms an almost triangular QW at the edge of the device (see figure 5.2). The quantized electron states therein are tunable with V_{gate}^{dc}. A variation of V_{gate}^{dc} leads to an oscillation of the device transmission T_{int} as shown in figure 6.3(c). We can not rule out this effect to cause the observed oscillations of the measured signal. To estimate the impact of this effect, we calculate the number of electron states in a triangular QW as shown in figure 7.6. The energy levels are given by

$$E_j = \left(\frac{\hbar^2}{2m^*}\right)^{1/3} \left(\frac{3\pi e \cdot \varepsilon^{ext}}{2}\left(j + \frac{3}{4}\right)\right)^{2/3} \qquad j = 0, 1, 2 \dots \ .$$

where $m^* = 0.039\, m_e$ (from [Hu03]). To obtain ε^{ext} we first calculate the voltage drop ΔV_{2DES} in the 2DES with equation 5.2. In chapter 5 we found that the voltage

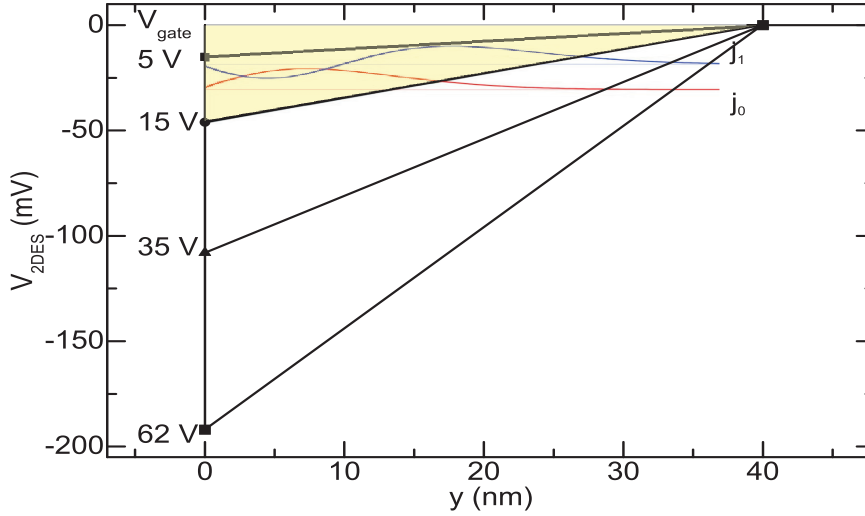

Figure 7.6: Triangular QW at the edge of sample as used for our model calculations. The conduction band edge is shown for 4 different gate voltages. For $V_{gate} = 15$ V the energy levels and the electron wave functions are depicted schematically.

drop in the 2DES occurs within a distance of 40 nm. Thus ε^{ext} is given by $\varepsilon^{ext} = \Delta V_{2DES} / \left(40 \times 10^{-9}\right)$ V/m. In the following table we summarize the energies for the highest bound state, i.e. $e \cdot \Delta V_{2DES} > E_j$ for different gate voltages.

$\boldsymbol{V_{gate}^{dc}}$	ΔV_{2DES}	$\boldsymbol{j}$	E_j
5 V	15 mV	0	12 meV
15 V	46 mV	1	45 meV
35 V	108 mV	2	106 meV
62 V	192 mV	3	191 meV

We find that the number of bound states in the triangular QW increases with V_{gate}^{dc}. In figure 7.4 we observe ~ 2 oscillations between $V_{gate}^{dc} = 0$ V and 10 V for $\theta = -5°$. Within this gate voltage range the calculated number of energy levels in the triangular QW does not change. The first increase of j occurs at $V_{gate}^{dc} = 15$ V. We conclude from the above calculations and the simulations in chapter 6 that this mechanism does explain oscillations of the device resistance but not within the range covered in our experiments. Further this model does not predict an influence of the angle θ between the external magnetic field and the 2DES.

Chapter 8

Hybrid structures under microwave irradiation

In this chapter we present room temperature experiments on an InAs (2DES)/Co/Al hybrid structure that is exposed to rf radiation in the GHz regime[1]. The magnetic field $\boldsymbol{h}_{rf}$ of the microwave excites the spins in the Co film. The preparation of the sample and the experimental setup is described in section 3.2. The following chapter is organized as follows: First, we measure the FMR via the rf voltage inductively picked up by the CPW. Second, in section 8.2, we use the CPW only for spin excitation. We measure the dynamic response of the hybrid structure by means of a dc voltage probed with a LIA across the structure.

8.1 Resonance of the ferromagnetic film

We measure the FMR of the Co layer on the cleaved edge as a function of a magnetic field H_x in x direction. For high H_x the magnetization $\boldsymbol{M}$ of the Co layer saturates and points in x direction. Here, the so–called macrospin behavior can be assumed. Orientations of the equilibrium magnetization $\boldsymbol{M}_0$, H_x and $\boldsymbol{h}_{rf}$ are sketched in the inset of figure 8.1. For such a configuration the rf component transverse to $\boldsymbol{M}_0$ causes a precession of $\boldsymbol{M}$ according to equation 2.18, where $\boldsymbol{H}_{\mathit{eff}}$ includes $\boldsymbol{h}_{rf}$. For each frequency the transmission S_{21} through the CPW is measured. Then the magnetic field is applied in z direction to obtain a reference curve. For this configuration spin precession can not be excited because $\boldsymbol{M}_0$ points parallel to $\boldsymbol{h}_{rf}$. We apply $\mu_0 H_z =$ 130 mT and measure S_{21} again for the same frequency range. This reference data is subtracted from the original transmission curve to filter rf absorptions that are not caused by the FM but by the setup and the CPW. In the following the symbol ΔS_{21} will be used for the transmission if a reference dataset was subtracted. ΔS_{21} is plotted for $\mu_0 H_x = +80$ mT in figure 8.1.

The transmission shows a significant minimum at $f = 8.9$ GHz. This minimum is attributed to the absorption of the microwave if the precession of $\boldsymbol{M}$ is in resonance with the rf frequency. Thus we interpret $f = 8.9$ GHz to be the resonance frequency f_{res} of the FMR of the 20 nm thin Co film on the cleaved edge for $\mu_0 H_x = +80$ mT. We

[1] The experiments were performed together with B. Botters at the Technische Universität München. B. Botters has taken over the rf probe station that has been designed and set–up in the course of my Ph.D. thesis.

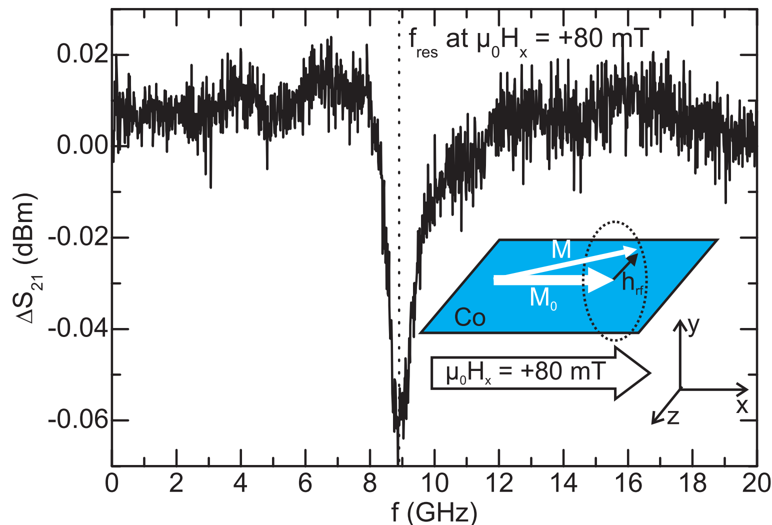

Figure 8.1: Microwave transmission through a CPW with an Al/Co/2DES hybrid structure on top. The sample has a 20 nm thin Co film deposited on the cleaved edge. The film is in the plane of the CPW. The magnetic field is $\mu_0 H_x = +80$ mT. A reference signal was subtracted, ΔS_{21} represents $S_{21}(\mu_0 H_x = 80\text{ mT}) - S_{21}(\mu_0 H_z = 130\text{ mT})$.

exclude a contribution of the InAs 2DES to this signature. In reference experiments on the same InAs heterostructure with no Co deposited on the cleaved edge we observed no characteristic absorption in the ΔS_{21} signal. For the experiment and interpretation we therefore assume in the following that the rf field mainly acts on the FM by means of the torque $\boldsymbol{\tau} = \boldsymbol{M} \times \boldsymbol{h}_{rf}$.

We repeated the above measurement procedure for various H_x starting at $\mu_0 H_x = +130$ mT and decreasing $\mu_0 H_x$ in steps of 2 mT down to -130 mT. The data set is shown as a gray–scale plot in figure 8.2. The dark color represents minima of the transmission, the yellow squares mark selected positions of the FMR for later discussion. The observed curves are symmetric with respect to $\mu_0 H_x = 0$ mT. Starting from positive H_x the resonance frequency decreases with decreasing H_x. In this regime we assume that $\boldsymbol{M}$ is always forced into the direction of H_x. This is denoted by the white arrows in the insets of figure 8.2. The signal shows a significant spin resonance. At $\mu_0 H_x = +30$ mT a minimum of 2 GHz is reached. Between $\mu_0 H_x = +30$ mT and -30 mT we observe no resonances. We suppose that the FMR signal in this magnetic field range is below the signal–to–noise ratio (SNR). To explain this observation, we must assume that $\boldsymbol{M}$ is either collinear with $\boldsymbol{h}_{rf}$ such that $\tau = 0$, or that $\boldsymbol{M}$ is oriented perpendicular to the plane of the Co film (out–of–plane) due to magnetic anisotropy. The latter consideration is stimulated by recent experiments performed by U. Wagner[2] [Wag08]. He measured the FMR of a $Ni_{80}Fe_{20}$ thin film using a CPW. He forced $\boldsymbol{M}$ out–of–plane by means of a field $\mu_0 H$. For this configuration the resonance dip was a factor of 3.6 less pronounced than the absorption for an in–plane magnetization. We will come back to this issue later in this section.

[2] At the Technische Universität München.

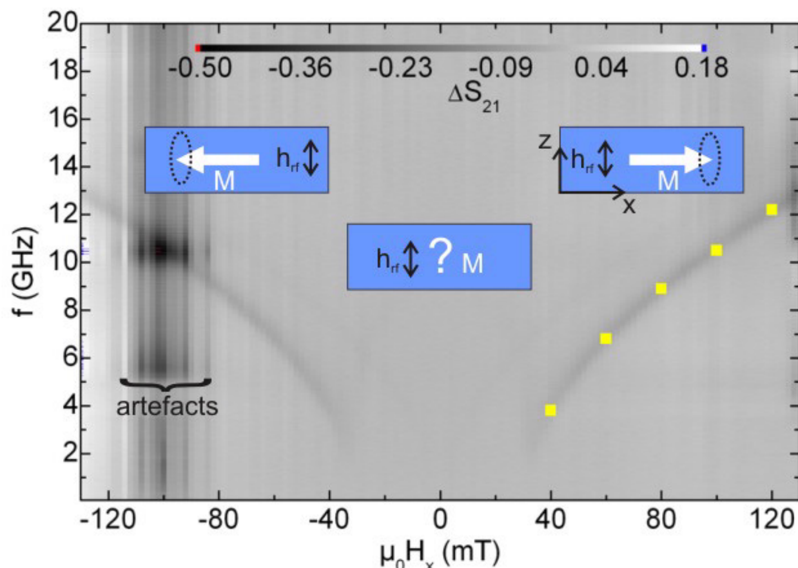

Figure 8.2: Gray-scale plot of absorption spectra taken at successively decreased magnetic field $\mu_0 H_x$ starting from +130 mT. Dark represents strong absorption. The white arrows indicate the magnetization direction of the Co film. Five points of resonant absorption are marked with yellow squares.

8.2 dc voltage detection of magnetic resonances

In the experiment described in this section we modulate the output power of the rf generator with a modulation frequency $f_m = 36$ Hz. We measure the differential voltage $\partial V_{dev}/\partial P_{rf}$ across the device while sweeping the rf frequency f. We repeat this measurement for different magnetic fields from $\mu_0 H_x = +130$ mT to -130 mT in steps of 5 mT. The data is shown in figure 8.3(a). To filter the background signal originating from the experimental setup and the CPW we subtract reference data $\langle \partial V_{dev}(f,\ H_x)/\partial P_{rf} \rangle_{H_x}$ from each spectrum, which is the average of the frequency sweeps of all H_x. When a background is subtracted from raw data, it will be indicated by the symbol Δ. In figure 8.3(b) the device voltage $\Delta V_{dev}(f, H_x) = (\partial V_{dev}(f,\ H_x)/\partial P_{rf}) - \langle \partial V_{dev}(f,\ H_x)/\partial P_{rf} \rangle_{H_x}$ is shown in a gray–scale plot as a function of the rf frequency f and of the magnetic field H_x. Graph (c) shows $\Delta V_{dev}(f, \mu_0 H_x = +80$ mT) along the vertical dashed line at $\mu_0 H_x = +80$ mT. In graph (d) we plotted a section through the gray scale plot at $f = 8$ GHz.

In the gray–scale plot (b) at $\mu_0 H_x = +130$ mT, a voltage peak is seen at $f_{res} = 12.4$ GHz (white signature). With decreasing magnetic field the frequency of this feature decreases and vanishes at $\mu_0 H_x = +30$ mT and $f_{res} = 3$ GHz. For $\mu_0 H_x < +30$ mT the signature changes sign and becomes negative (black trace). Now the frequency increases for decreasing H_x. At negative magnetic fields the behavior is symmetric with respect to $H = 0$. If compared with figure 8.2 we find that the white branch reproduces the field–dependence of the FMR of the Co film. Interestingly, between -30 mT and $+30$ mT we observe a pronounced signature in the voltage drop ΔV_{dev} across the device. In this regime the FMR measurement via the CPW did not provide a signal. The dc detection thus goes beyond the inductive FMR measurement presented

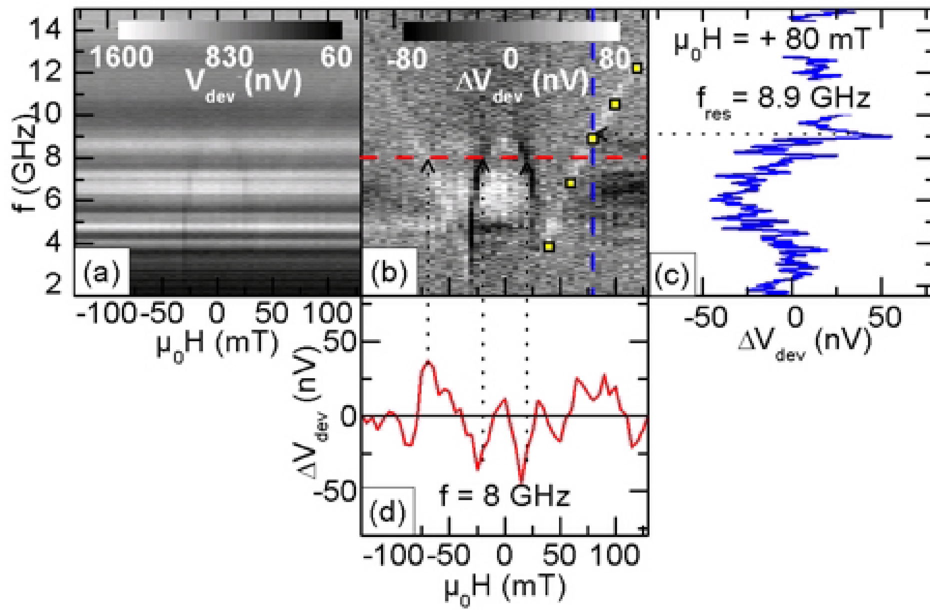

Figure 8.3: (a) Raw signal of the device voltage as a function of the rf frequency and of the magnetic field. (b) Device voltage ΔV_{dev}. Reference data is subtracted from the raw data in (a) (explained in the text). The resonant signatures appear at the same positions as the FMR. Five resonance positions from figure 8.2 are indicated by the yellow squares. (c) Cross section through the gray–scale plot at $\mu_0 H_x = 80$ mT. (d) Cross section through the gray–scale plot at $f = 8$ GHz. Dottet arrows indicate the position of the voltage extrema.

in figure 8.2. Furthermore, we observe a striking change in sign of the voltage signal. This will be discussed in more detail in the following.

For $|\mu_0 H_x| < 30$ mT the signal contrast is as large as for $|\mu_0 H_x| > 30$ mT. From this we conclude that $\boldsymbol{\tau} \neq 0$ in both field regimes. This suggests that the magnetic easy axis of the Co film points in y direction (out–of–plane). This statement is supported by the following three arguments:
(i.) In [Dre99] it was reported that C impurities in a Co film caused an out–of–plane magnetic anisotropy. This occurs for Co film thicknesses up to at least 18 monolayers. We have indication of a C contamination of the vacuum chamber in which the Co film was deposited.
(ii.) In [Gil05] a 188 nm thick Co film exhibited an out–of–plane component of $\boldsymbol{M}$ in its demagnetized and remanent states. This was measured by means of magnetic force microscopy. W. Gil et al. related this behavior to a crystalline anisotropy. They supposed a hcp texture in their polycrystalline Co film with the hexagonal axis pointing normal to the plane. An out–of–plane anisotropy of our polycrystalline Co film might occur, if the deposition of the nanoscopic Co crystals is not fully random but textured.
(iii.) If a magnetic anisotropy was present, the minimum frequency of the FMR signal depends on the angle between H_x and the magnetic hard axis [Lin03]. B. Botters et al. show [Bot06b] that lowest resonance frequencies are observed if H is aligned parallel to the hard axis. A small misalignment of 2° between H and the hard axis causes an increase of the minimum f_{res} from 0.5 GHz to 2 GHz, i.e. the initially sharp minimum in the $f_{res}(H_x)$ curve is smoothed. Reversely spoken, the easy axis must point perpendicular to H_x to observe minimal f_{res}. In our data (figure 8.3(b)) a strikingly sharp minimum is observed, indicating a misalignment below 2°. Assuming that our easy axis is oriented perpendicular to the plane of the Co film (out–of–plane), such a good alignment is self–adjusted by placing the sample on the CPW with the Co film on the cleaved–edge face down.

Now we compare in detail f and H_x of the extrema in the gray–scale plot with the positions of the FMR in figure 8.2. Exemplarily we take the $\Delta V_{dev}(f)$ curve for $\mu_0 H_x = +80$ mT shown in figure 8.3(c). We find a voltage peak at $f_{res} = 8.9$ GHz which is the same frequency as the absorption of the microwave in figure 8.1. Further the data points represented by the yellow squares in (b) are copied from those in figure 8.2. The extrema in the voltage curves occur at the same f_{res} and H_x where the resonance condition for spin precession in the FM is fulfilled.

Exclusion of diode–like behavior

In the following we discuss the possibility that the measured signal results from rectification of an induced rf current as a consequence of a diode–like transport behavior of the hybrid device. First, this requires a nonlinearity of the I V curve. We measured the voltage as a function of a dc bias current I_{dc}. No nonlinear behavior was found. Further, we observed the rf induced voltage at different bias currents. This is shown in subsection 8.2.1. So even if a nonlinearity around $I_{dc} = 0$ was present, which was too small to be resolved, we should not measure the signature at dc currents $I_{dc} \neq 0$. Second, in case of a rf rectification effect, the observed voltage signature should be correlated with the transmission characteristics of the CPW (shown as ΔS_{21} in section 8.1). Figure 8.4 shows the raw data of the transmission S_{21} at $\mu_0 H_x = +80$ mT. The dashed line labeled with (c) indicates the position of the FMR at $\mu_0 H_x = +80$ mT. The

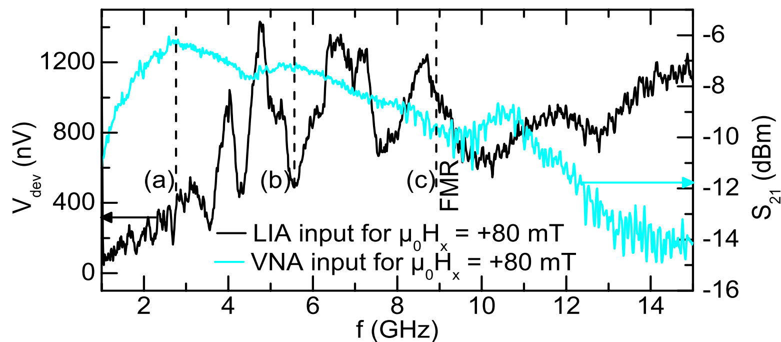

Figure 8.4: Raw signals of the voltage drop across the device measured with the LIA (dark curve, left scale) and of the transmitted rf power measured with the VNA (bright curve, right scale). The transmission characteristics of the CPW is not correlated with the measured voltage. The dashed line (c) denotes f_{res} of the FMR. Lines (a) and (b) are discussed in the text.

absorption due to FMR is small if compared with the total variation of rf power across the whole frequency range. The variation of up to 8 dBm is attributed to resonances in the measurement setup and losses in the CPW.
The left axis refers to the data of the raw LIA input signal V_{dev} for $\mu_0 H_x = +80$ mT. We focus on the frequencies at the dashed lines labeled with (a) and (b). At (a) the transmitted rf power exhibits a broad maximum. V_{dev} does not reflect such a significant maximum at this frequency. At (b) V_{dev} shows a significant dip, whereas the CPW's transmission varies smoothly. We conclude that the signals are uncorrelated and thus we can exclude rectification through diode characteristics to cause the signatures in ΔV_{dev} at the FMR frequency.

8.2.1 Microwave induced dc voltage: Dependence on modulation frequency, bias current, illumination and rf power

In figure 8.5 we present the influence of the lock–in modulation frequency (b), the magnetic field direction (c), the y position of the sample (d), the illumination state (e) and the rf power (f). The data obtained at small modulation frequency $f_m = 36$ Hz are depicted in (a) and serve as the reference dataset. In the following each column shows the device voltage ΔV_{dev} as a function of frequency and magnetic field in a gray–scale plot. We extracted frequency sweeps along the vertical lines through the gray–scale plots at $\mu_0 H_x = +80$ mT and -80 mT. These are plotted in the graphs below. The dotted lines indicate the resonance frequency observed in (a).

The lock–in modulation frequency f_m influences the contrast of the voltage extrema. The contrast in (a) is low. Figure 8.5(b) shows measurements at $f_m = 96$ kHz that exhibit more pronounced signals. We calculated the mean value of the absolute values of ΔV_{dev} at the maxima for 12 different magnetic fields from +100 mT to +50 mT and from -50 mT to -100 mT in steps of 10 mT. For the data shown in (b) we obtain $\langle|\Delta V_{dev}|\rangle_{\max} = 111$ nV. The angle bracket indicates the mean value of the voltage maxima.

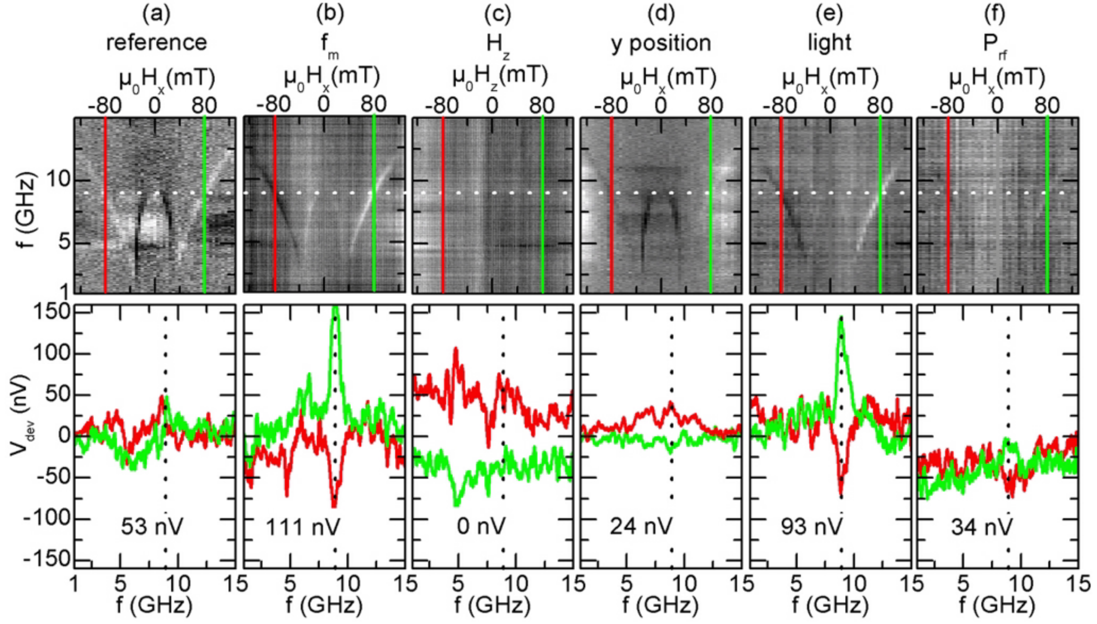

Figure 8.5: The gray–scale plots show the device voltage ΔV_{dev} as a function of frequency and magnetic field. Each plot represents a different parameter set. The lower panels show corresponding frequency sweeps $\mu_0 H_x = \pm 80$ mT. The values in units of nV represent the mean value of the absolute voltages at the position of the maxima $\langle|\Delta V_{dev}|\rangle_{\mathrm{max}}$ for each dataset. The following table provides the experimental conditions for each measurement.

param	**(a)**	**(b)**	**(c)**	**(d)**	**(e)**	**(f)**
$\boldsymbol{f}_m$	36 Hz	96 Hz	96 Hz	96 Hz	96 Hz	96 Hz
dir of $\boldsymbol{H}$	x	x	z	x	x	x
$\boldsymbol{y}$ pos	on CPW	on CPW	on CPW	50 μm	on CPW	on CPW
illumin	dark	dark	dark	dark	light on	light on
$\boldsymbol{P}_{rf}$	8 dBm	8 dBm	8 dBm	12 dBm	8 dBm	4 dBm

Further, f_m determines the symmetry of the signature. The reference signature in (a), measured at $f_m = 36$ Hz, is symmetric with respect to $H_x = 0$. This is not the case for (b), where the signature is positive for $\mu_0 H_x > +30$ mT and negative for $\mu_0 H_x < -30$ mT. We will discuss this in more detail later in this section.

The data shown in (c) were measured with $\boldsymbol{H}$ pointing along z direction. We find no field dependent resonant behavior in the gray–scale plot. In this configuration the magnetization points collinear to the rf magnetic field $\boldsymbol{h}_{rf}$ in the CPW and thus no precession can be excited. This confirms that the dc voltage signal is directly related to the resonant precession of the magnetization.

To rule out any direct electrical contact and possible current flow between the sample and the CPW we lifted the sample 50 μm in vertical direction. In this configuration a "vacuum" gap is guaranteed between the Co layer and the CPW. With an increased rf power P_{rf} of 12 dBm and at $f_m = 96$ kHz the signature is still observable as shown in figure 8.5(d). At the distance $y = 50$ μm above the CPW and for $P_{rf} = 12$ dBm we calculate the amplitude of the z component of $\boldsymbol{h}_{rf}$ based on the simulations presented in section 3.2 and equation 3.2. We obtain $\mu_0 h_{rf} \approx 15$ μT, what is a factor of 4.5 smaller than the value calculated for $y = 1$ μm and $P_{rf} = 8$ dBm. We compare the $\langle|\Delta V_{dev}|\rangle_{\max}$ of this signal with the value shown in (b) as the same $f_m = 96$ kHz were used. We find a decrease of the average voltage maximum by a factor of 4.6 from 111 nV to 24 nV. This indicates that ΔV_{dev} scales linearly with $\boldsymbol{h}_{rf}$.

So far all presented data was measured in the dark. Figure 8.5(e) shows a measurement with white light illuminating the sample. This reduces the resistance of the SC, but in contrast to low temperature experiments this photo effect is transient at room temperature. For $\langle|\Delta V_{dev}|\rangle_{\max}$ we calculate 93 nV. The comparison with the result from (b), where the same modulation frequency was used, yields a reduction of 16 % for the averaged magnitude for the illuminated device.

In column (f) in figure 8.5 a measurement with the rf power reduced by a factor of 2 to $P_{rf} = 4$ dBm. Using equation 3.2 we calculate a reduction of the current in the CPW from $I_{rf} = 355$ mA to $I_{rf} = 224$ mA. The mean magnitude of ΔV_{dev} reduces to $\langle|\Delta V_{dev}|\rangle_{\max} = 34$ nV. If compared with (b) this is a reduction by a factor of 3.3. In [Cos06a] a linear dependence of the resonant voltage signal on the square of the rf current in the CPW is reported. This is in qualitative accordance with our data if $\langle|\Delta V_{dev}|\rangle_{\max} = 0$ for $I_{rf} = 0$ is assumed. Quantitatively the slopes differ by ~ 25 % what might be explained with the different materials used for the hybrid structures. This issue will be discussed in more detail later in this chapter.

Modulation frequency dependence

We return to the dependence of the signature on the modulation frequency f_m of the rf amplitude. In figure 8.6 (left) ΔV_{dev} is plotted as a function of f_m and the rf frequency f. The magnetic field was fixed to $\mu_0 H_x = +80$ mT and the rf power $P_{rf} = 12$ dBm, with $\mu_0 h_{rf} = 0.1$ mT at the position of the Co layer. $f_{res} = 8.9$ GHz is indicated by the horizontal line in the gray–scale plot. We subtracted the frequency response measured at zero magnetic field. A signature always occurs at the same rf frequency $f_{res} = 8.9$ GHz. The sign depends on f_m. The right graph in figure 8.6 shows ΔV_{dev} as a function of f_m at the resonance frequency. At $f_m = 10$ kHz, 28 kHz and 57 kHz the device voltage is zero. The highest absolute value is found for high modulation frequencies. We attribute the change of sign to a phaseshift between the amplitude

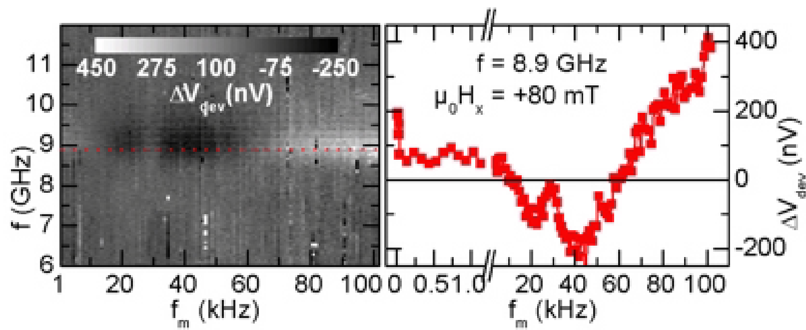

Figure 8.6: Left: Gray–scale plot of the device voltage as a function of the microwave frequency and the modulation frequency. $\mu_0 H_x = +80$ mT. The FMR frequency is indicated by the horizontal line. Right: Cross section at FMR frequency. Depending on f_m positive and negative voltage maxima are observed. Note that the scales before and after the brake of the f_m axis are different.

modulation of the microwave and the lock–in output frequency. This is probably caused by a frequency dependent time delay (phase shift) in the rf generator while processing the voltage at the amplitude modulation input. As this is of technical origin and not physical, we consider the dataset at low f_m as original. We find that for frequencies below 28 kHz no further sign changes occur. As shown in figure 8.5(a) this signal is symmetric with respect to $H_x = 0$ whereas at higher f_m (figure 8.5(b)) the signature is positive for $\mu_0 H_x > +30$ mT and negative for $\mu_0 H_x < -30$ mT. This asymmetry suggests a complex magnetic field dependence of the phase shift. This is interesting in itself but will not be discussed further in this work.

Current dependence

We studied the effect of a dc current I_{dc} on the observed effect. We applied 1 μA to the InAs (2DES)/Co/Al junction and measured the voltage as a function of the rf frequency and H_x. The signal ΔV_{dev} is shown as a gray–scale plot in figure 8.7. The parameters of the measurement are $P_{rf} = 12$ dBm, $f_m = 43$ kHz and the sample was unilluminated. Prior to each setting of the magnetic field H_x, the magnetization of the Co layer was saturated by sweeping H_x to +130 mT. The curves at $\mu_0 H_x = \pm 80$ mT are compared with a reference measurement with equal parameters but no dc current. Both curves have their extrema of ΔV_{dev} at $f_{res} = 8.9$ GHz, the FMR frequency of the Co film. The average of the absolute values of the voltage amplitudes is $\langle|\Delta V_{dev}|\rangle_{\max} = 813$ nV with $I_{dc} = 1$ μA. It exceeds the magnitude of the data with $I_{dc} = 0$ by a factor of 4.5.

8.2.2 Interpretation

We now further interpret our results. In particular, we compare our data with three models that provide different explanations for the occurrence of a voltage signal.

Model A: Induced voltage by the spin battery effect

We evaluate the model described in section 2.2.4 for our device. According to this theory a dc voltage is generated across a FM/NM interface by the spin pumping mechanism.

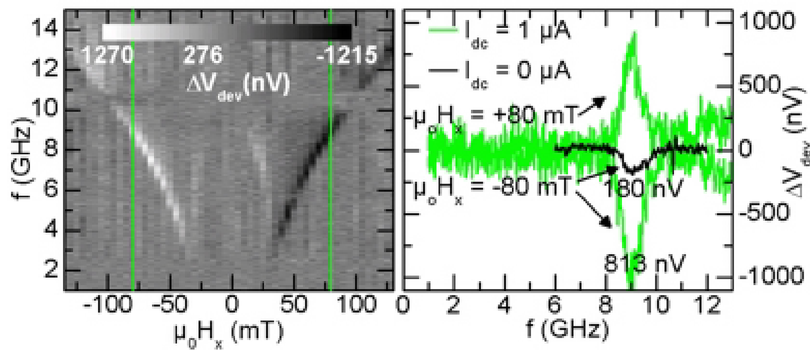

Figure 8.7: The gray–scale plot shows the device voltage as a function of the magnetic field and of the frequency. A dc current of 1 μA was applied across the InAs (2DES)/Co/Al junction. Significant peaks (dips) occur at the positions of the FMR. In the right picture we compare the data with a measurement at $I_{dc} = 0$. For both datasets f_m was 43 kHz. The average magnitude of the voltage extrema of the current biased experiment exceeds the reference data by a factor of 4.5.

For this, a precessing $\boldsymbol{M}$ is needed that, in our case, is caused by the rf magnetic field $\boldsymbol{h}_{rf}$. The relevant equations are 2.22 and 2.23. Using both we find

$$V_{dc} = \frac{\Delta\mu_0}{e} \simeq \frac{p_\omega}{2e}\hbar\omega \frac{g_\omega^{\uparrow\downarrow}}{\left(1+\frac{g_{NM}}{g_{FM}}\right)(1-p_\omega^2)\left(g_\omega^{\uparrow}+g_\omega^{\downarrow}\right)+2g_{NM}}\theta^2 \ . \tag{8.1}$$

Our device incorporates two interfaces. Thus, the measured voltage is the difference ΔV_{dc} of the voltage drops occurring at the Co/Al and at the Co/2DES interface. The effective conductances $g_\omega^{\uparrow(\downarrow)}$ and $g_\omega^{\uparrow\downarrow}$are calculated using the equations 2.20

$$g_\omega^{\uparrow(\downarrow)} = \frac{g^{\uparrow(\downarrow)}}{1+g^{\uparrow(\downarrow)}/g_\omega} \text{ and } g_\omega^{\uparrow\downarrow} = \frac{g^{\uparrow\downarrow}}{1+g^{\uparrow\downarrow}/g_\omega} \ .$$

These represent the spin dependent conductances in series with the bulk NM conductances evaluated over the spin averaging length l_ω using $g_\omega = \sigma_{NM}A/l_\omega$. The conductance $g_{NM\ (FM)} = \sigma_{NM\ (FM)}A_{NM\ (FM)}/l_{NM\ (FM)}$ in equation 8.1 refers to the bulk value of the NM (FM).

We evaluate the two interfaces separately.

The Co/Al interface The Co/Al interface area of our device is $A_{Co/Al} = 2\,000 \cdot 0.02\ \mu\text{m}^2$. For the Al film we use the material constants for room temperature (RT) of a surface–oxidized 50 nm thin film published in [Jed02]. We find $\sigma_{Al} = 1.1 \times 10^7\ (\Omega\text{m})^{-1}$, $\lambda_{sf}^{Al} = 350 \pm 50$ nm and for the diffusion constant $D_{Al} = 2.7 \times 10^{-3}\ \text{m}^2\text{s}^{-1}$. From D_{Al} we obtain [Wan06] $l_\omega = \sqrt{D_{Al}/\omega} = 220$ nm at a resonance frequency of 8.9 GHz at $\mu_0 H = 80$ mT. As $l_\omega < \lambda_{sf}^{Al}$ the time dependent components of the spin accumulation in the Al are zero in time average. With these values we calculate the conductance $g_\omega = \sigma_{Al}A_{Co/Al}/l_\omega = 2\,000\ \Omega^{-1}$. In order to determine the spin dependent conductances $g^{\uparrow(\downarrow)}$ we use the spin polarization in Co of 42 % [Sou98] and $\sigma_{Co} = 6.7 \times 10^6\ (\Omega\text{m})^{-1}$ [But96]. We find $\sigma^{\uparrow} = 4.8 \times 10^6\ (\Omega\text{m})^{-1}$ and $\sigma^{\downarrow} = 1.9 \times 10^6\ (\Omega\text{m})^{-1}$. The length

of the Co film is $l_{Co} = 50$ nm. Now we calculate the interface conductances $g^{\uparrow} = \sigma^{\uparrow} A_{Co/Al}/l_{\mathrm{Co}} = 3\,840\ \Omega^{-1}$ and analogously $g^{\downarrow} = 1\,520\ \Omega^{-1}$. With equations 2.20 we obtain the effective interface conductances $g_{\omega}^{\uparrow} = 1320\ \Omega^{-1}$ and $g_{\omega}^{\downarrow} = 864\ \Omega^{-1}$.

For the effective interface polarization we calculate $p_{Co/Al} = \left(g_{\omega}^{\uparrow} - g_{\omega}^{\downarrow}\right) / \left(g_{\omega}^{\uparrow} + g_{\omega}^{\downarrow}\right)$ $= 0.21$. We assume diffusive transport and thus, according to [Bra00], $g_{Co/Al}^{\uparrow\downarrow}$ is dominated by the conductance of the NM. The relevant length scale for the mixing conductance is the spin–flip length of Co, which is $\lambda_{sf}^{Co} \sim 100$ nm [Chi97]. For this we find $g_{Co/Al}^{\uparrow\downarrow} = \sigma_{Al} A_{Co/Al}/\lambda_{sf}^{Co} = 4\,400\ \Omega^{-1}$ and for the effective mixing conductance $g_{\omega}^{\uparrow\downarrow} = 1\,375\ \Omega^{-1}$.
The conductance $g_{Al} = \sigma_{Al} A_{Al}/l_{Al}$ for the Al contact with a cross section of $A_{Al} = A_{Co/Al}$ and $l_{Al} = 2$ mm yields $0.22\ \Omega^{-1}$. The same calculation for the Co film with the same cross section and $l_{Co} = 50$ nm yields $g_{Co} = 5\,360\ \Omega^{-1}$.
We estimate the the precession cone angle: We use the simulations of $\boldsymbol{h}_{rf}$ from section 3.2 and equation 3.2. For $P_{rf} = 8$ dBm and a distance between the CPW and the Co film of 1 μm we obtain $\mu_0 h_{rf} = 68\ \mu$T for the in–plane (z) component. $\boldsymbol{h}_{rf}$ and a static magnetic field of $\mu_0 H = 80$ mT collinear to the CPW are used as input parameters for a simulation[3] of the magnetization $\boldsymbol{M}$ in the Co film with the *MicroMagus* software[4]. From $\boldsymbol{M}$ we extract the in–plane precession angle of $\theta = 0.012°$. Note, that the out–of–plane precession angle is an order of magnitude smaller. This is due to the smaller out–of–plane magnitude of $\boldsymbol{h}_{rf}$ and to the shape anisotropy of the Co film. In the following we consider the in–plane precession angle only.

Using the above input parameters in equation 8.1 we calculate $V_{dc}^{Co/Al} = 1 \times 10^{-13}$ V for $f = 8.9$ GHz.

The Co/2DES interface For the voltage across the Co/2DES interface we use the same approach as for the Co/Al interface. The interface area is $A_{Co/2DES} = 4\,000 \cdot 0.004\ \mu\mathrm{m}^2$. The room temperature material parameters for the InAs heterostructure are taken from [Kro03]. We find for the electron density $n_{2DES} = 3.5 \times 10^{15}\ \mathrm{m}^{-2}$ and for the mobility $\mu_{2DES} = 2.1\ \mathrm{m}^2(\mathrm{Vs})^{-1}$. Using the Einstein relation at $T = 300$ K we obtain $D_{2DES} = e\mu_{2DES}/\left(k_B T\right) = 81\ \mathrm{m}^2\mathrm{s}^{-1}$ and $l_{\omega} = \sqrt{D_{2DES}/\omega} = 38\ \mu$m (for $f = 8.9$ GHz). This length scale over which the averaging of the transverse components of the spin precession occurs is large in the 2DES compared with the Al.
We estimate the spin flip length λ_{sf}^{2DES} at room temperature. The D'yakonov–Perel' spin scattering mechanism dominates (see table 2.17). Thus, we use equations 2.6 and 2.16 with a spin splitting of $\Delta E_{eff} \approx 10$ meV [Gru00] and a momentum scattering time of $\tau_m = \mu_{2DES} m^*/e = 0.5$ ps, where $m^* = 0.039\, m_e$ [Hu03]. This yields the spin scattering time

$$\tau_s = \left(\frac{\hbar}{\Delta E_{eff}}\right)^2 \frac{1}{\tau_m} = 9 \text{ fs} .$$

With the Fermi velocity given in equation 7.2 we estimate $\lambda_{sf}^{2DES} \approx 4$ nm. At this point we note that $l_{\omega} \ll \lambda_{sf}^{2DES}$ is not given but required within this model [Wan06]. The spins are scattered before the completion of a full precession cycle. Consequently the model developed by X. Wang et al. is not applicable for this interface. Thus, in the

[3] The simulations were performed by S. Neusser at the Technische Universität München.
[4] www.micromagus.de

following we consider the InAs (2DES) as a perfect "spin sink" (see subsection 2.2.4) with zero voltage drop $V_{dc}^{Co/2DES}$ across the Co/2DES interface.

Then, the calculated voltage drop across the hybrid device is

$$\Delta V_{dc} = V_{dc}^{Co/Al} - V_{dc}^{Co/2DES} = 1 \times 10^{-13} \text{ V} ,$$

whereas the measured voltages are of the order of tens of nanovolts. The discrepancy of the calculated value from the measured value might arise from the fact that λ_{sf}^{Co} exceeds the length of the Co film between the Al and the 2DES interface. As a consequence, the μ_s^{Co} at both interfaces are mixtures of the spin accumulations in the Al and the 2DES which interact via the backflow currents [Wan06]. Further we point out that the model is a one–dimensional approach which does not take into account the 3D device geometry.

In the following we discuss the prediction of the present model concerning the sign change we measured at $\mu_0 H_x = \pm 30$ mT. The voltage drop depends on the spin dependent conductivities in the FM, on the bulk conductivities of the involved materials and on the interface mixing conductances. None of these parameters is expected to exhibit a magnetic field dependence that would explain a sign change of the voltage signal. Further, it depends on the precession frequency and on the cone angle. These parameters might produce a sign change of ΔV_{dc}. But such a mechanism was not predicted so far.

We argued that the sign change coincides with a rotation of $\boldsymbol{M}$ of the Co film from the in–plane x direction to the out–of–plane y direction for $|\mu_0 H_x| < 30$ mT. Then, the spin accumulations in the NMs are also polarized in y direction. In the presence of small but nonzero H_x such a spin accumulation would dephase due to the Hanle effect. As this effect occurs in both NMs simultaneously, a reduction of the voltage drop could be explained, but not a change of sign.

Model B: AMR

Now we discuss the AMR effect (see section 2.3.1) to be the origin of the observed voltage signature. For this explanation we must assume a dc current $\boldsymbol{I}_{dc}$ flowing in z direction between the InAs (2DES) and the Al contact (device geometry: see subsection 3.2.1). A dc current might occur due to photocurrents induced by unavoidable light sources in the laboratory (e.g. displays, LEDs) or due to thermal voltages (Seebeck effect).

According to equation 2.27 the AMR depends on the angle θ between $\boldsymbol{M}$ and $\boldsymbol{I}_{dc}$. At high $|\mu_0 H_x|$ the magnetization is perpendicular to $\boldsymbol{I}_{dc}$. We expect a minimal resistance, as $\theta = 90°$. At resonance frequency, the precession cone angle of $\boldsymbol{M}$ increases. Accordingly, $\theta < 90°$ and the resistance increases. This could explain the increase of the voltage drop at resonance frequency in figure 8.5(a).

The increase of the averaged signature amplitude under illumination (figure 8.5(e)) supports this model. Based on this observation we exclude thermal voltages to generate the dc current and focus on the photovoltaic effect. First, we estimate the magnitude of the current that is needed to cause the observed signature. For this, we compare the experiments with and without externally applied I_{dc}. This is shown in figure 8.7. We find that an externally applied $I_{dc} = 1$ μA produces $\langle|\Delta V_{dev}|\rangle_{\max} = 813$ nV. In a linear approximation and under the assumption that $\langle|\Delta V_{dev}|\rangle_{\max} = 0$ for $I_{dc} = 0$ we estimate that in order to measure a device voltage of 180 nV a current $I_{dc} = 0.2$ μA

must flow. But $\langle|\Delta V_{dev}|\rangle_{\max} = 180$ nV is observed without applying an external current (see figure 8.7). Hence, within this model, a dc current of 0.2 μA must be induced by a photocurrent. A photocurrent arises from electron–hole pairs which are generated by photons and do not recombine. In photodiodes the recombination is prevented in the inversion layer of the p–n junction. A Schottky diode could also separate electrons and holes. The SC of our device does not exhibit areas of different doping as Si is the only donor material. Further we use an InAs 2DES which does not form Schottky barriers at the interfaces. Thus, due to the lack of a separation mechanism for generated electron–hole pairs we conclude that the generation of a photocurrent of 0.2 μA is unlikely for our device.

Now we discuss the sign change of the voltage signature within this model. At $|\mu_0 H_x| < 30$ mT the magnetization $\boldsymbol{M}$ presumably rotates out–of–plane. This leaves θ unchanged at 90° as the rotation axis is collinear to the current flow in z direction. In this configuration this model also predicts a voltage increase at FMR frequency. This contradicts our data, where a voltage decrease is observed in this magnetic field regime.

We conclude that this model is not appropriate to explain our data. First, the required dc photocurrent can not be generated and second, the sign change can not be explained.

Model C: Induced rf current and dynamic Hall resistance

Unlike in model B, in the experiment published by the group of C.–M. Hu [Gui07] the observed signal changes sign as a function of $\boldsymbol{H}$. This motivated the consideration of their model for the discussion of our data. The calculations outlined here were done in collaboration with N. Mecking[5]. In [Mec07] N. Mecking et al. explain how the interaction of an induced rf current density $\boldsymbol{j}$ and a dynamic AMR effect leads to a dc voltage drop in rf current direction. A summary is provided in subsection 2.4. With our device configuration we measure the voltage component *perpendicular* to $\boldsymbol{j}$. In the following we generalize their model and adapt it to our experimental conditions. For this, we include the relevant MR effects presented in section 2.3.2, i.e. the AHE and the IPHE.

In the following two coordinate systems (CS) are used. They are illustrated in white and in black color in figure 8.8. LCS (black) is the laboratory CS which is defined by the orientation of the sample such that z represents the growth direction of the heterostructure. In accordance with [Mec07] we assume that $\boldsymbol{j}$ points in x direction for our geometry. We define

$$\boldsymbol{j}(t) = \boldsymbol{j} = \boldsymbol{j}_1 \cos(\omega t - \theta_j) \ , \tag{8.2}$$

where ω is the rf frequency, θ_j is the phase shift between the microwave in the CPW and the induced $\boldsymbol{j}$ in the Co film.

The direction of the Co film magnetization $\boldsymbol{M}$ is defined via the angle α between the Co film plane and $\boldsymbol{M}$ and the angle β between $\boldsymbol{M}$ and the x axis within the film plane. We distinguish between the static components α_0, β_0, displayed in figure 8.8(a) and the dynamic components $\alpha_t(t)$, $\beta_t(t)$, shown in figure 8.8(b). The static components define the direction of the equilibrium magnetization $\boldsymbol{M}_0$. It is governed by the static external field and by the anisotropy field of the Co film. The CPW underneath the structure induces a rf magnetic field $\boldsymbol{h}_{rf}$ in z direction. Only for $\alpha_0 = 0°$ and $\beta_0 = 90°$

[5] At the Universität Hamburg.

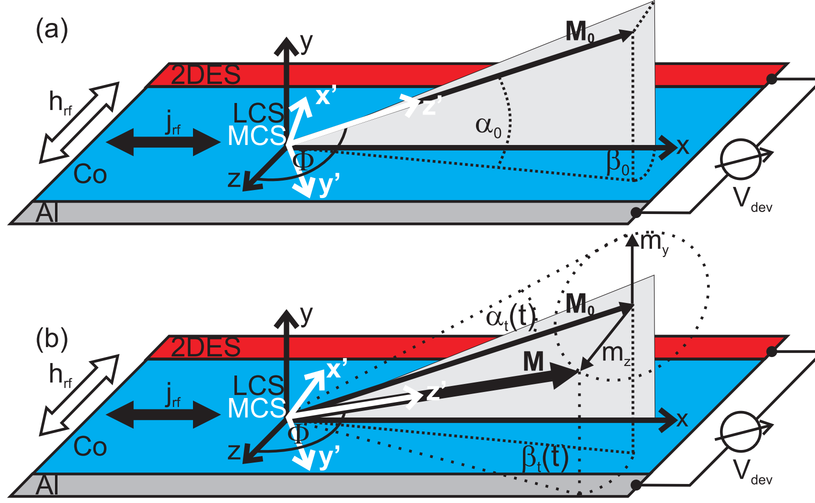

Figure 8.8: Scheme of our measurement configuration. Out–of–plane angles are labeled α, in–plane angles are labeled β. Note that β_0, as depicted here as an example, is negative. In (a) the equilibrium magnetization is described by the angles α_0 and β_0. In (b) the dynamic magnetization angles α_t and β_t are displayed, which describe the precession of $\boldsymbol{M}$.

no precession of $\boldsymbol{M}$ can be excited (see section 2.4). For the dynamic components of the magnetization angle we define

$$\begin{aligned} \alpha_t\left(t\right) &= \alpha_1\cos\left(\omega t-\theta_m\right) \\ \text{and } \beta_t\left(t\right) &= -\beta_1\sin\left(\omega t-\theta_m\right) \ . \end{aligned} \tag{8.3}$$

The amplitudes are given by the aperture angles of the (elliptic) precession cone $\sin\alpha_1 = m_y/M_0 \simeq \alpha_1$ and $\sin\beta_1 = m_z/M_0 \simeq \beta_1$. Accordingly, the total angles are $\alpha(t) = \alpha_0 + \alpha_t(t)$, and $\beta(t) = \beta_0 + \beta_t(t)$. In the following we use the short notation α instead of $\alpha(t)$ and β instead of $\beta(t)$ for the time dependent angles.

In the LCS $\boldsymbol{M}$ and $\boldsymbol{j}$ read

$$\boldsymbol{j} = \begin{pmatrix} j \\ 0 \\ 0 \end{pmatrix} \text{ and } \boldsymbol{M} = M_0 \begin{pmatrix} \cos\alpha\cos\beta \\ \sin\alpha \\ \cos\alpha\sin\beta \end{pmatrix} .$$

The MCS (white) is the CS in which $\boldsymbol{M}$ is pointing in z' direction (see figure 8.8). The y' axis is defined such that a single rotation of the MCS around this axis by an angle Φ maps z' onto the z axis of the LCS. With these presumptions the unit vector z' is defined in the LCS by

$$\boldsymbol{z'} = \begin{pmatrix} \cos\alpha\cos\beta \\ \sin\alpha \\ \cos\alpha\sin\beta \end{pmatrix} .$$

To find the transformation matrix $\boldsymbol{T}^{LCS}_{MCS}(\alpha,\beta)$, for which $(\boldsymbol{x'},\boldsymbol{y'},\boldsymbol{z'}) = \boldsymbol{T}^{LCS}_{MCS}(\alpha,\beta)(\boldsymbol{x},\boldsymbol{y},\boldsymbol{z})$, we determine the rotation that maps $\boldsymbol{z}$ onto $\boldsymbol{z'}$. The rotation axis $\boldsymbol{v_r}$ is perpendicular

to $\boldsymbol{M}$ and $\boldsymbol{z}$,

$$\boldsymbol{v}_r = \|\boldsymbol{M} \times \boldsymbol{z}\| = \left\| \begin{pmatrix} \cos\alpha\cos\beta \\ \sin\alpha \\ \cos\alpha\sin\beta \end{pmatrix} \times \begin{pmatrix} 0 \\ 0 \\ 1 \end{pmatrix} \right\| = N_1 \begin{pmatrix} \sin\alpha \\ -\cos\alpha\cos\beta \\ 0 \end{pmatrix} ,$$

where $N_1 = \frac{1}{\sqrt{(\cos^2\alpha)(\cos^2\beta)+\sin^2\alpha}}$ is the norming factor. The rotation angle $\Phi(\alpha, \beta)$ is defined by the scalar product of $\boldsymbol{M}$ and $\boldsymbol{z}$

$$\cos\Phi = \cos\alpha\sin\beta \; .$$

The CS rotation is determined by $\boldsymbol{v}_r$ and Φ in mathematically positive direction. Note that both, the rotation vector and the angle Φ, are time dependent.

Generally, the matrix for a rotation by an angle Φ around a vector $\boldsymbol{v}$ is $\boldsymbol{R} =$

$$\begin{pmatrix} \cos\Phi + v_1^2(1-\cos\Phi) & v_1v_2(1-\cos\Phi) - v_3\sin\Phi & v_1v_3(1-\cos\alpha) + v_2\sin\Phi \\ v_2v_1(1-\cos\Phi) + v_3\sin\Phi & \cos\Phi + v_2^2(1-\cos\Phi) & v_2v_3(1-\cos\Phi) - v_1\sin\Phi \\ v_3v_1(1-\cos\Phi) - v_2\sin\Phi & v_3v_2(1-\cos\Phi) + v_1\sin\Phi & \cos\Phi + v_3^2(1-\cos\Phi) \end{pmatrix} .$$

Thus, our matrix that transforms coordinates from the LCS into the MCS reads $\boldsymbol{T}_{MCS}^{LCS}(\alpha, \beta) =$

$$\begin{pmatrix} \cos\Phi - N_1^2\left(\sin^2\alpha\right)(\cos\Phi - 1) & N_1^2(\cos\alpha\cos\beta\sin\alpha)(\cos\Phi - 1) & -\cos\alpha\cos\beta \\ N_1^2(\cos\alpha\cos\beta\sin\alpha)(\cos\Phi - 1) & \cos\Phi - N_1^2\left(\cos^2\Phi\right)(\cos\Phi - 1) & -\sin\alpha \\ \cos\alpha\cos\beta & \sin\alpha & \cos\Phi \end{pmatrix} . \tag{8.4}$$

Accordingly, the current density vector $\boldsymbol{j}$ (which points in the x direction in the LCS) is given in the MCS by

$$\boldsymbol{j} = \boldsymbol{T}_{MCS}^{LCS}(\alpha, \beta) \begin{pmatrix} j \\ 0 \\ 0 \end{pmatrix} = \begin{pmatrix} j\left(\cos\alpha\sin\beta - N_1^2\left(\sin^2\alpha\right)(\cos\alpha\sin\beta - 1)\right) \\ jN_1^2(\cos\alpha\cos\beta\sin\alpha)(\cos\alpha\sin\beta - 1) \\ j\cos\alpha\cos\beta \end{pmatrix} .$$

Equations 2.28 and 2.30 define the resistivity tensors for the IPHE and for the AHE. Both effects are described simultaneously by the resistivity tensor

$$\boldsymbol{\rho}' = \begin{pmatrix} \rho_\perp & -\rho_{AHE} & 0 \\ \rho_{AHE} & \rho_\perp & 0 \\ 0 & 0 & \rho_\| \end{pmatrix} .$$

This matrix is defined within the MCS where $\boldsymbol{M}$ points in z direction. In this CS we find for the electric field

$$\begin{aligned} \varepsilon' &= \boldsymbol{\rho}'\boldsymbol{j} \qquad (8.5) \\ &= j \begin{pmatrix} \rho_\perp & -\rho_{AHE} & 0 \\ \rho_{AHE} & \rho_\perp & 0 \\ 0 & 0 & \rho_\| \end{pmatrix} \begin{pmatrix} N_1^2\sin^2\alpha(\cos\alpha\sin\beta - 1) + \cos\alpha\sin\beta \\ -N_1^2\cos\beta(\cos\alpha\sin\beta - 1)\cos\alpha\sin\alpha \\ \cos\alpha\cos\beta \end{pmatrix} = \end{aligned}$$

$$j \begin{pmatrix} \rho_\perp\left(\cos\Phi - N_1^2\left(\sin^2\alpha\right)(\cos\Phi - 1)\right) - \rho_A N_1^2(\cos\alpha\cos\beta\sin\alpha)(\cos\Phi - 1) \\ \rho_A\left(\cos\Phi - N_1^2\left(\sin^2\alpha\right)(\cos\Phi - 1)\right) + \rho_\perp N_1^2(\cos\alpha\cos\beta\sin\alpha)(\cos\Phi - 1) \\ \rho_\|\cos\alpha\cos\beta \end{pmatrix}$$

The quantity which is experimentally accessible is the z component of the electric field in the LCS. Thus we transform the electric field vector from equation 8.5 into the LCS,

$$\varepsilon = \boldsymbol{T}_{LCS}^{MCS}(\alpha,\beta)\,\varepsilon',$$

where $\boldsymbol{T}_{LCS}^{MCS} = \left(\boldsymbol{T}_{MCS}^{LCS}\right)^{-1}$. We obtain

$$= j\begin{pmatrix} \rho_\perp + \left(\rho_\| - \rho_\perp\right)\cos^2\alpha\cos^2\beta \\ \rho_{AHE}\cos\alpha\sin\beta + \left(\rho_\| - \rho_\perp\right)\sin\alpha\cos\alpha\cos\beta \\ -\rho_{AHE}\sin\alpha + \frac{1}{2}\left(\rho_\| - \rho_\perp\right)\cos^2\alpha\sin(2\beta) \end{pmatrix}. \quad (8.6)$$

Setting $\alpha = 0°$ in the latter equation yields the electric field for an in–plane magnetization

$$\varepsilon_{\alpha=0} = \begin{pmatrix} j\left(\rho_\perp + \left(\rho_\| - \rho_\perp\right)\cos^2\beta\right) \\ j\rho_{AHE}\sin\beta \\ j\frac{1}{2}\left(\rho_\| - \rho_\perp\right)\sin(2\beta) \end{pmatrix},$$

what is the known result for the AMR effect and the AHE from equations 2.28 and 2.30 in chapter 2.

The z component of the electric field in equation 8.6 is

$$\varepsilon_z = j\left(-\rho_{AHE}\sin\alpha + \frac{1}{2}\left(\rho_\| - \rho_\perp\right)\cos^2\alpha\sin(2\beta)\right). \quad (8.7)$$

Now we investigate the response of ε_z on a precessing magnetization. To find the non–vanishing terms in time average we use MacLaurin's expansion about the time dependent terms in ε_z, $\alpha_t(t)$ and $\beta_t(t)$, which are defined in equation 8.3. For small precession angles, i.e. small α_1 and β_1, the approximation of ε_z to first order is adequate. ε_z reads

$$\varepsilon_z = j\left(-\rho_{AHE}\sin(\alpha_0+\alpha_t) + \frac{1}{2}\left(\rho_\| - \rho_\perp\right)\cos^2(\alpha_0+\alpha_t)\sin(2(\beta_0-\beta_t))\right),$$

and the expansion is defined by

$$\varepsilon_z = \varepsilon_z\Big|_{\alpha_t=\beta_t=0,} + \frac{\partial\varepsilon_z}{\partial\alpha_t}\Big|_{\alpha_t=\beta_t=0}\alpha_t + \frac{\partial\varepsilon_z}{\partial\beta_t}\Big|_{\alpha_t=\beta_t=0}\beta_t + O\left(\alpha_t^2\right) + O\left(\beta_t^2\right). \quad (8.8)$$

We evaluate the second and the third term separately:

$$\frac{\partial\varepsilon_z}{\partial\alpha_t}\Big|_{\alpha_t=\beta_t=0}\alpha_t = -j\alpha_t\left(\rho_{AHE}\cos\alpha_0 - \frac{1}{2}\left(\rho_\perp - \rho_\|\right)\sin(2\alpha_0)\sin(2\beta_0)\right),$$

and with equations 8.2 and 8.3

$$\begin{aligned} &= -j_1\left(\cos(\omega t - \theta_j)\right)\left(\alpha_1\cos(\omega t - \theta_m)\right)\cdot \\ &\quad \left(\rho_{AHE}\cos\alpha_0 - \frac{1}{2}\left(\rho_\perp - \rho_\|\right)\sin(2\alpha_0)\sin(2\beta_0)\right) \\ &= -\frac{1}{2}j_1\alpha_1\left(\cos(\theta_j+\theta_m-2\omega t) + \cos(\theta_j-\theta_m)\right)\cdot \\ &\quad \left(\rho_{AHE}\cos\alpha_0 - \frac{1}{2}\left(\rho_\perp - \rho_\|\right)\sin(2\alpha_0)\sin(2\beta_0)\right). \end{aligned}$$

The third term is

$$\left.\frac{\partial \varepsilon_z}{\partial \beta_t}\right|_{\alpha_t=\beta_t=0} \beta_t = j\beta_t \cos(2\beta_0)\left(\cos^2\alpha_0\right)\left(\rho_\perp - \rho_\parallel\right) \ .$$

Analog to the second term, we use equations 8.2 and 8.3 and find

$$\begin{aligned} & j_1 \left(\cos(\omega t - \theta_j)\right)\left(\beta_1 \sin(\omega t - \theta_m)\right)\cos(2\beta_0)\left(\cos^2\alpha_0\right)\left(\rho_\parallel - \rho_\perp\right) \\ = \ & \frac{1}{2} j_1\beta_1 \left(\sin(\theta_j - \theta_m) + \sin(\theta_j + \theta_m - 2\omega t)\right)\cos(2\beta_0)\left(\cos^2\alpha_0\right)\left(\rho_\perp - \rho_\parallel\right) \ . \end{aligned}$$

Now we combine the terms using equation 8.8 to

$$\begin{aligned} \varepsilon_z = \ & -j_1 \cos(\omega t - \theta_j) \cdot \\ & \left(\rho_{AHE} \sin\alpha_0 - \frac{1}{4}\sin(2\beta_0)\cos(2\alpha_0) + 1\left(\rho_\parallel - \rho_\perp\right)\right) \\ & -\frac{1}{2} j_1\alpha_1 \left(\cos(\theta_j + \theta_m - 2\omega t) + \cos(\theta_j - \theta_m)\right) \cdot \\ & \left(\rho_{AHE} \cos\alpha_0 + \frac{1}{2}\left(\rho_\parallel - \rho_\perp\right)\sin(2\alpha_0)\sin(2\beta_0)\right) \\ & +\frac{1}{2} j_1\beta_1 \left(\sin(\theta_j - \theta_m) - \sin(\theta_j + \theta_m - 2\omega t)\right)\cos(2\beta_0) \cdot \\ & \left(\cos^2\alpha_0\right)\left(\rho_\parallel - \rho_\perp\right) \ . \end{aligned}$$

The last step is to calculate the time average of the electric field $\langle\varepsilon_z\rangle_t$ which governs the dc voltage signal. For this we use $\left\langle\cos^2(\omega t)\right\rangle_t = \left\langle\sin^2(\omega t)\right\rangle_t = 1/2$ and $\langle\cos(\omega t + x)\rangle_t = \langle\sin(\omega t + x)\rangle_t = 0$ and obtain

$$\begin{aligned} \langle\varepsilon_z\rangle_t = \ & -\frac{1}{2} j_1\alpha_1 \cos(\theta_j - \theta_m) \cdot \\ & \left(\rho_{AHE} \cos\alpha_0 + \frac{1}{2}\left(\rho_\parallel - \rho_\perp\right)\sin(2\alpha_0)\sin(2\beta_0)\right) \\ & +\frac{1}{2} j_1\beta_1 \sin(\theta_j - \theta_m)\cos(2\beta_0)\left(\cos^2\alpha_0\right)\left(\rho_\parallel - \rho_\perp\right) \ . \end{aligned} \tag{8.9}$$

The time averaged z component of the electric field multiplied with the distance d between the Al and the 2DES contact yields the measurable device voltage:

$$V_{dev} = \langle\varepsilon_z(t)\rangle_t \, d \ . \tag{8.10}$$

Our data do not provide all parameters needed for a quantitative analysis of equation 8.9. Thus, for some parameters, we use values provided in literature and adapt them for our purpose. In table 8.11 we summarize and comment on the relevant input

parameters to calculate V_{dev}.

quantity	comment
$j_1 = 2 \times 10^9 \ \mathrm{A\,m^{-2}}$	In [Cos06b] induced rf currents of $\approx 20\ \mu$A at $P_{rf} = 9$ dBm are reported through a cross section of $300 \times 35\ \mathrm{nm}^2$.
$\beta_1 = 0.012°$	Obtained from computer simulations as explained above and in section 3.2.1.
$\alpha_1 = 0.0018°$	Obtained from computer simulations as explained above and in section 3.2.1.
$\theta_m = 90°$	At FMR the phase–shift between the magnetization precession and the exciting field is 90° [Gie07].
$\theta_j = 20°$	In [Cos06b] the in–phase and out–of–phase components of the induced current I_1 and I_2 are determined. We use $\tan\theta_j = I_2/I_1$.
$\rho_{\parallel} - \rho_{\perp} = 1.96 \times 10^{-9}\ \Omega\,\mathrm{m}$	Taken from [Gil05].
$\rho_{AHE} = 2 \times 10^{-9}\ \Omega\,\mathrm{m}$	Taken from [Köt05].
$d = 50 \times 10^{-9}\ \mathrm{m}$	Distance between the Al contact and the 2DES.

(8.11)

The plots in figure 8.9 show the calculated device voltage V_{dev} as a function of the magnetization direction defined by α_0 and β_0. The values shown in table (8.11) are used.

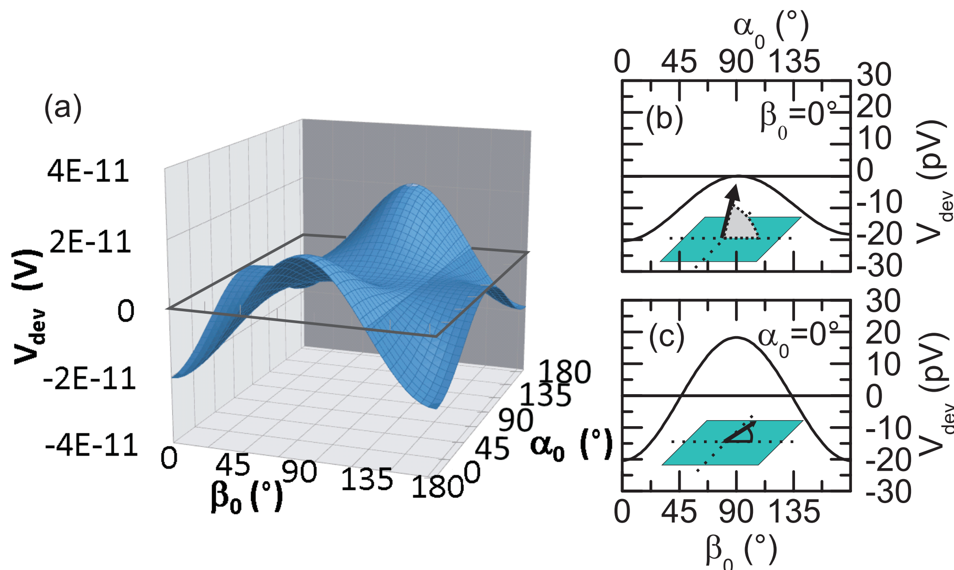

Figure 8.9: Calculated voltage drop between the Al contact and the 2DES as a function of the magnetization direction. The latter is defined via the out–of–plane angle α_0 and the in–plane angle β_0. The parameters given in table 8.11 are used.

In section 8.1 we provided evidence for an out–of–plane magnetic anisotropy. In this case the in–plane angle $\beta_0 = 0°$ and, sweeping the external magnetic field from high positive $\mu_0 H_x$ to zero, the out–of–plane angle varies from $\alpha_0 = 0°$ to 90°. The

behavior of V_{dev} for this scenario is illustrated in figure 8.9(b). On the scale of this figure our model predicts a sign change for the given parameter set. At $\alpha_0 = 93°$ V_{dev} amounts 0.04 pV. However this will not be resolvable experimentally. With these input parameters we find that a resolvable sign change of V_{dev} (α_0,β_0) only occurs if β_0 is varied. Figure 8.9(c) depicts this case, where $\alpha_0 = 0°$. We vary the in–plane angle β_0 from 0° to 180° and find two sign changes at $\beta_0 = 45°$ and 135°. The voltage maximum is reached at $\beta_0 = 90°$. The curve is almost symmetric about $\beta_0 = 90°$. Both, the two sign changes and the symmetry corresponds qualitatively to our experiment. This simulation commends an in–plane anisotropy of the Co film with an easy axis in z direction, i.e. $\beta_0 = 90°$.

In our experiment the rf current in the Co is induced by means of inductive and capacitive coupling between the CPW and the sample. With our experimental setup the phase shift θ_j is not well definable. Thus it is instructive to illustrate the particular sensitivity on the phase difference $\theta_j - \theta_m$. Figure 8.10 shows V_{dev} (α_0,β_0) with the same parameters as in 8.9 for three different $\theta_j - \theta_m$. We find that for $9° < |\theta_j - \theta_m| < 171°$

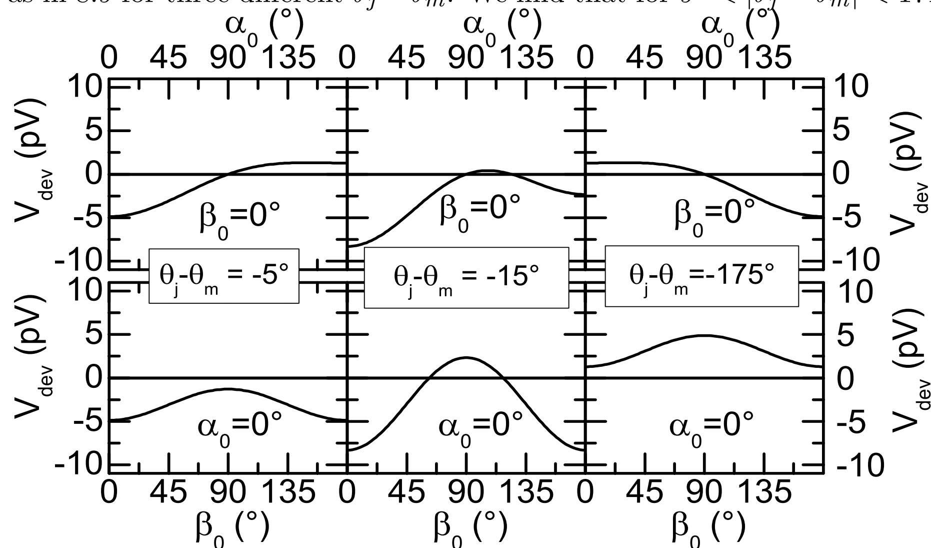

Figure 8.10: Calculated voltage drop between the Al contact and the 2DES as a function of the magnetization direction. The plots are analog to figure 8.9(b) and (c) but with different phase relations $\theta_j - \theta_m$ between the induced rf current and the magnetization precession.

with exception of $|\theta_j - \theta_m| = 90°$ two sign changes of the voltage signal occur if $\boldsymbol{M}_0$ is reversed via the out–of–plane direction. Such a configuration is shown in the upper middle panel of figure 8.10. The sign changes in this graph occur at $\alpha_0 = 90°$ and 125°. Interestingly, this signature is not symmetric. One might speculate that such a scenario could explain the data measured at higher modulation frequencies f_m as shown in figure 8.5, for example.

The left and right upper panels show typical device voltage signatures for $\theta_j - \theta_m > -9°$ and $\theta_j - \theta_m < -171°$, respectively. Here the sign of the calculated voltage changes only once when $\boldsymbol{M}_0$ passes the perpendicular–to–film plane direction. This characteristics is not observed experimentally.

The curves in the lower panels in figure 8.10 show V_{dev} for a magnetization reversal with $\boldsymbol{M}_0$ staying in–plane (i.e. $\alpha_0 = 0$). Consistent with figure 8.9 nearly symmetric signatures about $\beta_0 = 90°$ are seen for all phase differences. The voltage level is solely negative for $\theta_j - \theta_m > -9°$ and solely positive for $\theta_j - \theta_m < -171°$. No sign changes are found in these regimes.

Quantitatively the model calculations yield voltages that are below the measured data. The values differ by four orders of magnitude. The reliability of quantitative analyses is reduced due to the lack of measured input parameters for our device. Further we did not consider high–frequency effects on the susceptibility and on the conductivity tensor of the Co layer. These effects are discussed in [Cos06b] and in [Mec07]. The most significant feature of this model is the prediction of sign changes as a function of the magnetization angle. For this reason we consider model C to be most suitable to explain our data.

Chapter 9

Conclusions

In this thesis we presented extensive theoretical and experimental studies on hybrid structures. In the first we investigated spin transport in a nanoscopic spin FET device at low temperatures and in the second part we discussed the dynamic photovoltage of a NM/FM/NM hybrid structure under microwave irradiation.

The device of the first part consisted of two FM contacts separated by an InAs heterostructure incorporating a 2DES. Calculations of the spin–orbit coupling in the InAs heterostructure based on a tight–binding model were performed. We found that the coupling parameter caused by the bulk inversion asymmetry of the InAs α_{BIA} is of the same order of magnitude as α_{SIA} which describes the spin–orbit coupling resulting from the structure inversion asymmetry. α_{BIA} dominated the spin–orbit coupling for our heterostructure design. From α_{BIA} and α_{SIA} we calculated a total spin–orbit coupling parameter α. Our calculations yield that it is tunable by an external electric field and takes values between 0.025 eVÅ and 0.09 eVÅ. The predicted range is a factor of 10 smaller than previously published experimentally determined values. Furthermore, we found that the electric field varies α_{BIA} rather than α_{SIA}. This was in contrast to the orthodox understanding.

For our non–planar sample design it is not trivial to determine the impact of an applied gate voltage on the 2DES. We performed computer simulations to obtain the potential landscape in our device. These revealed that the 2DES area where the electric field from the gate electrode was effective was limited to an area of 100×40 nm^2 between the source and the drain contact.

We examined the spin dependent electron transmission of a nanoscopic FM/InAs (2DES)/FM device by computer simulations. The inverted transmission is proportional to the voltage measured in our transport experiments. Assuming first zero spin–orbit coupling in the 2DES we found that the variation of the gate voltage leads to an oscillatory behavior of the transmission. This is caused by the variation of the potential landscape in the 2DES as a function of the gate voltage. The electron states vary between resonant and non–resonant states what is reflected in the transmission.
Second, in a calculation the gate voltage was set to a fixed value and α was varied. The amplitude of the spin–orbit coupling driven resistance oscillation is 1 % of the signature found for a variation of the potential landscape by the gate voltage. The characteristics of the device resistance differed significantly from the sinusoidal trace referring to S. Datta and B. Das.
Third, assuming spin split electron states in the FM contacts we calculated the trans-

mission change for parallel and antiparallel contact magnetizations. By this means we studied the GMR effect in the model device. For realistic parameters we predicted a GMR effect of about 5 %.

In magnetotransport measurements we investigated a Co/InAs (2DES)/Co spin FET device fabricated using in situ CEO and a special mix–and–match lithography technique. This included AFM patterning ("nanoindenting") and FIB etching. By this means, our particular sample design meets the requirements of a ballistic spin–FET. The length of the 2DES channel between the Co contacts on the cleaved edge is below 100 nm. We determined a spin scattering length in the order of this separation and thus interpreted our experiments in the framework of quasi–ballistic spin transport. We applied a magnetic field in the plane of the 2DES and of the Co contacts. In this geometry we avoid the influence of stray field effects from the FM electrodes on the 2DES. Sweeping the magnetic field between ± 1 T we measured a GMR effect of $-0.014\,\%$. This was attributed to a spin polarized current flowing across the Co/InAs (2DES) interfaces. We calculated a spin polarization of 1 % . For magnetic fields applied perpendicular to the 2DES plane we observed signatures of the EMR effect.

On the same device we measured reproducible oscillations of the dynamic device resistance as a function of an applied gate voltage. The magnitude of these oscillations depended on the angle between the magnetization $\boldsymbol{M}$ of the Co contacts and the 2DES plane. For $\boldsymbol{M}$ perpendicular to the 2DES, the oscillations almost vanished, whereas the highest amplitudes were found for $\boldsymbol{M}$ aligned parallel to the 2DES. From temperature dependent measurements we extrapolated that the spin polarization at $T = 0$ K at the Co/2DES interfaces is 7 %. The spin polarization extracted directly from a GMR experiment was 1 % at 4.5 K. The relative oscillation amplitude of the dynamic device resistance falls below the signal noise level at $T = 21$ K. This temperature is relatively high if compared with literature values for spin transport experiments. We attribute this to the high purity of our Co/2DES interfaces.

The magnetic field– and temperature dependence of the observed signature suggested that our device was a spin FET and the resistance oscillations were due to a variation of the spin precession angle in the 2DES channel. The gate voltage regime studied in the experiment did not agree quantitatively with the theoretical prediction. However, as the absolute value of α measured in further experiments was also a factor of 10 larger than predicted, one can still assume that the resistance change was induced by a variation of α.

In the following we summarize room temperature experiments on Al/Co/InAs (2DES) hybrid structures under microwave irradiation. The FMR revealed a magnetic anisotropy of the Co film we used. Further analysis suggested a magnetic easy axis perpendicular to the film plane.

We measured the voltage drop across the hybrid structure as a function of the rf frequency and of an applied magnetic field. The induced voltage signal showed a dip for magnetic fields $|\mu_0 H|$ below the anisotropy field of 30 mT and a peak for fields above 30 mT. We demonstrated that these resonant voltage signatures coincided with the resonant precession of the magnetization, i.e. the FMR. The observed sign changes of the device voltage at 30 mT and the presence of a signature below 30 mT were unexpected and went beyond the results from the inductively measured FMR data. Measuring the resonant voltage signal allowed to determine the FMR in a magnetic field range where the inductively measured signal was below the SNR.

We further found that the amplitude of the voltage signature depended on the rf power. And if a dc current of 1 μA was applied to the Al/Co/InAs (2DES) hybrid structure the voltage drop increased by a factor of 4.5. We excluded that the signal is caused by rectification of a rf induced ac current, based on a diode–like behavior of the device.

For the discussion of the origin of the resonant dc voltage signal we presented three models. The first model was the voltage drop at FM/NM interfaces due to the spin battery effect. Calculating the device voltage on the basis of this model yielded 0.1 pV what was five orders of magnitude below the measured voltage. Further, no sign change of the voltage signal is predicted. Considering the geometry of our device we found that the spin accumulation in the NM should dephase due to the Hanle effect for magnetic fields below the anisotropy field of 30 mT. As a consequence, the voltage signal would not appear with opposite sign below 30 mT.

In the second model we discussed the AMR effect to cause the voltage drop. In principle this model could explain the occurrence of the resonant voltage peak due to a large magnetization precession cone angle at FMR. But we excluded this effect for the following reasons: First, a dc current of 0.2 μA must be presumed for the AMR effect to cause the observed voltage peaks but none of the considered mechanisms gave rise to such a current flowing through our hybrid structure. Second, the sign changes of the device voltage at magnetic fields of ±30 mT could not be explained.

The third model included detailed calculations of the Hall voltage. A Hall voltage is expected to arise from an induced rf current in the Co film and a precessing magnetization. We considered the dynamic IPHE and the dynamic AHE. The time average of these effects yielded non–vanishing terms, i.e. a dc voltage was predicted. Furthermore, this model predicts sign changes of this voltage. For a quantitative interpretation of our data with this model device specific input parameters are needed. We could not extract these parameters from our results. Hence, we used literature values and computer simulations of comparable structures. The calculated device voltage is four orders of magnitude smaller than the measured data. As this is considered to be the most promising model to explain our data we suggest to determine the input parameters experimentally. A better matching with the experiment would be achieved by using rf susceptibilities which have to be measured carefully in a special experiment. This went beyond this thesis and remains open to be done in a future project.

A. List of abbreviations

2DES	two–dimensional electron system
ac	alternating current
AFM	atomic force microscope
AHE	anomalous Hall effect
AMR	anisotropic magnetoresistance
CEO	cleaved–edge overgrowth
CPW	coplanar waveguide
CS	coordinate system
dc	direct current
DP	D'yakonov–Perel'
EMR	extraordinary magnetoresistance
EY	Elliott–Yafet
FET	field–effect transistor
FIB	focused ion beam
FM	ferromagnetic metal
GMR	giant magnetoresistance
IPHE	in–plane Hall effect
LIA	lock–in amplifier
MR	magnetoresistance
NM	non–ferromagnetic metal
QHE	quantum Hall effect
QW	quantum well
rf	radio frequency in the GHz range
SC	semiconductor
SNR	signal–to–noise ratio
SRM	spin relaxation mechanism

Bibliography

[Ahl01] E. Ahlswede, P. Weitz, J. Weis, K. von Klitzing and K. Eberl. *Hall potential profiles in the quantum Hall regime measured by a scanning force microscope*. Physica B: Condensed Matter **289**, 562–566 (2001).

[And82] Tsuneya Ando, Alan B. Fowler and Frank Stern. *Electronic properties of two-dimensional systems*. Rev. Mod. Phys. **54**, 437–672 (1982).

[App07] Ian Appelbaum and Douwe J. Monsma. *Transit-time spin field-effect transistor*. Applied Physics Letters **90**, 262501 (2007).

[Ash76] N. W. Ashcroft and N. D. Mermin. *Solid State Physics*. Saunders College Publishing, 1976.

[Aws02] D. D. Awschalom, D. Loss, N. Samarth and H. X. Tang. *Nanoscience and Technology*, p. 31–92. Springer Verlag Berlin Heidelberg New York, 2002.

[Bah07] M. S. Bahramy, P. Murugan, G. P. Das and Y. Kawazoe. *Calculations of spin-induced transport in ferromagnets*. Phys. Rev. B **75**, 054404 (2007).

[Bai89] M. N. Baibich, J. M. Broto, A. Fert, F. Nguyen, Van Dan, F. Petroff, P. Etienne, G. Grenzet, A. Friederich and J. Chazelas. *Giant magnetoresistance of (001)Fe/(001)Cr magnetic superlattices*. Phys. Rev. B **39**, 4828 (1989).

[Bar04] M. Barthelmess, C. Pels, A. Thieme and G. Meier. *Stray fields of domains in permalloy microstructures—measurements and simulations*. Journal of Applied Physics **95**, 5641–5645 (2004).

[Bas90] J. Barnaś, A. Fuss, R. E. Camley, P. Grünberg and W. Zinn. *Novel magnetoresistance effect in layered magnetic structures: Theory and experiment*. Phys. Rev. B **42**, 8110–8120 (1990).

[Bin89] G. Binasch, P. Grünberg, F. Saurenbach and W. Zinn. *Enhanced magnetoresistance in layered magnetic structures with antiferromagnetic interlayer exchange*. Phys. Rev. B **39**, 4828 (1989).

[Bir76] L. L. Bir, A. G. Aronov and G. E. Pikus. *Spin relaxation of electrons due to scattering by holes*. Sov. Phys. JETP **42**, 705 (1976).

[Boc07] L. Bocklage, J. M. Scholtyssek, U. Merkt and G. Meier. *Spin polarization of* Ni_2MnIn *and* $Ni_{80}Fe_{20}$ *determined by point-contact andreev spectroscopy*. 10th JOINT MMM/INTERMAG CONFERENCE **101**, 09J512 (2007).

[Bot06a] B. Botters. *Ferromagnetische Resonanz an dünnen Heusler-Filmen und einem nanostrukturierten Permalloy-Ring.* Diploma thesis, Universität Hamburg, 2006.

[Bot06b] B. Botters, F. Giesen, J. Podbielski, P. Bach, G. Schmidt, L.W. Molenkamp and D. Grundler. *Stress dependence of ferromagnetic resonance and magnetic anisotropy in a thin NiMnSb film on InP(001).* Applied Physics Letters **89**, 242505 (2006).

[Bra00] A. Brataas, Yu. V. Nazarov and Gerrit E. W. Bauer. *Finite-element theory of transport in ferromagnet–normal metal systems.* Phys. Rev. Lett. **84**, 2481–2484 (2000).

[Bra02] A. Brataas, Y. Tserkovnyak, G. E. W. Bauer and B. I. Halperin. *Spin battery operated by ferromagnetic resonance.* Phys. Rev. B **66**, 060404 (2002).

[Bue85] M. Buettiker, Y. Imry, R. Landauer and S. Pinhas. *Generalized many-channel conductance formula with application to small rings.* Phys. Rev. B **31**, 6207–6215 (1985).

[But96] W. H. Butler, X.-G. Zhang, D. M. C. Nicholson, T. C. Schulthess and J. M. MacLaren. *Giant magnetoresistance from an electron waveguide effect in cobalt-copper multilayers.* Phys. Rev. Lett. **76**, 3216–3219 (1996).

[Byc84a] Y. A. Bychkov and É. I. Rashba. *Properties of a 2D electron gas with lifted spectral degeneracy.* Soviet Journal of Experimental and Theoretical Physics Letters **39**, 78–81 (1984).

[Byc84b] Yu. A. Bychkov and E. I. Rashba. *Oscillatory effects and the magnetic susceptibility of carriers in inversion layers.* J. Phys. C: Solid State Physics **17**, 6039–6045 (1984).

[Cal73] J. Callaway and C. S. Wang. *Self-consistent calculation of energy bands in ferromagnetic nickel.* Phys. Rev. B **7**, 1096–1103 (1973).

[Chi97] W.-C. Chiang, Q. Yang, Jr. W. P. Pratt, R. Loloee and J. Bass. *Variation of multilayer magnetoresistance with ferromagnetic layer sequence: Spin-memory loss effects.* The 41st annual conference on magnetism and magnetic materials **81**, 4570–4572 (1997).

[Chk92] D. B. Chklovskii, B. I. Shklovskii and L. I. Glazman. *Electrostatics of edge channels.* Phys. Rev. B **46**, 4026–4034 (1992).

[Cos06a] M. V. Costache, M. Sladkov, S. M. Watts, C. H. van der Wal and B. J. van Wees. *Electrical detection of spin pumping due to the precessing magnetization of a single ferromagnet.* Physical Review Letters **97**, 216603 (2006).

[Cos06b] M. V. Costache, S. M. Watts, M. Sladkov, C. H. van der Wal and B. J. van Wees. *Large cone angle magnetization precession of an individual nanopatterned ferromagnet with dc electrical detection.* Applied Physics Letters **89**, 232115 (2006).

[Cos06c] M. V. Costache, M. Zaffalon and B. J. van Wees. *Spin accumulation probed in multiterminal lateral all-metallic devices.* Physical Review B (Condensed Matter and Materials Physics) **74**, 012412 (2006).

[Dat90] S. Datta and B. Das. *Electronic analog of the electro-optic modulator.* Applied Physics Letters **56**, 665–667 (1990).

[dG83] R. A. de Groot, F. M. Mueller, P. G. van Engen and K. H. J. Buschow. *New class of materials: Half-metallic ferromagnets.* Phys. Rev. Lett. **50**, 2024–2027 (1983).

[Dre55] G. Dresselhaus. *Spin-orbit coupling effects in zinc blende structures.* Phys. Rev. **100**, 580–586 (1955).

[Dre99] M. Dreyer, M. Kleiber, A. Wadas and R. Wiesendanger. *Composition-driven change of the magnetic anisotropy of ultrathin Co/Au(111) films studied by means of magnetic-force microscopy in ultrahigh vacuum.* Phys. Rev. B **59**, 4273 (1999).

[D'y71] M. I. D'yakonov and V. I. Perel'. *Spin orientation of electons associated with the interband absorption of light in semiconductors.* Soviet Physics JETP **33**, 1053 (1971).

[Ell54] R. J. Elliott. *Theory of the effect of spin-orbit coupling on magnetic resonance in some semiconductors.* Phys. Rev. **96**, 266–279 (1954).

[Eng97] G. Engels, J. Lange, Th. Schäpers and H. Lüth. *Experimental and theoretical approach to spin splitting in modulation-doped InGaAs/InP quantum wells for $B \rightarrow 0$.* Phys. Rev. B **55**, R1958–R1961 (1997).

[Fab07] J. Fabian, A. Matos-Abiague, C. Ertler, P. Stano and I. Zutić. *Semiconductor spintronics.* Acta Physica Slovaca **57**, 565–907 (2007).

[Fer01] A. Fert and H. Jaffrès. *Conditions for efficient spin injection from a ferromagnetic metal into a semiconductor.* Phys. Rev. B **64**, 184420 (2001).

[Gan03] S. D. Ganichev and W. Prettl. *Spin photocurrents in quantum wells.* Journal of Physics: Condensed Matter **15**, R935–R983 (2003).

[Gan04] S. D. Ganichev, V. V. Bel'kov, L. E. Golub, E. L. Ivchenko, Petra Schneider, S. Giglberger, J. Eroms, J. De Boeck, G. Borghs, W. Wegscheider, D. Weiss and W. Prettl. *Experimental separation of Rashba and Dresselhaus spin splittings in semiconductor quantum wells.* Physical Review Letters **92**, 256601 (2004).

[Gie05] F. Giesen, J. Podbielski, T. Korn, M. Steiner, A. van Staa and D. Grundler. *Hysteresis and control of ferromagnetic resonances in rings.* Applied Physics Letters **86**, 112510 (2005).

[Gie07] F. Giesen, J. Podbielski and D. Grundler. *Mode localization transition in ferromagnetic microscopic rings.* Physical Review B (Condensed Matter and Materials Physics) **76**, 014431 (2007).

[Gil04] T.L. Gilbert. *A phenomenological theory of damping in ferromagnetic materials.* Magnetics, IEEE Transactions on **40**, 3443–3449 (2004).

[Gil05] W. Gil, D. Görlitz, M. Horisberger and J. Kötzler. *Magnetoresistance anisotropy of polycrystalline cobalt films: Geometrical-size and domain effects.* Phys. Rev. B **72**, 134401 (2005).

[Gru00] D. Grundler. *Large Rashba splitting in InAs quantum wells due to electron wave function penetration into the barrier layers.* Phys. Rev. Lett. **84**, 6074–6077 (2000).

[Gru01a] D. Grundler. *Ballistic spin-filter transistor.* Phys. Rev. B **63**, 161307 (2001).

[Gru01b] D. Grundler. *Oscillatory spin-filtering due to gate control of spin-dependent interface conductance.* Phys. Rev. Lett. **86**, 1058–1061 (2001).

[Gru07] G. Gruenberg. *Nobel prize lecture, http://nobelprize.org/nobel_ prizes/ physics/laureates/2007/grunberg-slides.pdf*, 2007.

[Gui07] Y. S. Gui, N. Mecking, X. Zhou, Gwyn Williams and C.-M. Hu. *Realization of a room-temperature spin dynamo: The spin rectification effect.* Physical Review Letters **98**, 107602 (2007).

[Hal80] E. H. Hall. *On the new action of magnetism on a permanent electric current.* Philos. Mag. **10**, 301 (1880).

[Hal06] K. C. Hall and M. E. Flatté. *Performance of a spin-based insulated gate field effect transistor.* Applied Physics Letters **88**, 162503 (2006).

[Han05] A. E. Hansen, M. T. Björk, C. Fasth, C. Thelander and L. Samuelson. *Spin relaxation in inas nanowires studied by tunable weak antilocalization.* Physical Review B (Condensed Matter and Materials Physics) **71**, 205328 (2005).

[Hau92] R. J. Haug, H. Munekata and L. L. Chang. *One-dimensional conduction on the cleaved edge of InAs quantum wells.* Japanese Journal of Applied Physics **31**, L127–L129 (1992).

[Heu03] Heusler. *Über magnetische Manganlegierungen.* Verhandlungen der Deutschen Physikalischen Gesellschaft **5**, 219 (1903).

[Hey02] C. Heyn, S. Mendach, S. Schnüll, S. Löhr, S. Beyer and W. Hansen. *Growth of shallow InAs HEMTs with metamorphic buffer.* Molecular Beam Epitaxy, 2002 International Conference on 185–186 (2002).

[Hey08] Ch. Heyn. *Private communication (Universität Hamburg)*, 2008.

[Hil02] B. Hillebrands and K. Ounadjela. *Spin Dynamics in confined magnetic structures I.* Forschungszentrum Jülich, 2002.

[Hoe06] M. Hoener, O. Kronenwerth, Ch. Heyn, D. Grundler and M. Holz. *Geometry-enhanced magnetoresistance of narrow Au/InAs hybrid structures incorporating a two-dimensional electron system.* Journal of Applied Physics **99**, 036102 (2006).

[Hol03a] M. Holz, O. Kronenwerth and D. Grundler. *Magnetoresistance of semiconductor-metal hybrid structures: The effects of material parameters and contact resistance*. Phys. Rev. B **67**, 195312 (2003).

[Hol03b] M. Holz, O. Kronenwerth and D. Grundler. *Optimization of semiconductor–metal hybrid structures for application in magnetic-field sensors and read heads*. Applied Physics Letters **83**, 3344–3346 (2003).

[Hol06] M. Holz. *Discussion and computer simulations about/of the expected GMR signatures for our sample design (private communication)*, 2006.

[Hu01a] C.-M. Hu and T. Matsuyama. *Spin injection across a heterojunction: A ballistic picture*. Phys. Rev. Lett. **87**, 066803 (2001).

[Hu01b] C.-M. Hu, Junsaku Nitta, A. Jensen, J. B. Hansen and Hideaki Takayanagi. *Spin-polarized transport in a two-dimensional electron gas with interdigital-ferromagnetic contacts*. Phys. Rev. B **63**, 125333 (2001).

[Hu03] C.-M. Hu, C. Zehnder, Ch. Heyn and D. Heitmann. *THz collective spin-flip excitation of a two-dimensional electron system*. Phys. Rev. B **67**, 201302 (2003).

[Hua07] B. Huang, D. J. Monsma and I. Appelbaum. *Experimental realization of a silicon spin field-effect transistor*. Applied Physics Letters **91**, 072501 (2007).

[Hub98] A. Hubert and R. Schäfer. *Magnetic Domains – The Analysis of Magnetic Microstructures*. Springer, Berlin, 1998.

[Iba99] H. Ibach and H. Lüth. *Festkörperphysik - Einführung in die Grundlagen*. Springer, Berlin, 5. Auflage, 1999.

[Int07] Intel. *http://techresearch.intel.com/articles/index.html*, 2007.

[Isl07] J. Islam, Y. Yamamoto, Eiji Shikoh, Akihiko Fujiwara and H. Hori. *A comparative study of Co and Fe thin films deposited on GaAs(001) substrate*. Journal of Magnetism and Magnetic Materials **320**, 571–574 (2007).

[Jao77] O. Jaoul, I. A. Campbell and A. Fert. *Spontaneous resistivity anisotropy in Ni alloys*. Journal of Magnetism and Magnetic Materials **5**, 23–34 (1977).

[Jed02] F. J. Jedema, H. B. Heersche, A. T. Filip, J. J. A. Baselmans and B. J. van Wees. *Electrical detection of spin precession in a metallic mesoscopic spin valve*. Nature **416**, 713 (2002).

[Ji01] Y. Ji, G. J. Strijkers, F. Y. Yang, C. L. Chien, J. M. Byers, A. Anguelouch, Gang Xiao and A. Gupta. *Determination of the spin polarization of half-metallic CrO_2 by point contact andreev reflection*. Phys. Rev. Lett. **86**, 5585–5588 (2001).

[Joh98] M. Johnson. *Theory of spin-dependent transport in ferromagnet-semiconductor heterostructures*. Phys. Rev. B **58**, 9635–9638 (1998).

[Kat00] J. A. Katine, F. J. Albert, R. A. Buhrman, E. B. Myers and D. C. Ralph. *Current-driven magnetization reversal and spin-wave excitations in Co /Cu /Co pillars.* Phys. Rev. Lett. **84**, 3149–3152 (2000).

[Kit93] Charles Kittel. *Einführung in die Festkörperphysik.* R. Oldenbourg Verlag GmbH, München, 10. Auflage, 1993.

[Kli80] K. v. Klitzing, G. Dorda and M. Pepper. *New method for high-accuracy determination of the fine-structure constant based on quantized hall resistance.* Phys. Rev. Lett. **45**, 494–497 (1980).

[Kli93] K. v. Klitzing. *Nobel Lectures in Physics 1981-1990.* World Scientific Publishing Company, Singapore, 1993.

[Kli05] K. v. Klitzing, R. Gerhardts and J. Weis. *25 Jahre Quanten–Hall–Effekt.* Physik Journal **6**, 37 (2005).

[Koo08] H. C. Koo, J. H. Kwona, J. Eoma, J. Changa and Han S.-H. *Interface resistance dependence of spin transport in a ferromagnetsemiconductor hybrid structure.* Journal of Magnetism and Magnetic Materials **320**, 1436–1439 (2008).

[Kor07] T. Korn. *Discussion about time-resolved faraday rotation experiments on GaAs/AlGaAs heterostructures (private communication)*, 2007.

[Köt05] J. Kötzler and W. Gil. *Anomalous Hall resistivity of cobalt films: Evidence for the intrinsic spin-orbit effect.* Physical Review B (Condensed Matter and Materials Physics) **72**, 060412 (2005).

[Kro03] O. Kronenwerth, C. H. Möller, D. Grundler, Ch. Heyn and D. Heitmann. *in: toward the controllable quantum states, edited by h. takayanagi and j. nitta.* Proceedings of MS+S 2002 99 (2003).

[Kro04a] H. Kroemer. *The 6.1 Å family (InAs, GaSb, AlSb) and its heterostructures: a selective review.* Physica E: Low-dimensional Systems and Nanostructures **20**, 196 (2004).

[Kro04b] O. Kronenwerth. *Extraordinary Magnetoresistance Effect: Metall-Halbleiter-Hybridstrukturen in homogenen und inhomogenen Magnetfeldern.* Doctoral thesis, Universität Hamburg, 2004.

[Kro07] H. Kronmüller, S. Parkin and R. Winkler. *Handbook of Magnetism and Advanced Magnetic Materials*, Vol. 5. John Wiley & Sons Ltd., 2007.

[Kru06] V. V. Kruglyak and R. J. Hicken. *Magnonics: Experiment to prove the concept.* Journal of Magnetism and Magnetic Materials **306**, 191–194 (2006).

[Ky66] V.-D. Ky. *Plane Hall effect in ferromagnetic metals.* Soviet Journal of Experimental and Theoretical Physics **23**, 809 (1966).

[Lan30] L. Landau. *Diamagnetismus der Metalle.* Zeitschrift für Physik A Hadrons and Nuclei **64**, 629–637 (1930).

[Lan35] L. D. Landau and E. M. Lifshitz. *On the theory of the dispersion of magnetic permeability in ferromagnetic bodies.* Phys. Z. Sowjet. **8**, 153–169 (1935).

[Lan65] L.D. Landau and D. ter Haar. *Collected papers of LD Landau.* Pergamon Press, 1965.

[Las85] R. Lassnig. *$\overrightarrow{k} \cdot \overrightarrow{p}$ theory, effective-mass approach, and spin splitting for two-dimensional electrons in GaAs-GaAlAs heterostructures.* Phys. Rev. B **31**, 8076–8086 (1985).

[Lau81] R. B. Laughlin. *Quantized Hall conductivity in two dimensions.* Phys. Rev. B **23**, 5632–5633 (1981).

[Lin03] J. Lindner and K. Baberschke. *In situ ferromagnetic resonance: an ultimate tool to investigate the coupling in ultrathin magnetic films.* Journal of Physics: Condensed Matter **15**, R193–R232 (2003).

[Löh03] S. Löhr, S. Mendach, T. Vonau, Ch. Heyn and W. Hansen. *Highly anisotropic electron transport in shallow InGaAs heterostructures.* Phys. Rev. B **67**, 045309 (2003).

[Lom88] G. Lommer, F. Malcher and U. Rössler. *Spin splitting in semiconductor heterostructures for $B \rightarrow 0$.* Phys. Rev. Lett. **60**, 728 (1988).

[Maj00] J.A. Majewski, P. Vogl and P. Lugli. *First principles study of spin-electronics: Zero-field spin-splitting in superlattices.* Proceedings of the 25th International Conference of the Physics of Semiconductors, Osaka (2000).

[Maj02] J.A. Majewski and P. Vogl. *Resonant spin-orbit interactions and phonon relaxation rates in superlattices.* Proceedings of the 26th International Conference of the Physics of Semiconductors, Edinburgh (2002).

[Mat02] T. Matsuyama, C.-M. Hu, D. Grundler, G. Meier and U. Merkt. *Ballistic spin transport and spin interference in ferromagnet/InAs(2DES)/ferromagnet devices.* Phys. Rev. B **65**, 155322 (2002).

[Mec07] N. Mecking, Y. S. Gui and C.-M. Hu. *Microwave photovoltage and photoresistance effects in ferromagnetic microstrips.* Physical Review B (Condensed Matter and Materials Physics) **76**, 224430 (2007).

[Mec08] N. Mecking. *A comprehensive study of the AMR-induced microwave photovoltage, photocurrent and photoresistance in Permalloy microstrips.* Doctoral thesis, Universität Hamburg, 2008.

[Mei07] L. Meier, G. Salis, I. Shorubalko, E. Gini, S. Schön and K. Ensslin. *Measurement of Rashba and Dresselhaus spin-orbit magnetic fields.* Nature Physics **3**, 650 (2007).

[Men01] S. Mendach, C.-M. Hu, Ch. Heyn, S. Schnüll, H.P. Oepen, R. Anton and W. Hansen. *Strain relaxation in high-mobility InAs inserted-channel heterostructures with metamorphic buffer.* Physica E **13**, 1204 (2001).

[Möl02] C. H. Möller, O. Kronenwerth, D. Grundler, W. Hansen, Ch. Heyn and D. Heitmann. *Extraordinary magnetoresistance effect in a microstructured metal–semiconductor hybrid structure.* Applied Physics Letters **80**, 3988–3990 (2002).

[Möl03a] C. H. Möller, D. Grundler, O. Kronenwerth, C. Heyn and D. Heitmann. *Effect of the Interface Resistance on the Extraordinary Magnetoresistance of Semiconductor/Metal Hybrid Structures.* Journal of Superconductivity **16**, 195–199 (2003).

[Möl03b] C. H. Möller, Ch. Heyn and D. Grundler. *Spin splitting in narrow InAs quantum wells with $In_{0.75}Ga_{0.25}As$ barrier layers.* Applied Physics Letters **83**, 2181–2183 (2003).

[Mot36] N. F. Mott. *The electrical conductivity of transition metals.* Proceedings of the Royal Society of London **153**, 699–717 (1936).

[New96] R. M. H. New, R. F. W. Pease and R. L. White. *Lithographically patterned single-domain cobalt islands for high-density magnetic recording.* Journal of Magnetism and Magnetic Materials **155**, 140–145 (1996).

[Nit97] Junsaku Nitta, Tatsushi Akazaki, Hideaki Takayanagi and Takatomo Enoki. *Gate control of spin-orbit interaction in an inverted $In_{0.53}Ga_{0.47}As/In_{0.52}Al_{0.48}As$ heterostructure.* Phys. Rev. Lett. **78**, 1335–1338 (1997).

[Par02] J. S. Parker, S. M. Watts, P. G. Ivanov and P. Xiong. *Spin polarization of CrO_2 at and across an artificial barrier.* Phys. Rev. Lett. **88**, 196601 (2002).

[Pod06] J. Podbielski, F. Giesen and D. Grundler. *Spin-wave interference in microscopic rings.* Physical Review Letters **96**, 167207 (2006).

[Pri95] G. A. Prinz. *Spin-polarized transport.* Physics Today **48**, 58–63 (1995).

[Ras03] E. I. Rashba and Al. L. Efros. *Orbital mechanisms of electron-spin manipulation by an electric field.* Phys. Rev. Lett. **91**, 126405 (2003).

[Ric00] A. Richter, M. Koch, T. Matsuyama, Ch. Heyn and U. Merkt. *Transport properties of modulation-doped InAs-inserted-channel $In_{0.75}Al_{0.25}As/In_{0.75}Ga_{0.25}As$ structures grown on GaAs substrates.* Appl. Phys. Lett. **77**, 3227 (2000).

[Rie84] H. Riechert, S. F. Alvarado, A. N. Titkov and V. I. Safarov. *Precession of the spin polarization of photoexcited conduction electrons in the band-bending region of GaAs (110).* Phys. Rev. Lett. **52**, 2297–2300 (1984).

[Sch84] L. Schweitzer, B. Kramer and A. MacKinnon. *Magnetic field and electron states in two-dimensional disordered systems.* Journal of Physics C: Solid State Physics **17**, 4111–4125 (1984).

[Sch00] G. Schmidt, D. Ferrand, L.W. Molenkamp, A.T. Filip and B.J. van Wees. *Fundamental obstacle for electrical spin injection from a ferromagnetic metal into a diffusive semiconductor.* Phys. Rev. B **62**, R4790 (2000).

[Sch03] J. Schliemann, J. C. Egues and D. Loss. *Nonballistic spin-field-effect transistor.* Physical Review Letters **90**, 146801 (2003).

[Sha65] Y.U. Sharvin. *A possible method for studying fermi surfaces.* Sov. Phys. JETP **21**, 655 (1965).

[Shu30] L. Shubnikov and W. J. de Haas. *Magnetische Widerstandsvergrösserung in Einkristallen von Wismut bei tiefen Temperaturen.* Comm. Phys. Lab. Univ. Leiden **207a** (1930).

[Smi51] J. Smit. *Magnetoresistance of ferromagnetic metals and alloys at low temperatures.* Physica **17**, 612–627 (1951).

[Sni07] G. Snider. *1d poisson, downloadable at: www.nd.edu/∼gsnider*, 2007.

[Sol00] S. A. Solin, T. Thio, D. R. Hines and J. J. Heremans. *Enhanced room-temperature geometric magnetoresistance in inhomogeneous narrow-gap semiconductors.* Science **289**, 1530 (2000).

[Son02] Pil Hun Song and K. W. Kim. *Spin relaxation of conduction electrons in bulk III-V semiconductors.* Phys. Rev. B **66**, 035207 (2002).

[Sou98] Jr. Soulen, R. J., J. M. Byers, M. S. Osofsky, B. Nadgorny, T. Ambrose, S. F. Cheng, P. R. Broussard, C. T. Tanaka, J. Nowak, J. S. Moodera, A. Barry and J.M.D. Coey. *Measuring the spin polarization of a metal with a superconducting point contact.* Science **282**, 85–88 (1998).

[Sti07] D. Stich, J. H. Jiang, T. Korn, R. Schulz, D. Schuh, W. Wegscheider, M. W. Wu and C. Schüller. *Detection of large magnetoanisotropy of electron spin dephasing in a high-mobility two-dimensional electron system in a* [001] $GaAs/Al_xGa_{(1-x)}As$ *quantum well.* Physical Review B (Condensed Matter and Materials Physics) **76**, 073309 (2007).

[Sto83] H. L. Stormer and D. C. Tsui. *The Quantized Hall Effect.* Science **220**, 1241–1246 (1983).

[Tac99] Atsushi Tackeuchi, Takamasa Kuroda, Shunichi Muto and Osamu Wada. *Picosecond electron-spin relaxation in GaAs/AlGaAs quantum wells and InGaAs/InP quantum wells.* Physica B: Condensed Matter **272**, 318–323 (1999).

[Tan59] P. E. Tannenwald and M. H. Seavey Jr. *Microwave resonance in thin ferromagnetic films.* Le Journal de Physique et le Radium **20**, 323–326 (1959).

[Tre06] A. Trellakis, T. Zibold, T. Andlauer, S. Birner, R. K. Smith, R. Morschl and P. Vogl. *The 3d nanometer device project nextnano: Concepts, methods, results.* Journal of Computational Electronics **5**, 285–289 (2006).

[Tse02] Y. Tserkovnyak, A. Brataas and G. E. W. Bauer. *Enhanced Gilbert damping in thin ferromagnetic films.* Phys. Rev. Lett. **88**, 117601 (2002).

[Tse05] Y. Tserkovnyak, A. Brataas, G. E. W. Bauer and B. I. Halperin. *Nonlocal magnetization dynamics in ferromagnetic heterostructures.* Reviews of Modern Physics **77**, 1375 (2005).

[vdP58] L. J. van der Pauw. *A method of measuring specific resistivity and Hall effect of discs of arbitrary shape.* Philips Res. Repts. **13**, 1 (1958).

[Vog07] P. Vogl. *Discussion about spin–orbit interaction calculated with a tight-binding approach (private communication)*, 2007.

[vS87] P. C. van Son, H. van Kempen and P. Wyder. *Boundary resistance of the ferromagnetic-nonferromagnetic metal interface.* Phys. Rev. Lett. **58**, 2271–2273 (1987).

[Vur01] I. Vurgaftman, J. R. Meyer and L. R. Ram-Mohan. *Band parameters for III-V compound semiconductors and their alloys.* Journal of Applied Physics **89**, 5815–5875 (2001).

[vW07] B. van Wees. *Semiconductor spintronics: Spins go their own way.* Nature Physics **3**, 147–148 (2007).

[Wag08] U. Wagner. *Ferromagnetische Resonanz an dünnen Heusler-Filmen und einem nanostrukturierten Permalloy-Ring.* Diploma thesis, Technische Universität München, 2008.

[Wan06] X. Wang, G. E. W. Bauer, B. J. van Wees, A. Brataas and Y. Tserkovnyak. *Voltage generation by ferromagnetic resonance at a nonmagnet to ferromagnet contact.* Physical Review Letters **97**, 216602 (2006).

[Wei86] G. Weimann. *Transport properties of semiconductor heterostructures*, Vol. 26 aus *Festkörperprobleme.* Vieweg, Braunschweig, 1986.

[Wil02] Z. Wilamowski, W. Jantsch, H. Malissa and U. Rössler. *Evidence and evaluation of the Bychkov-Rashba effect in SiGe/Si/SiGe quantum wells.* Phys. Rev. B **66**, 195315 (2002).

[Win03] R. Winkler. *Spin–Orbit Coupling Effects in Two-Dimensional Electron and Hole Systems.* Springer Berlin / Heidelberg, Springer-Verlag GmbH, Heidelberg, Germany, 2003.

[Win04] R. Winkler. *Spin orientation and spin precession in inversion-asymmetric quasi-two-dimensional electron systems.* Physical Review B (Condensed Matter and Materials Physics) **69**, 045317 (2004).

[Wu00] Ning C. Z. Wu, M. W. *A novel mechanism for spin dephasing due to spin-conserving scatterings.* The European Physical Journal B - Condensed Matter and Complex Systems **18**, 373–376 (2000).

[Wun02] O. Wunnicke, Ph. Mavropoulos, R. Zeller, P. Dederichs and D. Grundler. *Ballistic spin injection from Fe(001) into ZnSe and GaAs.* Phys. Rev. B **65**, 241306(R) (2002).

[Xia01] K. Xia, P. J. Kelly, G. E. W. Bauer, I. Turek, J. Kudrnovský and V. Drchal. *Interface resistance of disordered magnetic multilayers.* Phys. Rev. B **63**, 064407 (2001).

[Yaf63] Y. Yafet. *g factors and spin-lattice relaxation of conduction electrons.* Solid State Physics **14**, 1 (1963).

[Yau71] K L Yau and J T H Chang. *The planar Hall effect in thin foils of Ni-Fe alloy.* Journal of Physics F: Metal Physics **1**, 38–43 (1971).

[Zaw04] W. Zawadzki and P. Pfeffer. *Spin splitting of subband energies due to inversion asymmetry in semiconductor heterostructures.* Semiconductor Science and Technology **19**, R1–R17 (2004).

[Zho01] T. Zhou, D. R. Hines and S. A. Solin. *Extraordinary magnetoresistance in externally shunted van der Pauw plates.* Applied Physics Letters **78**, 667–669 (2001).

[Zut04] I. Zutić, J. Fabian and S. D. Sarma. *Spintronics: Fundamentals and applications.* Reviews of Modern Physics **76**, 323 (2004).

[Zwi03] M. Zwierzycki, K. Xia, P. J. Kelly, G. E. W. Bauer and I. Turek. *Spin injection through an Fe/InAs interface.* Phys. Rev. B **67**, 092401 (2003).

Acknowledgements

During the formation of this thesis I was accompanied by many dear people. I am very grateful for all discussions and contributions, and for the assistance and support I received from those people in Hamburg and in Munich. I wish to express my gratitude to all of the following:

My Ph.D. advisor and referees of this thesis and disputation
Prof. Dr. Detlef Heitmann
Prof. Dr. Dirk Grundler
Prof. Dr. Wolfgang Hansen

my collaborators

Prof. Dr. Peter Vogl	Stefan Birner	Bernhard Botters
Tillmann Kubis	Dr. Nikolai Mecking	Sebastian Neusser
Kevin Rachor	Daniel Stickler	

the scientific and technical staff at the TU München, in particular

Dr. Paul Berberich	Herbert Hetzl	Roswitha Hoppen
Stephan Lichtenauer	Thomas Rapp	Johannes Seitz
Heinz Singer	Valentin Vedl	Birgit Wiedemann
Tjark Windisch	Dr. Mark Wilde	

the scientific and technical staff at the Universität Hamburg, in particular

Prof. Dr. Daniela Pfannkuche	PD Dr. habil. Guido Meier	Rolf Beneke
Horst Biedermann	Dr. René Eiselt	Thomas Finger
Wolfgang Hatje	Dr. Christian Heyn	Renate Kiesewalter
Dr. Tobias Kipp	Dr. Tobias Korn	Dr. Jan Podbielski
Andrea Stemmann	Jürgen Swirski	

my family
my father Reinhold Wittmann
my brother Jürgen Wittmann

my girlfriend
Christina Kempf

my close friends

Dr. Claus Christ	Alexander Eck	Florian Festner
Axel Hannemann	Benjamin Janutta	Simon Kayser
Dr. Matthias Kraft	Christian Menk	Dr. Claas H. Möller
Jan Reblin	Matthias Schröder	Dirk M. Wilhelm